

FACULDADE DE ENGENHARIA DA UNIVERSIDADE DO PORTO

**Study and development of new geometries of optical
fiber sensors for monitorization of crystallizers in
pharmaceutical field**

Liliana Patrícia Santos Soares



Programa Doutoral em Engenharia Física

Supervisor: Susana Ferreira de Oliveira Silva

Co-supervisors: António Manuel Azevedo Ferreira and Orlando José Reis Frazão

February 4, 2025

Study and development of new geometries of optical fiber sensors for monitorization of crystallizers in pharmaceutical field

Liliana Patrícia Santos Soares

Programa Doutoral em Engenharia Física

Approved in oral examination by the committee:

Chair: Prof. Joana Cassilda Rodrigues Espain de Oliveira

External Examiner: Prof. Paulo Sérgio de Brito André

External Examiner: Dr. Marta Sofia dos Anjos Ferreira

Local Examiner: Prof. Joaquim Agostinho Gomes Moreira

Local Examiner: Prof. Manuel Joaquim Bastos Marques

Local Examiner: Prof. Carlos Daniel Diogo Matias Pintassilgo

Supervisor: Dr. Susana Ferreira de Oliveira Silva

Co-Supervisors: Dr. António Manuel Ferreira and Prof. Orlando José dos Reis Frazão

February 4, 2025



Liliana Soares agradece a bolsa de doutoramento da Fundação para a Ciência e a Tecnologia (FCT), com a referência 2020.05297.BD, DOI:10.54499/2020.05297.BD, financiada por fundos nacionais do Ministério da Ciência, Tecnologia e Ensino Superior (MCTES), com verbas do Orçamento de Estado, por verbas do Fundo Social Europeu (FSE), ao abrigo do PORTUGAL2020, e através do Programa PDQI - Demografia, Qualificações e Inclusão, o Pessoas 2030, e através do Programa Operacional Regional do Norte (NORTE 2020).

Este trabalho foi suportado por fundos nacionais, FCT/MCTES (PIDDAC): LEPABE, UIDB/00511/2020 (DOI: 10.54499/UIDB/00511/2020); UIDP/00511/2020 (DOI: 10.54499/UIDP/00511/2020) e ALiCE, LA/P/0045/2020 (DOI: 10.54499/LA/P/0045/2020).

Abstract

Crystallization is an important operation for the processing and development in pharmaceutical field. Through it, it is possible to produce 90% of pharmaceutical products, the Active Pharmaceutical Ingredients (APIs).

Despite its relevant role in the pharmaceutical industry, the control and monitoring of crystallization are still limited, because the technology available for this purpose, Process Analytical Technology (PAT), is incompatible with the geometry of some today's crystallizer systems (crystallizers/ reactors).

Batch production is the approach more used in crystallization processes. However, with technological and scientific development, more efficient methods of production were discovered, such as production in a continuous way.

The final product quality optimization, though continuous crystallization, created the development of new geometries of crystallizers, namely, the Oscillatory Flow Crystallizer (OFC). The results reached with this new geometry of crystallizers are very promising, however there is a need related to PAT tools available for monitoring the process flow of crystallizers *in situ*. The technology available for this has higher dimensions than the OFC vessels (diameters in the order of millimeters).

In this dissertation the use of fiber optic technology to answer this need is proposed.

Since its discovery, and especially from the 1970s, fiber optics technology has been revealed to be a versatile means to produce detection tools, such as optical fiber sensors, with applicability in several areas.

Considering the dimensions of optical fibers, it is believed that a solution based on this technology is capable of monitoring different processual parameters during crystallization process, regardless of the crystallizer geometry.

In this work, some geometries of sensors are presented. Specifically, optical fiber probes capable of monitoring process parameters in liquid solutions, namely, concentration and temperature.

The characteristics of the developed optical fiber sensors allow them to be introduced into the process flow of different crystallizer geometries, in a non-invasive and non-destructive way. Validation of the entire technology in a real context, in crystallizers, confirms the ability of the

sensors to read the parameters of interest, concentration and temperature, in situ throughout the crystallization process. In this way, control and monitoring of the crystallization process are ensured in any crystallizer geometry, allowing the optimization of the entire crystallization system, whether batch or continuous. Maximum use of reagents is ensured and the quality of the final product, the APIs, is guaranteed, using low-cost technology (based on optical fibers), compared to current PAT technologies (probes).

Keywords: crystallization, active pharmaceutical ingredients, process analytical technology, continuous crystallization, oscillatory flow crystallizer, optical fiber sensors, process parameters.

Resumo

A cristalização é uma operação muito importante para o processamento e desenvolvimento na indústria farmacêutica. Através da mesma são produzidos cerca de 90% dos seus produtos, os Princípios Ativos Cristalinos (APIs).

Apesar do seu papel de relevo na indústria farmacêutica, o controlo e a monitorização da cristalização são ainda operações bastante limitadas, uma vez que a tecnologia disponível para este efeito, tecnologia analítica de processo (PAT), é incompatível com as geometrias de alguns dos sistemas de cristalização (cristalizadores/reatores) atuais.

A produção em “batch” é a abordagem mais usada em processos de cristalização. No entanto, com o avanço tecnológico foram surgindo métodos de produção mais eficientes, como é o caso da produção em contínuo.

A otimização da qualidade do produto final, através da cristalização em contínuo, originou o desenvolvimento de novas geometrias de cristalizadores, como o cristalizador de fluxo oscilatório (OFC). Apesar dos resultados promissores alcançados com esta nova geometria de cristalizador, surge a necessidade de desenvolver uma tecnologia capaz de monitorizar o seu fluxo de processo *in situ*, uma vez que as ferramentas PAT disponíveis para este efeito possuem dimensões superiores ao diâmetro dos vasos do OFC (diâmetros na ordem dos milímetros).

Nesta dissertação é proposta a utilização da tecnologia em fibra ótica para dar resposta a esta necessidade.

Desde o seu surgimento, e sobretudo a partir da década de 1970, a fibra ótica tem-se revelado um meio bastante versátil para a produção de tecnologias de deteção, como é o caso dos sensores em fibra ótica, com aplicação nas mais variadas áreas.

Tendo em conta as dimensões da fibra ótica, acredita-se que uma solução baseada nesta tecnologia é capaz de monitorizar diferentes parâmetros processuais ao longo da cristalização, independentemente da geometria de cristalizador.

Neste trabalho são apresentadas algumas geometrias sensoras, especificamente pontas de prova em fibra ótica, capazes de monitorizar parâmetros processuais em líquidos, como é o caso da concentração e da temperatura.

As características dos sensores em fibra ótica desenvolvidos permitem que estes sejam introduzidos no fluxo de processo das diferentes geometrias de cristalizadores, de forma não invasiva e não destrutiva. A validação de toda a tecnologia em contexto real, nos cristalizadores, constata a capacidade de os sensores realizarem a leitura dos parâmetros de interesse, concentração e temperatura, *in situ* ao longo do processo de cristalização. Desta forma, o controlo e a monitorização do processo de cristalização são assegurados em qualquer geometria de cristalizador, permitindo ainda otimizar todo o sistema de cristalização, quer seja este em batch ou em contínuo. O aproveitamento máximo dos reagentes é assegurado e a qualidade do produto final, os APIs, são garantidos, utilizando uma tecnologia (baseada em fibras óticas) de baixo custo, comparativamente às tecnologias PAT atuais (sondas).

Palavras-chave: cristalização, princípios ativos, tecnologia analítica de processo, cristalização em contínuo, cristizador de fluxo oscilatório, sensores em fibra ótica, parâmetros processuais.

Acknowledgements

I would like to express my gratitude to all the people who were directly or indirectly involved in completing another stage of my academic life.

To my supervisors, Dr. Susana Silva, Professor Orlando Frazão and Dr. António Ferreira, I express my deep gratitude for their guidance, total support, professionalism and availability. For the knowledge they transmitted, for their criticisms and opinions and, above all, for their collaboration in resolving doubts and problems that arose throughout the development of this work. I also appreciate the words of encouragement and the opportunity to learn a little more.

To the Center for Applied Photonics (INESC TEC, CAP) and the Laboratory of Process Engineering, Environment, Biotechnology and Energy (LEPABE) – Department of Chemical Engineering at FEUP, for providing me with all the necessary conditions to prepare this project. I am grateful for the friendliness and availability of everyone involved.

To My Friends for sharing good (and less good) moments, for their sincere friendship and for transmitting confidence and strength.

To Jean-Philippe, the love of my life and my best friend, for his patience, support, affection and complicity, and for encouraging me in the most difficult moments. Thank you for your serenity and positivism.

To My Family, especially My Parents and My Grandparents. Thank you for all the teaching and for always believing in me.

Last, but not least, to my four-legged companions, Lucas, Kiko and Channel. Thank you for your loyalty and for your silent looks of tenderness.

Thank you all.

*“Life is not easy for any of us. But what of that?
We must have perseverance and above all confidence in ourselves. We must believe that we are
gifted for something, and that this thing must be attained.”*

Marie Curie

Contents

Chapter 1. Introduction

1.1.	Motivation and objectives	1
1.2.	Dissertation overview	2
1.3.	Main contributions.....	3
1.4.	List of publications	4

Chapter 2. Crystallization

2.1.	Theoretical notions	6
2.2.	Crystallization types	7
2.2.1.	Batch crystallization	8
2.2.2.	Continuous crystallization	9
2.3.	Geometries of continuous crystallizers: the Oscillatory Flow Crystallizer	9
2.4.	Monitorization of crystallization process: PAT tools	13
2.4.1.	Limitations of PAT tools	14
2.4.2.	Fiber-optic based solutions as alternative to conventional PAT tools	16
	References.....	18

Chapter 3. Optical fiber sensors

3.1.	Optical fiber concept	23
3.1.1.	Structural and material characterization	23
3.1.2.	Physical operating mechanism.....	24
3.2.	Optical fiber classification.....	28
3.3.	Optical fiber as a sensing tool.....	29
3.4.	Classification of optical fiber sensors.....	29
3.5.	Intensity modulated sensors.....	30
	References.....	31

Chapter 4. Optical fiber tips for refractive index sensing

4.1.	Introduction	33
4.2.	Graded-index fiber tip sensor for refractometric analysis of ethanol-water binary solutions ...	35
4.2.1.	Sensing head and experimental setup	36
4.2.2.	Output spectrum.....	39
4.2.3.	Measurements of ethanol-water binary solutions	39
4.2.4.	Influence of temperature	42
4.2.5.	Concluding remarks	43

4.3.	Graded-index fiber tip sensor for crystallization process detection	44
4.3.1.	Sensor characterization and operating mechanism	45
4.3.2.	Monitorization of crystallization process.....	50
4.3.3.	Concluding remarks	53
4.4.	Final chapter remarks	53
	References.....	54
Chapter 5. Erbium-doped fiber lasers for refractive index sensing		
5.1.	Introduction	59
5.1.1.	Laser	59
5.1.2.	Optical fiber lasers	62
5.1.3.	Erbium-doped fiber lasers applications	64
5.2.	Erbium-doped fiber ring cavity configuration.....	65
5.2.1.	Sensing head structure and operating mechanism	66
5.2.2.	Output spectrum.....	67
5.2.3.	Fiber ring cavity characterization	68
5.2.4.	Sensing applications	69
5.2.5.	Concluding remarks	73
5.3.	Erbium-doped fiber laser based on linear cavity configuration.....	74
5.3.1.	Laser gain.....	74
5.3.2.	Experimental configurations	74
5.3.3.	Linear fiber lasers characterization.....	76
5.3.4.	Sensing applications	81
5.3.5.	Concluding remarks	85
5.4.	Final chapter remarks	86
	References.....	86
Chapter 6. Monitorization of crystallization in an oscillatory flow crystallizer using optical fiber sensors		
6.1.	Introduction	90
6.2.	Monitorization of concentration <i>in situ</i>	92
6.2.1.	Sensing head and portable interrogation system.....	92
6.2.2.	Measurements of paracetamol liquid solutions.....	93
6.2.3.	Monitorization of concentration in crystallizers	98
6.2.4.	Concluding remarks	103
6.3.	Monitorization of temperature <i>in situ</i>	103
6.3.1.	Experimental setup	105

6.3.2.	Monitorization of temperature in an OFC	108
6.3.3.	Monitorization of temperature in an OFC during a crystallization experiment.....	113
6.3.4.	Concluding remarks	115
6.4.	Simultaneous measurements of concentration and temperature in an OFC during a crystallization experiment.....	115
6.4.1.	Calibration curve and sensitivity	116
6.4.2.	Monitorization of concentration in an OFC during a crystallization experiment	121
6.4.3.	Concluding remarks	124
6.5.	Final chapter remarks	125
	References.....	126
Chapter 7.	Conclusions and future work.....	130
Appendix A.		
A.1.	Introduction	133
A.2.	Fundamentals of Raman spectroscopy	133
A.3.	Quantitative analysis of paracetamol.....	138
A.4.	Final remarks	146
	References.....	147
Appendix B.		
B.1.	Introduction	150
B.2.	Experimental setup	150
B.3.	Results and discussion.....	151
B.4.	Final remarks	156
	References.....	156

List of Figures

Figure 2.1. Schematic representation of the crystallization process.	6
Figure 2.2. Representation of a Stirred Tank Crystallizer	8
Figure 2.3. Schematic comparison between MSMPR and PF crystallizers.....	10
Figure 2.4. Representation of the oscillatory flow crystallizer operating principle	11
Figure 2.5. Difference between tubular and planar-OFCs.	12
Figure 2.6. Representation of a planar-OFC with SPC and identification of the crystallization phases that occur in each crystallizer section.	13
Figure 2.7. Experimental setup for monitoring the crystallization process using NIR probe	14
Figure 2.8. Experimental setup for monitoring the crystallization process using ATR-FTIR probe.....	15
Figure 2.9. Schematic representation of the dielectric constant sensor setup for monitoring the crystallization process.	15
Figure 2.10. Experimental setup for concentration measurements in crystallizers using densitometers	15
Figure 3.1. Schematic representation of an optical fiber.	24
Figure 3.2. Light refraction representation	25
Figure 3.3. Total reflection: (a) critical angle; (b) total reflection representation	26
Figure 3.4. Schematic representation of the acceptance cone.....	27
Figure 3.5. Refractive index profiles of optical fibers	28
Figure 3.6. Generic representation of an optical fiber sensor modulated in intensity.....	31
Figure 4.1. Schematic representation of different geometries of optical fiber tips sensors.	33
Figure 4.2. Schematic representation of the GI-MMF tip cleavage setup.	37
Figure 4.3. Scheme of the experimental setup used and detail of the sensing head.	38
Figure 4.4. Characterization of a GI-MMF-based fiber tip.....	39
Figure 4.5. Characterization of ethanol-water binary liquid solutions at room temperature	40
Figure 4.6. Refractive index dependence with ethanol concentration and temperature variations	41
Figure 4.7. Influence of temperature, as an external factor, in the sensor output power response.	43
Figure 4.8. Schematic representation of paracetamol polymorphs	44
Figure 4.9. Sensor characterization.....	46
Figure 4.10. Schematic representation of the experimental setup implemented.....	46
Figure 4.11. Characterization of paracetamol samples.	47
Figure 4.12. Optical power dependence on paracetamol concentration and respective refractive index. ...	48
Figure 4.13. Determination of sensor resolution.....	49
Figure 4.14. Experimental setup for the monitorization of paracetamol crystallization process.	50

Figure 4.15. Monitorization of paracetamol crystallization process.	51
Figure 4.16. Sensor output power response during the paracetamol crystallization process	52
Figure 5.1. Schematic representation of absorption and emission, created by radiation-medium interaction, between two levels of energy.....	59
Figure 5.2. Schematic of population inversion and amplified spontaneous emission	60
Figure 5.3. Lasing threshold	61
Figure 5.4. Schematic representation (simplified) of fiber laser elements.....	62
Figure 5.5. Schematic representation of a fiber laser and its principal elements	63
Figure 5.6. Schematic representation of fiber laser cavities	63
Figure 5.7. Experimental setup of the erbium-doped fiber ring cavity used for refractive-index measurements.....	66
Figure 5.8. Schematic of the sensing head and its operating mechanism.	67
Figure 5.9. EDFRC output spectrum pumped by a 976-nm laser at 20 mW, when both output port 2 (reference port) and output port 3 (sensing head) were in air.	67
Figure 5.10. Sensor characterization with (black line) and without (blue line) FBG	68
Figure 5.11. Concentration of paracetamol in solution as a function of refractive index.	69
Figure 5.12. Refractive index characterization of ethanol and deionized water mixtures.	70
Figure 5.13. EDFRC output spectra pumped by a 976-nm laser at 20 mW, when the reference port was in the reference solution and sensing head was in air.	71
Figure 5.14. Output power levels as a function of paracetamol concentration in solution when the end of the reference port was immersed in the reference solution.....	71
Figure 5.15. Evaluation of system resolution.	72
Figure 5.16. Schematic of the bidirectional erbium-doped fiber amplifier.....	74
Figure 5.17. Experimental setup of the fiber laser systems based on linear cavities.	75
Figure 5.18. Relation between optical output power and laser diode drive current for Setup (A)	77
Figure 5.19. Characterization of fiber laser systems of Setup (B).	78
Figure 5.20. Influence of temperature in the fiber laser system output power response of Setup (A).....	79
Figure 5.21. Long-term stability evaluation of fiber laser systems.....	80
Figure 5.22. Characterization of paracetamol liquid samples.....	81
Figure 5.23. Optical output power as a function of paracetamol concentration for each fiber laser system.	83
Figure 5.24. Resolution of the developed fiber laser systems.....	84
Figure 6.1. Schematic representation of planar-OFC.....	91
Figure 6.2. Schematic representation of the experimental setup and sensing head	93

Figure 6.3. Sensor calibration	95
Figure 6.4. Influence of temperature in the sensor performance.	96
Figure 6.5. Resolution of the developed system.	98
Figure 6.6. Experimental setup of the Stirred Tank crystallizer.	99
Figure 6.7. Paracetamol concentration during crystallization in the STC. Inset: Evolution of the optical power of the fiber tip sensor during crystallization.	100
Figure 6.8. Experimental setup of the Oscillatory Flow crystallizer.	101
Figure 6.9. Paracetamol concentration during crystallization in the OFC	102
Figure 6.10. Schematic representation of the operation principle of an FBG.....	104
Figure 6.11. Representation of the experimental setup used to monitor the temperature in an OFC.	105
Figure 6.12. Spectral characterization of the optical fiber tip sensors fabricated, before and after the FBG cleavage	106
Figure 6.13. Sensor's calibration. Variation of Bragg wavelength as a function of temperature, for each optical fiber tip sensor.....	107
Figure 6.14. Experimental setup for in-situ temperature monitorization in the OFC	108
Figure 6.15. Temperature variation inside the OFC when the crystallizer was fed with a flow rate of 28 mL/min and without oscillation	110
Figure 6.16. Temperature variation inside the OFC when the crystallizer was fed with a flow rate of 58 mL/min and without oscillation	111
Figure 6.17. Temperature variation inside the OFC when the crystallizer was fed with a flow rate of 58 mL/min and with oscillation	112
Figure 6.18. Experimental setup for in-situ temperature monitorization in the OFC during paracetamol crystallization process.....	113
Figure 6.19. Temperature variation inside the OFC during paracetamol crystallization	114
Figure 6.20. Characterization of paracetamol samples. Paracetamol concentration dependence on the refractive index.	116
Figure 6.21. Sensor calibration	118
Figure 6.22. Sensor calibration. Optical power sensor responses to the variation of temperature, at a measuring wavelength of 1520 nm.	119
Figure 6.23. Resolution of the FBG-based optical fiber tip sensor.....	121
Figure 6.24. Variation of concentration at the input OFC channel during the first cycle of paracetamol crystallization process.....	122
Figure 6.25. Temperature variation at the output OFC channel during the second cycle of paracetamol crystallization process.....	123

Figure 6.26. Variation of concentration at the output OFC channel during the second cycle of paracetamol crystallization process	124
Figure 6.27. Schematic representation of the monitorization of paracetamol crystallization in the OFC	124
Figure A.1. Diagram representation of Rayleigh and Raman scattering processes	134
Figure A.2. Characteristics regions of a Raman spectrum.....	135
Figure A.3. Schematic representation of a typical Raman spectrometer	136
Figure A.4. Example of a Raman spectrum and respective information	137
Figure A.5. Chemical structure of paracetamol	139
Figure A.6. Experimental setup: Raman spectrometer. System inVia Qontor, Renishaw®.	140
Figure A.7. Raman spectrum of silicon: calibration with a standard sample.....	140
Figure A.8. Raman spectra of ethanol and paracetamol samples in a spectral range of 300 to 1800 cm^{-1}	142
Figure A.9. Example of the adjustment performed in the calculations of paracetamol bands intensity ...	144
Figure A.10. Relative intensity (i.e., ratio between the intensity of paracetamol bands and the intensity of ethanol band at 881 cm^{-1}) as a function of paracetamol concentration	145
Figure B.1. Spectral characterization of the optical fiber tip sensor fabricated.	151
Figure B.2. Output spectrum for each RI measured (optical fiber tip sensor 1).	152
Figure B.3. Optical output power as a function of RI.....	152
Figure B.4. Measurements of paracetamol samples using optical fiber tip sensor (3).....	153
Figure B.5. Simulation results.	154
Figure B.6. Comparation between experimental and simulated data (normalized data). Variation of sensor output response as a function of RI.....	155

List of Tables

Table 2.1. Main differences between batch and continuous manufacturing.....	9
Table 2.2. Characterizations of the main models of continuous crystallizers: Mixed Suspension Mixed Product Removal and Plug Flow Crystallizer.....	10
Table 2.3. Resume of principal PAT tools used to monitor the crystallization process	14
Table 4.1. Different configurations of optical fiber tip sensors reported in literature.	34
Table 4.2. Parameters obtained by a third-order polynomial approximation when varying the %(v/v) of ethanol present in the ethanol-water binary liquid solutions properties	40
Table 4.3. Determination of samples' refractive index	42
Table 5.1. Determination of system resolution.	72
Table 5.2. Sensitivity of fiber laser systems to variations of paracetamol concentrations.....	83
Table 5.3. Determination of fiber laser systems resolution.	85
Table 6.1. Characterization of paracetamol liquid samples.	94
Table 6.2. Determination of system LOD.....	97
Table 6.3. Determination of system resolution.	98
Table 6.4. Variation of paracetamol concentration during crystallization process in the STC.....	100
Table 6.5. Variation of Bragg wavelength as a function of temperature	107
Table 6.6. Determination of sensors LOD.....	108
Table 6.7. Experimental setup for in-situ temperature monitorization in the OFC during paracetamol crystallization process.....	114
Table 6.8. Determination of FBG-based optical fiber tip sensor LOD.....	120
Table 6.9. Determination of sensor resolution.....	121
Table A.1. Raman spectroscopy applications in different scientific fields.....	138
Table A.2. Raman acquisition parameters adopted.....	141
Table A.3. Ethanol-assigned Raman bands and respective vibrational modes.....	142
Table A.4. Paracetamol-assigned Raman bands and respective vibrational modes.....	143
Table A.5. Intensity band sensitivity to the variation of paracetamol concentration.....	145
Table B.1. Parameters obtained by a linear approximation when varying the RI.....	154

Abbreviations

APIs	Active Pharmaceutical Ingredients
ASE	Amplified Spontaneous Emission
ATR	Attenuated Total Reflectance
ATR-FTIR	Attenuated Total Reflectance-Fourier Transform
BBS	Broadband Source
CAS	Chemical Abstracts Service
CCD	Charge-Coupled Device
ECTFE	Ethylene-Chlorotrifluoroethylene
EDF	Erbium-Doped Fiber
EDFA	Erbium-Doped Fiber Amplifier
EDFL	Erbium-Doped Fiber Laser
EDFRC	Erbium-Doped Fiber Ring Cavity
FBG	Fiber Bragg Grating
FBRM	Focused Beam Reflectance Measurements
GI	Graded-Index
HPLC	High-Performance Liquid Chromatography
LOT	Limit Of Detection
MMF	Multimode Fiber
MSMPR	Mixed Suspension Mixed Product Removal
NIR	Near Infrared Reflectance
OFC	Oscillatory Flow Crystallizer
OFS	Optical Fiber Sensor
OSA	Optical Spectrum Analyzer
OSNR	Optical Signal to Noise Ratio
PAT	Process Analytical Technology
PFC	Plug Flow Crystallizer
RI	Refractive Index
SHB	Spatial Hole Burning

SI	Step-Index
SMF	Single-Mode Fiber
SPC	Smooth Periodic Constrictions
STC	Stirred Tank Crystallizer
UV	Ultraviolet
WDM	Wavelength Division Multiplexer
YAG	Yttrium Aluminum Garnet

Chapter 1. Introduction

Crystallization is an important process in the pharmaceutical area, however, it is also a poorly understood and controlled process, as the technologies available for this purpose, the Process Analytical Technologies (PATs), are limited.

PAT corresponds to a set of tools used to guarantee the quality of the final product. Its implementation requires sensors that measure certain variables of interest/process parameters; however, some crystallizers have small vessels with channels with a diameter smaller than the diameter of the technology used, not allowing their immersion in the process flow and making it impossible to monitor the process parameters in real-time.

Optical fiber-based sensors are expected to revolutionize real-time monitoring of the crystallization process, offering a versatile solution applicable across all types of crystallizers. Since its emergence, and essentially since the 1970s, fiber optics technology has revolutionized the development of sensors. It has played a critical role in the emergence of optical sensors for several areas, such as biomedicine, military field, engineering, and fundamental sciences.

Accordingly, the development of fiber optic-based technology may provide a viable solution to address the specific crystallization monitoring and control requirements identified within the pharmaceutical industry.

In this chapter, the motivation and objectives of all the research work performed are presented, followed by a description of the structure of the dissertation. A list of publications resulting from the work developed and the main contributions to the field are also included.

1.1. Motivation and objectives

The work developed in the context of the PhD program was motivated by the development of a new geometry of crystallizer/reactor, the Oscillatory Flow Reactor (OFC), and the non-existence of PAT compatible with this reactor channels' dimensions.

Specifically, the main objective was the development of a fiber optic-based technology, capable of being implemented in different crystallizers, to respond to the need to monitor *in situ* and in real-time the crystallization process of Active Pharmaceutical Ingredients (APIs).

To achieve the main goal, over the PhD program, the main objectives of research activities were:

- Study of different configurations of optical fiber sensors, sensitive to parameters of interest (temperature, refractive index (RI), and concentration, that prove to be important for the pharmaceutical area).
- Fabrication and characterization of the developed optical fiber sensors.
- Development and optimization of a portable interrogation system that allowed the reading of process/interest parameters throughout the crystallization process.
- Validation of the system developed inside crystallizers, especially inside OFC channels.

1.2. Dissertation overview

This dissertation is composed of seven main chapters that describe the entire evolution of the developed research activities, from theoretical foundations to the production methods and characterization of the sensors, ending with their implementation.

Chapter 1 provides the structure, motivation and objectives of the project developed within the scope of the PhD program. The main publications that resulted from this thesis are also presented.

Chapter 2 corresponds to a brief introduction to the crystallization process of APIs, with theoretical notions about the stages of the crystallization process. The gaps identified by the pharmaceutical area in the control and monitor of this process are presented, as well as the PAT tools used in the different geometries of crystallizers/reactors for crystallization control.

Chapter 3 presents all the theoretical concepts and state-of-the-art inherent to the use of optical fiber sensors for sensing applications.

Chapter 4 presents the experimental characterization of the simplest configurations of optical fiber sensor tips, based on Multimode Graded Index Fibers (MMF-GIFs). In the end the performance of fabricated probes is tested for RI and concentration sensing, with applicability in the crystallization field: detection of the crystallization process of an API, the paracetamol.

Chapter 5 focuses on the implementation of the optical fiber tip sensors fabricated through an interrogation system, based on fiber laser technology. Different configurations of fiber laser systems (ring and linear configurations) were developed and the performance of them were compared for RI/concentration sensing.

Chapter 6 corresponds to the implementation of the developed technology *in situ*, i.e., the implementation of the optical fiber sensors based on MMF-GIF tips was performed in the reactors, especially in the OFC. The monitorization of RI and concentration during the paracetamol crystallization process was tested. Also, a new geometry of optical fiber sensor was also presented in this chapter. The sensor corresponds to a tip based on a cleaved FBG and allowed to perform temperature measurements, inside the OFC, during the crystallization process.

Finally, **Chapter 7** summarizes the main results achieved throughout the thesis and highlights its importance as an alternative for monitoring the crystallization process in the pharmaceutical industry. Guidelines for future work are also discussed in this context.

1.3. Main contributions

The research activities developed in the context of this PhD thesis revealed to have some scientific contributions, namely:

- The crystallization process of APIs, a process used to fabricate 90% of pharmaceutical products, was studied through the monitorization of some process parameters: RI, concentration and temperature.
- The development of an optical fiber-based technology, compatible with different geometries of crystallizers/reactors, allows the control of crystallization process, regardless of the equipment used and without disturbing the process flow inside the reactor.
- The OFC geometry has created a growing interest in the pharmaceutical industry, because of its great results in the crystallization field. However, this new geometry is not compatible with the PAT tools available. Due to its characteristics, the optical fiber sensors developed allowed the monitorization of the process parameters inside the OFC in a non-invasive way, contributing even more to the optimization of crystallization process of APIs, throughout the OFC.
- The optical fiber sensors developed are also an alternative and less expensive technology, compared to other PAT tools used in the crystallization field, such as the ATR probes.

1.4. List of publications

International journals

L. Soares, R. A. Pérez-Herrera, S. Novais, A. Ferreira, S. Silva, and O. Frazão, “Linear Fiber Laser Configurations for Optical Concentration Sensing in Liquid Solutions”, *Photonics*, vol.11, nº5, 393, Apr. 2024, DOI:10.3390/photonics11050393.

L. Soares, C. Cunha, S. Novais, A. Ferreira, O. Frazão, and S. Silva, "Refractive Index Measurements of Ethanol–Water Binary Liquid Solutions Using a Graded-Index Fiber Tip Sensor", *IEEE Sensors Letters*, vol.7, nº9, pp.1-4, Sept. 2023, DOI:10.1109/LSENS.2023.3303079.

L. Soares, R. A. Pérez-Herrera, S. Novais, A. Ferreira, O. Frazão, and S. Silva, “Paracetamol concentration-sensing scheme based on a linear cavity fiber laser configuration”, *Optical Fiber Technology*, vol.80, 103407, Oct. 2023, DOI:10.1016/j.yofte.2023.103407.

L. Soares, R. A. Pérez-Herrera, S. Novais, A. Ferreira, S. Silva, and O. Frazão, “Measurement of Paracetamol Concentration Using an Erbium-Doped Fiber Ring Cavity”, *Photonics*, vol.10, nº1, 50, Jan. 2023, DOI:10.3390/photonics10010050.

L. Soares, S. Novais, A. Ferreira, O. Frazão, and S. Silva, "Detection of the Crystallization Process of Paracetamol with a Multimode Optical Fiber in a Reflective Configuration", *Sensors*, vol.20, nº1, 87, Dec. 2019, DOI:10.3390/s20010087.

International and national conferences

L. Soares, S. Novais, A. Ferreira, O. Frazão, and S. Silva, "*In-situ* temperature monitorization in oscillatory flow crystallizer using optical fiber sensors with a Bragg grating inscribed at the fiber tips ends” in 12th European Optical Society Annual Meeting (EOSAM 2024), 9-13 Sept. 2023, Naples, Italy.

L. Soares, S. Novais, A. Ferreira, O. Frazão, and S. Silva, "Linear Cavity Fiber Laser configurations for refractive index measurements” in VI International Conference on Applications of Optics and Photonics (AOP 2024), 16-19 July 2024, Aveiro, Portugal.

L. Soares, S. Novais, A. Ferreira, O. Frazão, and S. Silva, “Tecnologia em fibra ótica para análise refratométrica de soluções binárias de etanol-água” in Encontro Ciência 2024, 3-5 July 2023, Porto, Portugal.

L. Soares, R. A. Pérez-Herrera, S. Novais, A. Ferreira, O. Frazão, and S. Silva, “Measurement of paracetamol concentration using a fiber laser system” in IEEE 7th Portuguese Meeting on Bioengineering (ENBENG 2023), 22-23 June 2023, Porto, Portugal, DOI: 10.1109/ENBENG58165.2023.10175344.

L. Soares, C. Cunha, S. Novais, A. Ferreira, O. Frazão, and S. Silva, "Refractive Index Measurements of Ethanol–Water Binary Liquid Solutions Using a Graded-Index Fiber Tip Sensor” in 11th European Optical Society Annual Meeting (EOSAM 2023), 11-15 Sept. 2023, Dijon, France, DOI: 10.1051/epjconf/202328709038.

L. Soares, A. Ferreira, O. Frazão, and S. Silva, “Optical fiber sensor to measure the concentration of Paracetamol in Crystallization experiments”, in 1st PRODEF Day, 11 Nov. 2022, Porto, Portugal.

L. Soares, A. Ferreira, O. Frazão, and S. Silva, “Quantitative analysis of paracetamol liquid solutions by Raman spectroscopy,” in 4th Doctoral Congress in Engineering (DCE2021), 28-19 June 2021, Porto, Portugal.

Other publications

P. Robalinho, V. Piaia, **L. Soares**, S. Novais, A. L. Ribeiro, S. Silva, and O. Frazão, “Phase-shifted fiber Bragg grating by selective pitch slicing”, *Sensors*, vol.24, n°21, 6898, Oct. 2024, DOI:10.3390/s24216898.

R. A. Pérez-Herrera, H. Diaz, **L. Soares**, S. Novais, M. Lopez-Amo, S. Silva, and O. Frazão, "Erbium-doped fiber ring cavity assisted by an FBG and PS-FBG reflector for refractive-index measurements,” in 11th European Optical Society Annual Meeting (EOSAM 2023), 11-15 Sept. 2023, Dijon, France, DOI:10.1051/epjconf/202328709012.

O. Frazão, P. Robalinho, A. Vaz, **L. Soares**, B. Soares, C. S. Monteiro, S. Novais, and S. Silva, "How to Use Fiber Optic Sensors for Accurate Absolute Measurements”, in 11th European Optical Society Annual Meeting (EOSAM 2023), 11-15 Sept. 2023, Dijon, France, DOI:10.1051/epjconf/202328709008.

R. A. Pérez-Herrera, **L. Soares**, S. Novais, O. Frazão, and S. Silva, "Erbium-doped fiber ring cavity for the measurement of refractive index variations”, in European Workshop on Optical Fibre Sensors (EWOFS 2023), 23-26 May 2023, Mons, Belgium, DOI:10.1117/12.2678101.

R. A. Pérez-Herrera, **L. Soares**, S. Silva, and O. Frazão, “Ring Cavity Erbium-Doped Fiber for Refractive Index Measurements”, *Sensors*, vol.22, n°23, 9315, Nov. 2022, DOI:10.3390/s22239315.

Chapter 2. Crystallization

2.1. Theoretical notions

Crystallization corresponds to a separation and purification process. It is responsible for 90% of the pharmaceutical industry products, the APIs, which correspond to crystals of small organic molecules [1, 2].

During this process, a phase change happens, and a solid product (a crystalline product) is obtained from a solution, i.e., from a mixture of two or more species that form a homogeneous single phase, which might be liquid, solid or gaseous [3].

The most common is the crystallization from a liquid solution (the mixture of a liquid solvent and a solid solute, forming a homogeneous phase). In this case, there is a maximum amount of solute, for a given pressure and temperature, that can be dissolved in the solvent, which is called solubility or concentration of saturation [3].

Solutions can be classified as unsaturated, saturated or supersaturated as the concentration of solute is less than, equal or greater than solubility, respectively. Regarding the crystallization process, it is essential that the solution in question is supersaturated, i.e., with a solute concentration higher than the saturation concentration [4].

As is represented in **Figure 2.1**, there are two consecutive steps that occur during crystallization: (1) nucleation and (2) crystalline growth.

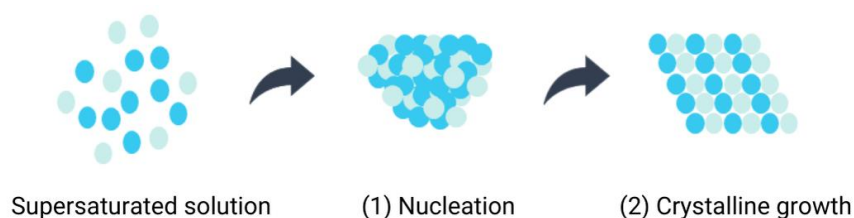


Figure 2.1. Schematic representation of the crystallization process. Adapted from [6].

(1) Nucleation corresponds to the union of the solute molecules, which are found in the supersaturated solution, until a stable aggregate is formed. When nucleation occurs in the absence of solute surfaces, it is called primary. However, when it is necessary to use particles from the

solute itself (seeds) to induce this process, the nucleation is called secondary. In the absence of agents foreign to the system, nucleation is classified as homogeneous, however, when using some type of interference or energy contribution, it is classified as heterogeneous [5, 6].

(2) Crystalline growth occurs after nucleation and is associated with the way nuclei grow, giving rise to the crystals. During this process, mass transfer happens, from the growth units (solute molecules present in the supersaturated solution) to the crystal/solution interface, and its incorporation into the crystal surface [6, 7].

At an industrial level, crystallization is a very attractive process, since it allows obtaining products with a purity greater than 99%, using reduced energy consumption, when compared to other processes [8, 9]. In addition, it is a process that allows the control of shape and the size of the final product. However, despite all these characteristics, crystallization is still a poorly understood and controlled process, since the available PATs are still limited [10-12].

2.2. Crystallization types

Crystallization can be reached by (1) cooling, (2) reaction, (3) evaporation and (4) change in solvent composition [13].

Crystallization induced by cooling is the most used in the industrial field and, in this work, it is the only approached [9].

According to the way of inducing crystallization/supersaturation, there are different geometries of crystallizers/reactors. The type of crystallizer selection is very important, because it has repercussions in the crystallization final product, namely, crystal size distribution, crystal median size and particles purity. To obtain a certain size of crystal and a specific crystal size distribution, it is mandatory a rigid control of the reactor and its operating conditions [9, 14, 15].

In the case of cooling crystallizers, they can regulate the cooling process such that the solution temperature drops below saturation. The solute becomes less soluble at lower temperatures, which causes excess solute to precipitate. Gradually, the lowering of temperature promotes nucleation, leading to the creation of crystal formations [9, 16].

The crystallization process can be designed for a non-continuous operation, called “batch”, or for a continuous operation. Regarding the type of operation, the crystallizers are different.

The main difference between batch and continuous crystallization is that in the batch system, the crystals are collected at the end of the batch run and in the continuous system, the crystallizer is continuously fed in an extremity, and the crystals are collected at an opposite one [9, 14].

2.2.1. Batch crystallization

Batch crystallization can be performed at the simplest geometry of crystallizers, similar to an open tank. It can be agitated (Stirred Tank Crystallizer – STC) and non-agitated, if it has a mechanical stirred or not, respectively (**Figure 2.2**) [16, 17].

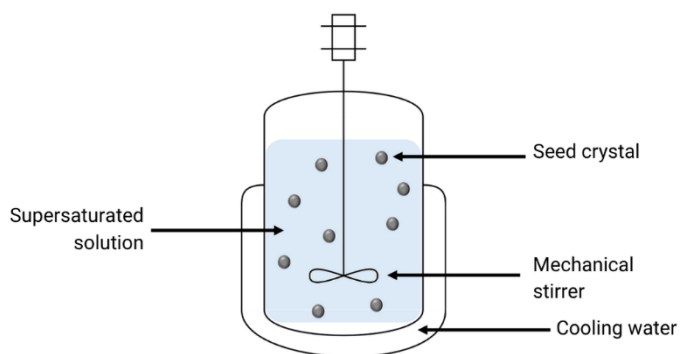


Figure 2.2. Representation of a Stirred Tank Crystallizer. Adapted from [16].

In a non-agitated crystallizer, the supersaturated solution is added inside the open tank and then, by natural convection, the solution cools down. In the case of STC, after the addition of a supersaturated solution, the mechanical stirred helps the mixing and the transference of heat and mass, i.e., the operating time is lower, as well as the labor cost [14, 16].

In terms of final product, STC geometry, although being more expensive, is the most attractive one, because of the uniformity of the crystal size. Since in a non-agitated crystallizer the cooling is slower, the crystals formed have higher dimensions and there is the retention of supersaturated solution, i.e., there is a loss of reagents, and the final product is impure [15].

Non-agitated crystallizers are generally not employed at the industrial scale due to their limited process control and scalability. In the pharmaceutical industry, however, crystallization is predominantly conducted in Stirred Tank Crystallizers (STCs), operated in batch mode. While batch crystallization has been extensively investigated and remains widely used, it is associated

with inherent disadvantages such as batch-to-batch variability and process inefficiency. These limitations have prompted growing interest in continuous crystallization as a means to enhance process control, consistency, and scalability [14, 15].

2.2.2. Continuous crystallization

As previously mentioned, the continuous crystallization process corresponds to a unit operation in which the process flow is continuously flowed into the crystallizer, and the crystals are continuously removed. According to the literature, this type of continuous process can save 9% to 40% of the production cost and, when compared with batch operation, continuous one can offer high production efficiency and reduce product variability without interruptions [14, 15].

In this type of crystallization, it is possible to provide more stable operating conditions, namely, temperature and concentration, during the whole process [15-17].

In the last years, the study of continuous manufacturing in the pharmaceutical industry has led to the development of new geometries of crystallizers, specifically for continuous crystallization. The OFC is one of the examples [9, 18].

Table 2.1 shows the main differences between batch and continuous crystallizations.

Table 2.1. Main differences between batch and continuous manufacturing [14, 15].

Crystallization	
Batch	Continuous
Batch manufacturing	Non-stop production cycle
Difficult to scale-up	Flexible scaling to match demands
High waste and operating costs (sometimes, entire batches can be ruined)	Ability to isolate small amounts of defective material to reduce waste

2.3. Geometries of continuous crystallizers: the Oscillatory Flow Crystallizer

There are two main categories of continuous crystallizers: the Mixed Suspension Mixed Product Removal (MSMPR) crystallizer and the Plug Flow Crystallizer (PFC).

Both crystallizers, MSMPR and PFC, depend on stirring mechanisms and turbulent flow conditions for mixing. As it is possible to see in **Figure 2.3**, the main differences between MSMPR

and PFC crystallizers are the design and the way crystals are formed and removed. **Table 2.2** summarizes the main characteristic of both types of crystallizers [14, 19, 20].

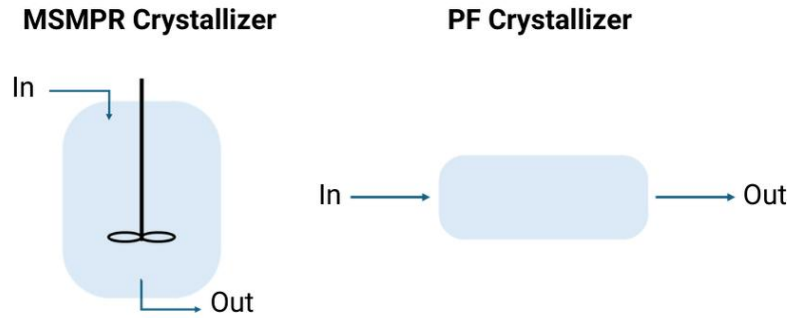


Figure 2.3. Schematic comparison between MSMPR and PF crystallizers. Adapted from [14].

Table 2.2. Characterizations of the main models of continuous crystallizers: Mixed Suspension Mixed Product Removal and Plug Flow Crystallizer [14, 19, 20].

	MSMPR	PFC
Design	Continuous mixing design: the crystal suspension and the solution are kept homogeneous	Unidirectional flow: the flow moves along the crystallizer such as a “plug”
Operating	The crystals are continuously removed while the supersaturated solution is fed	The crystals are sequentially formed along the geometry of crystallizer, and they are collected at its output
Advantages	Easily implemented in existing batch equipment; operation and control well established	Efficient and easy to scale-up; fine residence time distributions
Disadvantages	High localized shear regions due to agitators; non-uniform temperature control; Challenges with handling solids at transfer lines; in some cases, difficult to scale-up	Prone to incrustations and fouling
Applications	Used in processes where the crystal size uniformity is critical	Used in processes where the sequential formation of crystals is important

As previously mentioned, new geometries of crystallizers, based on MSMPR and PFC models, have been developed. OFC is one of the examples and it is a variant of the PFC.

OFC can be used for both manufacturing, batch and continuous, and it is composed of horizontal tubes or vertical columns [9, 15, 21].

In continuous manufacturing, OFC geometry has achieved great results in the crystallization of APIs, attracting the interest of more and more pharmaceutical companies. Contrary to MSMPR and PFC crystallizers, the OFC mechanism relies on the interaction between the oscillating fluid and baffles. A conventional OFC is a tubular crystallizer with equally spaced orifice baffles, where a periodically oscillating motion is applied on the liquid flow, as illustrated in **Figure 2.4** [22, 23].

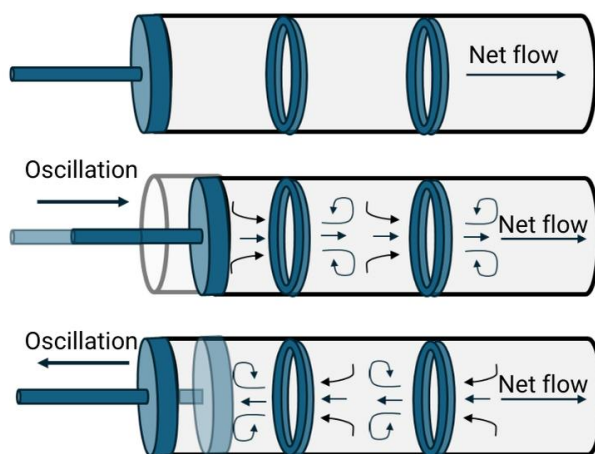


Figure 2.4. Representation of the oscillatory flow crystallizer operating principle. Adapted from [15].

The oscillating motion is created, in the axial direction (**Figure 2.4**), by moving baffles or moving fluid, by means of diaphragms, bellows or pistons, at one or both ends of the tube.

The interaction between the oscillating fluid and the baffles results in the generation and cessation of vortices, which provides both axial and radial mixing in the tube. This creates zones of uniform mixing in each inter-baffle cell, and the OFC itself can be regarded as a series of well mixed cells with an overall plug flow behavior [21-23].

There are different types of orifice baffles. In the case of continuous crystallization in an OFC, when they are designed with Smooth Periodic Constrictions (SPC), the results are better, i.e., OFCs with SPC generally require a lower amplitude of oscillation to create fully suspended solids. In this way, the intensification of the mixture is improved, as well as the heat and mass transfer, the particle mixing and separation, and the crystallization speed [24].

Despite these great results, there are some issues that have been reported, associated with the common OFC geometry, the tubular-OFC. The main problem is the formation of encrustations on the surfaces of the OFC tubes, which cause the loss of control and blockages, leading to the stoppage of crystallization process [25-27]. Due to this limitation, a new variant of OFCs has been developed: the planar-OFC, which combines the technology of a conventional tubular-OFC, however its design is rectangular rather than circular, as represented in **Figure 2.5** [28, 29].

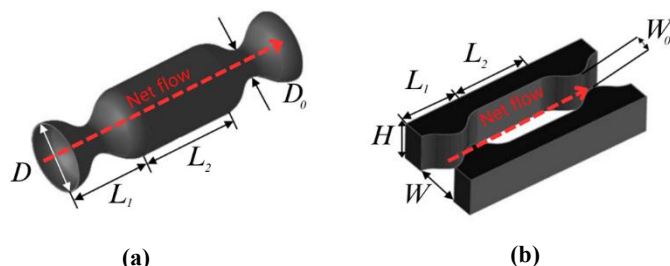


Figure 2.5. Difference between tubular and planar-OFCs with SPC baffles: (a) Tubular-OFC with SPC; (b) Planar-OFC with SPC. Where, D corresponds to the tube diameter in the straight section, D_0 is the tube diameter in the constriction, L_1 is the constriction length, L_2 is the straight section length, W is the channel width in the straight section, W_0 is the channel width in the constriction, and H is the channel height. Millimeter scale. Adapted from [29].

In a conventional tubular-OFC the SPC section is more elevated than the straight section, causing the restraints of the flow of solids along the tube and, as consequence, the accumulation of solids close to the constrictions. Since in the planar-OFC the SPC section and the straight section are at same level, this does not happen, i.e., the flow of solids along the channel is facilitated [27, 28].

Continuous crystallization in planar-OFCs has achieved great results related to: (1) more precise control of size and morphology of crystals; (2) high crystals grow rates and (3) reduction of waste. Due to the rise of continuous manufacturing in the pharmaceutical industry, the development and application of planar-OFCs has received significant attention in the past years [29, 30]. However, the crystallization of APIs in this type of geometry is not a common manufacturing procedure in the pharmaceutical industry, because the use of PAT in these crystallizers is still limited by the diameters of the probes, which typically exceed the diameter of the planar-OFCs channels [28].

In this thesis, the main subject will be the monitorization of APIs crystallization (namely, paracetamol – study case) in a planar-OFCs, operating at the milliliter scale. **Figure 2.6** illustrates this geometry of crystallizer. It is also identified which crystallization stages occur in each planar-OFC section (recall **Figure 2.1**).

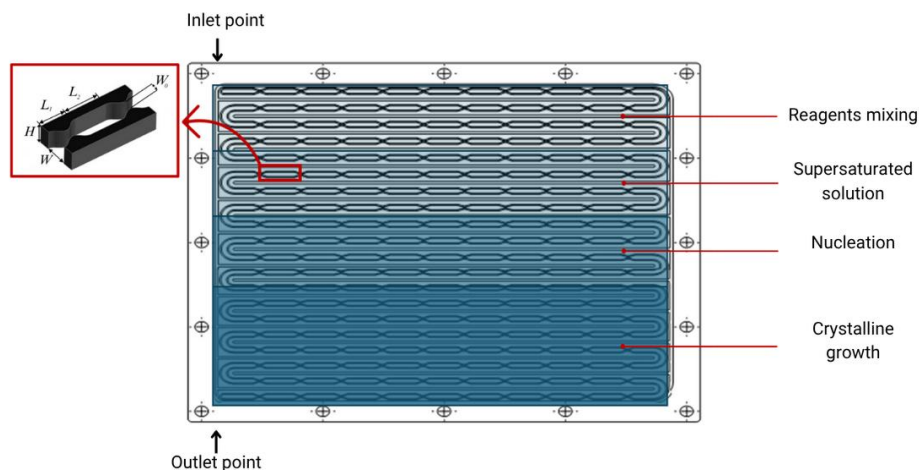


Figure 2.6. Representation of a planar-OFC with SPC and identification of the crystallization phases that occur in each crystallizer section.

2.4. Monitorization of crystallization process: PAT tools

The pharmaceutical industry is imposing a growing pressure for the development of new and optimized crystallizers that makes the crystallization process more efficient from the point of view of the consumption of reagents, solvents, energy, and space [31, 32].

As previously mentioned, scientific and technological advances have enabled the emergence of different geometries of crystallizers, of different sizes. However, the control of process parameters, namely, temperature or concentration, is a difficult task. PAT tools available for this purpose have dimensions incompatible with the dimensions of the crystallizer vessels, which makes real-time monitoring impossible and, consequently, makes it difficult to guarantee a final quality product [14, 18, 21, 28].

In the implementation of PAT tools for measuring variables of interest, sensors are used. Depending on their location, sensors can be classified into (1) offline, (2) online, (3) in line and (4) non-invasive [12].

When measurements are performed on a sample extracted from the process flow, the sensor is classified as “offline”. On the other hand, when measurements are performed in real-time, the sensor can be defined as “online” (the sample analyzed is deviated from the process flow and

returns to it), “in line” (measurements are made directly in the process flow because it can be disturbed) or “non-invasive” (the process flow is not disturbed by the measurements).

Regarding crystallization, sensors that enable real-time measurements are more advantageous compared to offline sensors, as they eliminate the need for sample preparation and allow continuous monitoring of the process, facilitating the identification of potential failures or errors.

Currently, the available PAT tools make real-time measurements in certain crystallizers impractical, as the crystallizer vessels are smaller than the probes, preventing them from being fully immersed in the process flow [12, 14].

2.4.1. Limitations of PAT tools

Optical probes are the most widely used PAT in terms of controlling the crystallization process of APIs. These tools are essentially based on spectroscopic fundamentals, and they can measure the size of particles, as well as the viscosity, speed and concentration of the process flow [33].

Appendix A presents a spectroscopy technique used to analyzed paracetamol samples in a “offline” way to determine its concentration.

Table 2.1 summarizes the main probes used in crystallization field and **Figure 2.7** to **Figure 2.10** illustrate the respective techniques.

Table 2.3. Resume of principal PAT tools used to monitor the crystallization process [34-37].

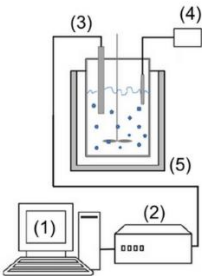
Illustration	Description
	Probes based on spectroscopy in the Near Infrared Reflectance (NIR), which are used to monitor in line and control the crystallization process of paracetamol by cooling [34].

Figure 2.7. Experimental setup for monitoring the crystallization process using NIR probe: (1) data acquisition system, (2) detector, (3) NIR probe, (4) temperature controller and (5) crystallizer. Adapted from [34].

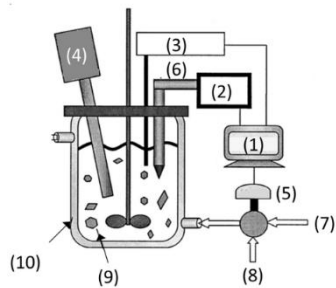


Figure 2.8. Experimental setup for monitoring the crystallization process using ATR-FTIR probe: (1) data acquisition system, (2) FTIR, (3) thermocoupler, (4) FBRM, (5) valve, (6) ATR probe, (7) and (8) hot and cold water, respectively, (9) solution and (10) jacketed vessel. Adapted from [35].

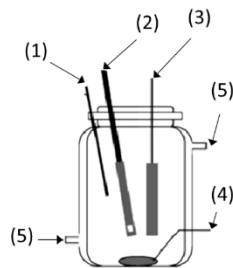


Figure 2.9. Schematic representation of the dielectric constant sensor setup for monitoring the crystallization process: (1) thermocouple, (2) turbidity probe, (3) dielectric constant probe, (4) magnetic stirred bar and (5) input and output sites of the crystallizer. Adapted from [36].

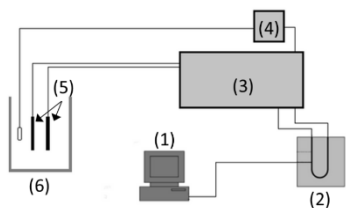


Figure 2.10. Experimental setup for concentration measurements in crystallizers using densitometers: (1) data acquisition system, (2) U-tube densitometer, (3) thermostat, (4) peristaltic pump, (5) metal filters and (6) crystallizer. Adapted from [37].

Probe based on Infrared spectroscopy with Attenuated Total Reflectance Fourier Transform (ATR-FTIR) used to monitor the dissolution dynamics in the crystallization system, from a perspective of mass counting, while a probe implemented with the technique of Focused Beam Reflectance Measurements (FBRM) allows the control of the size distribution of formed crystals, at the end of the crystallization process. Both measurements are performed online [35].

Sensor that studies the effects of temperature and solute concentration on the dielectric constant, allowing the identification of specific stages of crystallization. For the implementation of the dielectric constant sensor is also necessary a thermocouple, which, coupled with a water circulator, allows temperature control, and a magnetic stirrer for homogenizing the solution. The turbidity is measured by another sensor [36].

Densitometer allows the monitorization of the optical density of a solution and, consequently, its optical concentration. In addition to the densitometer (in this case a U-tube), it is necessary to implement an external circulation circuit. This circuit consists of two metallized filters, through which the process flow passes, alternately, from the crystallizer. The process flow is introduced into the circuit, due to the action of a peristaltic pump. The temperature of process flow is always monitored by a thermostat [37].

All the previous studies (**Table 2.3**) occur in crystallizers with simple geometries and similar to open tanks (STCs).

In literature, the same type of monitoring in other types of crystallizers, more complex, such as the planar-OFC, remains forgotten.

Due to the incompatible dimensions of PAT tools with the crystallizer's vessels, the crystallization process in planar-OFC is not control in an efficient way.

Additional disadvantages of the optical probes presented (**Table 2.3**) include their high commercial cost and the time-consuming nature of their operation, as they necessitate the integration of multiple signals. For a continuous and real-time monitoring of the various process parameters throughout the crystallization process, it is necessary to apply several and different probes, which cause the need of integrating different PAT signals [14].

In view of these limitations, the need for simpler and less expensive technology, which promotes a better knowledge and control of the crystallization process in continuous and in different geometries of crystallizers, immerses.

2.4.2. Fiber-optic based solutions as alternative to conventional PAT tools

Optical fiber-based sensors have characteristics that make them excellent detection tools, both for physical and biochemical parameters [38]. Regarding the pharmaceutical area, characteristics such as reduced dimensions, low weight, flexibility, low losses, no electromagnetic interference, multiplexing capacity and remote monitoring at specific spatial points (as a probe) or even in large areas (through multiple detection regions along the optical fiber), make this type of sensors an asset [39-42]. These sensors are low-cost, minimally invasive and can be placed in direct contact with the process flow – direct measures.

The direct measures eliminate the need for sampling and avoid associated problems, namely: (1) difficulty in accessing the sample; (2) presence of an unrepresentative sample and (3) need of a recurrent sampling process that changes the material (changes the process flow).

Some of the simplest optical fiber-based sensor configurations are fiber tips. They can have different geometries and can be used as refractometers to monitor concentrations of some chemicals.

A cone-shaped fiber tip was developed to detect local variations in the RI of samples under study. The results showed that this type of refractometer may be the ideal candidate for monitoring the variation of the RI in real-time, with a detection limit of 6.7×10^{-5} RIU [44]. Other fiber tip sensors have been fabricated and implemented. A spherical fiber tip (microsphere) with a sensitivity of 96.07 dB/RIU, and presenting good repeatability and accuracy, was proposed to measure RI. The results obtained showed that the sensor in question may have applicability in several areas, namely, in chemical, environmental and biomedical industries, due to its resistance to acid and alkalinity and due to its high mechanical resistance [44]. A hollow-core probe was fabricated to measure viscosity in small volumes of liquid. The probe consists of an air cavity, with a small access hole for fluids and functions as a two-wave interferometer [45]. Until now, Fiber Bragg Gratings (FBGs) have also been a fiber optic-based technology that is quite useful for many different techniques. For example, an FBG coated with an inorganic polymer was developed to measure the temperature during lyophilization, a critical parameter of the referred process. The results obtained allowed to prove the efficiency of the sensor to monitor the temperature in a non-invasive way and with greater sensitivity, more quickly and with better resolution, compared to other conventional techniques. The same authors also affirmed the possibility of integrating a glass fiber with several sensors in series, to create several temperature measurement points, during the lyophilization process. In this study, and in addition to temperature control, it was also possible to monitor other events of a chemical nature, such as crystallization [46].

In literature, it is possible to find other studies related to the crystallization process, however, only related to the crystallization of proteins [47] and salts [48]. The monitorization of APIs crystallization using fiber optic technology remains forgotten.

In view of the results found in literature, it is believed that optical fiber tip sensors can measure different variables of interest, namely, RI, concentration and temperature. This fiber-optic based technology may present high potential as a PAT tool, allowing the measurement of process parameters in real-time, throughout the crystallization of APIs in different geometries of crystallizers.

References

- [1] N. Saleemi, *Strategic feedback control of pharmaceutical crystallization systems*, Loughborough University: England, UK, 2011.
- [2] J. Chen, B. Sarma, J. B. Evans, and A. Myerson, "Pharmaceutical Crystallization", *Cryst. Growth Des.*, vol.11, n°4, pp.887-895, Feb. 2011, DOI:10.1021/cg101556s.
- [3] A. M. Schwartz, and A. S. Myerson, "Solutions and solution properties". In *Handbook of Industrial Crystallization*, 2nd ed., ch.1, pp.1-31, Butterworth-Heinemann: Oxford, UK, 2002.
- [4] J. M. Coulson, and J. F. Richardson, "Crystallization". In *Chemical Engineering*, 5th ed., ch. 15, p.84, Butterworth-Heinemann: Oxford, UK, 2013.
- [5] J. W. Mullin, "Nucleation". In *Crystallization*, 4th ed., pp 181–215, Butterworth Heinemann: Oxford, UK, 2001.
- [6] A. S. Myerson, and R. Ginde, "Crystals, crystal growth, and nucleation". In *Handbook of Industrial Crystallization*, 2nd ed., ch. 2, pp.33-65, Butterworth-Heinemann: Oxford, UK, 2002.
- [7] J. W. Mullin, "Crystal Growth". In *Crystallization*, 4th ed., pp. 216–288, Butterworth-Heinemann: Oxford, UK, 2001.
- [8] A. B. Haan, and H. Bosch, *Industrial Separation Processes: Fundamentals*, Walter de Gruyter GmbH: Berlin, 2013.
- [9] Z. Gao, S. Rohani, J. Gong, and J. Wang, "Recent Developments in the Crystallization Process: Toward the Pharmaceutical Industry", *Engineering*, vol.3, n°3, pp.343-353, June 2017, DOI:10.1016/J.ENG.2017.03.022.
- [10] M. Birch, S. Fussell, P. Higginson, N. McDowall, and I. Marziano, "Towards a PAT-Based Strategy for Crystallization Development", *Org. Process Res. Dev.*, vol.9, n°3 pp.360-364, Apr. 2005, DOI:10.1021/op0500077.
- [11] L. L. Simon, H. Pataki, G. Marosi, F. Meemken, K. Hungerbühler, A. Baiker, S. Tummala, B. Glennon, M. Kuentz, G. Steele, H. J. M. Kramer, J. W. Rydzak, Z. Chen, J. Morris, F. Kjell, R. Singh, R. Gani, K. V. Gernaey, M. Louhi-Kultanen, J. O'Reilly, N. Sandler, O. Antikainen, J. Yliruusi, P. Froberg, J. Ulrich, R.D. Braatz, T. Leyssens, M. von Stosch, R. Oliveira, R.B.H. Tan, H. Wu, M. Khan, D. O'Grady, A. Pandey, R. Westra, E. Delle-Case, D. Pape, D. Angelosante, Y. Maret, O. Steiger, M. Lenner, K. Abbou-Oucherif, Z. K. Nagy, J.

-
- D. Litster, V. K. Kamaraju, and M.-S. Chiu, "Assessment of Recent Process Analytical Technology (PAT) Trends: A Multiauthor Review", *Org. Process Res. Dev.*, vol.19, n°1, pp.3–62, Jan. 2015, DOI:10.1021/op500261y.
- [12] L. Yu, R. Lionberger, A. Raw, R. D'Costa, H. Wu, and A. Hussain, "Applications of process analytical technology to crystallization processes", *Adv. Drug Deliv. Rev.*, vol.56, n°3, pp.349–369, Feb. 2004, DOI:10.1016/j.addr.2003.10.012.
- [13] A. Mersmann, *Crystallization Technology Handbook*, 1st ed., CRC Press: New York, 2001.
- [14] D. Zhang, S. Xu, S. Du, J. Wang, and J. Gong, "Progress of Pharmaceutical Continuous Crystallization", *Engineering*, vol.3, n°3, pp.54–364, June 2017, DOI:10.1016/J.ENG.2017.03.023.
- [15] J. Orehek, D. Teslić, and B. Likozar, "Continuous Crystallization Processes in Pharmaceutical Manufacturing: A Review", *Org. Process Res. Dev.*, vol.25, n°1, pp.16-42, Dec. 2020, DOI:10.1021/acs.oprd.0c00398.
- [16] R. D. Braatz, and S. Hasebe, "Particle Size and Shape Control in Crystallization Processes". In *Proceedings of the 6th International Conference of Chemical Process Control*, pp.307-327, Jan. 2001, Tucson, Arizona.
- [17] D. Dallinger, and C. O. Kappe, "Why Flow Means Green – Evaluating the Merits of Continuous Processing in the Context of Sustainability", *Curr. Opin. Green Sustain. Chem.*, vol.7, pp.6-12, Oct. 2017, DOI:10.1016/j.cogsc.2017.06.003.
- [18] T. Wang, H. Lu, J. Wang, Y. Xiao, Y. Zhou, Y. Bao, and H. Hao, "Recent Progress of Continuous Crystallization", *J. Ind. Eng. Chem.*, vo.54, pp.14-29, Oct. 2017, DOI:10.1016/j.jiec.2017.06.009.
- [19] S. Y. Wong, A.P. Tatusko, B. L. Trout, and A. S. Myerson, "Development of Continuous Crystallization Processes Using a Single-Stage Mixed-Suspension, Mixed-Product Removal Crystallizer with Recycle", *Cryst. Growth Des.*, vol.12, n°11, pp.5701–5707, Oct. 2012, DOI:10.1021/cg301221q.
- [20] G. Cogoni, B. P. de Souza, and P. J. Frawley, "Particle Size Distribution and yield control in continuous Plug Flow Crystallizers with recycle", *Chem. Eng. Sci.*, vol.138, pp.592–599, Dec. 2015, DOI:10.1016/j.ces.2015.08.041.

-
- [21] T. McGlone, N. E. B. Briggs, C. A. Clark, C. J. Brown, J. Sefcik, and A. J. Florence, "Oscillatory flow reactors (OFRs) for continuous manufacturing and crystallization", *Org. Process Res. Dev.*, vol.19, n°9, pp.1186–1202, Aug. 2015, DOI:10.1021/acs.oprd.5b00225.
- [22] A. W. Fitch, H. Jian, and X. Ni, "An Investigation of the Effect of Viscosity on Mixing in an Oscillatory Baffled Column Using Digital Particle Image Velocimetry and Computational Fluid Dynamics Simulation", *Chem. Eng. J.*, vol.112 n°1–3, pp.197–210, Sept. 2005, DOI:10.1016/j.cej.2005.07.013.
- [23] S. Lawton, G. Steele, P. Shering, L. Zhao, I. Laird, and X.-W. Ni, "Continuous Crystallization of Pharmaceuticals Using a Continuous Oscillatory Baffled Crystallizer", *Org. Process Res. Dev.*, vol.13, n°6, pp.1357–1363, Nov. 2009, DOI:10.1021/op900237x.
- [24] L. N. Ejim, S. Yerdelen, T. McGlone, I. Onyemelukwe, B. Johnston, A. J. Florence, and N. M. Reis, "A Factorial Approach to Understanding the Effect of Inner Geometry of Baffled Meso-Scale Tubes on Solids Suspension and Axial Dispersion in Continuous, Oscillatory Liquid–Solid Plug Flows", *Chem. Eng. J.*, vol.308, pp.669–682, Jan. 2017, DOI:10.1016/j.cej.2016.09.013.
- [25] N. E. B. Briggs, U. Schacht, V. Raval, T. McGlone, J. Sefcik, and A. J. Florence, "Seeded Crystallization of β -L-Glutamic Acid in a Continuous Oscillatory Baffled Crystallizer", *Org. Process Res. Dev.*, vol.19, n°12, pp.1903–1911, Oct. 2015, DOI:10.1021/acs.oprd.5b00206.
- [26] L. R. Agnew, T. McGlone, H. P. Wheatcroft, A. Robertson, A. R. Parsons, and C. C. Wilson, "Continuous Crystallization of Paracetamol (Acetaminophen) Form II: Selective Access to a Metastable Solid Form", *Cryst. Growth Des.*, vol.17, n°5, pp.2418–2427, May 2017, DOI:10.1021/acs.cgd.6b01831.
- [27] R. Peña, J. A. Oliva, C. L. Burcham, D. J. Jarmer, and Z. K. Nagy, "Process Intensification through Continuous Spherical Crystallization Using an Oscillatory Flow Baffled Crystallizer", *Cryst. Growth Des.*, vol.17, n°9, pp.4776–4784, July 2017, DOI:10.1021/acs.cgd.7b00731.
- [28] A. Ferreira, F. Rocha, J. A. Teixeira, and F. Castro, "Modular Oscillatory Flow Plate Reactor", PT 109314 H, 2016; PCT/IB2017/052005, 2017; US 16/092,010, EP3439773, 2018.
- [29] P. Cruz, C. Silva, F. Rocha, and A. Ferreira, "The axial dispersion of liquid solutions and solid suspensions in planar oscillatory flow crystallizers", *AIChE Journal*, vol.65, n°9, e16683, June 2019, DOI:10.1002/aic.16683.

-
- [30] P. Cruz, F. Rocha, and A. Ferreira, "Crystallization of paracetamol from mixtures of ethanol and water in a planar oscillatory flow crystallizer: effect of the oscillation conditions on the crystal growth kinetics", *CrystEngComm*, vol.23, n°47, pp.8301-8314, Oct. 2021, DOI:10.1039/D1CE00858G.
- [31] S. Lawton, G. Steele, P. Shering, L. Zhao, I. Laird, and X. W. Ni, "Continuous crystallization of pharmaceuticals using a continuous oscillatory baffled crystallizer", *Org. Process Res. Dev.*, vol.13, n°6, pp.1357-1363, Oct. 2009, DOI:10.1021/op900237x.
- [32] F. Castro, A. Ferreira, F. Rocha, and A. Teixeira, "Precipitation of Hydroxyapatite at 37°C in a Meso Oscillatory Flow Reactor Operated in Batch at Constant Power Density", *AIChE Journal*, vol.59, n°12, pp.4483-4493, July 2013, DOI:10.1002/aic.14193.
- [33] X. Li, C. Yang, S. Yang, and G. Li, "Fiber-Optical Sensors: Basics and Applications in Multiphase Reactors", *Sensors*, vol.12, n°9, pp.12519-12544, Sept. 2012, DOI:10.3390/s120912519.
- [34] I. -C. Wang, M. -J. Lee, D. -Y. Seo, H. -E. Lee, Y. Choi, W. -S. Kim, C. -S. Kim, M. -Y. Jeong, and G. J. Choi, "Polymorph Transformation in Paracetamol Monitored by In-line NIR Spectroscopy During a Cooling Crystallization Process", *AAPS PharmSciTech.*, vol.12, n°2, pp.764-770, June 2011, DOI:10.1208/s12249-011-9642-x.
- [35] D. J. Griffin, Y. Kawajiri, R. W. Rousseau, and M. A. Grover, "Using MC plots for control of paracetamol crystallization", *Chem. Eng. Sci.*, vol.164, pp.344-360, June 2017, DOI:10.1016/j.ces.2017.01.065.
- [36] M. W. Hermanto, G. He, M. Tjahjono, P. S. Chow, R. B. H. Tan, and M. Garland, "Calibration of dielectric constant measurements to improve the detection of cloud and clear points in solution crystallization", *Chem. Eng. Res. Des.*, vol.89, n°12, pp.2613-2619, Dec. 2011, DOI:10.1016/j.cherd.2011.04.012.
- [37] J. Worlitschek, and M. Mazzotti, "Model-Based Optimization of Particle Size Distribution in Batch-Cooling Crystallization of Paracetamol", *Cryst. Growth Des.*, vol.4, n°5, pp.891-903, Feb. 2004, DOI:10.1021/cg034179b.
- [38] Z. Y. Zhang, and K. T. Grattan, "Survey of US patent activity in optical fiber sensors". In *Optical Fiber Sensor Technology: Introduction and Overview*, Springer: Boston, MA, 2000, DOI:10.1007/978-1-4757-6081-11.

-
- [39] R. Correia, R. Sinha, A. Norris, S. Korposh, S. Talbot, F. U. Hernandez, and S. P. Morgan, "Optical fiber sensing at the interface between tissue and medical device". In Proceedings of the *International Conference on Biophotonics V*, 103400X, Apr. 2017, Perth, Australia. DOI:10.1117/12.2269811.
- [40] S. Silvestri, and E. Schena, "Optical-Fiber Measurement Systems". In *Optoelectronics: Devices and Applications*, P. Predeep, Ed. Rijeka, Croatia: InTech, pp.205–224, 2011.
- [41] S. Silva, P. Roriz, and O. Frazão, "Refractive Index Measurements of Liquids Based on Microstructured Optical Fibers", *Photonics*, vol.1, n°4, pp.516-529, Dec. 2014, DOI:10.3390/photonics1040516.
- [42] R. Y. Shah, and Y. K. Agrawal, "Introduction to fiber optics: Sensor for biomedical applications", *Indian J. Pharm. Sci.*, vol.73, n°1, pp.17-22, Jan. 2011, DOI:10.4103/0250-474X.89752.
- [43] H. Nikbakht, H. Latifia, T. Aminib, and M. L. Zibaiia, "Tip Sensor Probe for Changing Refractive Index Measurement in Small Volumes", *Int. J. Opt. Photonics*, vol.8, n°2, pp.105-111, July 2014, Corpus ID:8020494.
- [44] M. Li, Y. Liu, S. Qu, and Y. Li, "Fiber-optic sensor tip for measuring temperature and liquid refractive index", *Optical Engineering*, vol.53, n°11, pp.116110(1)-116110(5), Nov. 2014, DOI:10.1117/1.OE.53.11.116110
- [45] A. D. Gomes, J. Kobelke, J. Bierlich, K. Schuster, H. Bartelt, and O. Frazão, "Optical Fiber Probe Viscometer Based on Hollow Capillary Tube", *J. Lightwave Technol.*, vol.37, n°18, pp.4456-4461, Sept. 2019, DOI:10.1109/JLT.2019.2890953.
- [46] J. C. Kasper, M. Wiggernhorn, M. Resch, and W. Friess, "Implementation and evaluation of an optical fiber system as novel process monitoring tool during lyophilization", *Eur. J. Pharm. Biopharm.*, vol.83, n°3, pp.449-459, Apr. 2013, DOI:10.1016/j.ejpb.2012.10.009.
- [47] R. R. Ansari, K. I. Suh, A. Arabshahi, W. W. Wilson, T. L. Bray, and L. J. DeLucas, "A fiber optic probe for monitoring protein aggregation, nucleation and crystallization", *J. Cryst. Growth*, vol.168, n°1–4, pp.216-226, Oct. 1996, DOI:10.1016/0022-0248(96)00357-0.
- [48] M. Boerkamp, D. W. Lamb, and P. G. Lye, "An intrinsic exposed core optical fiber sensor as a quantitative surface crystallization monitoring sensor", *Sens. Actuators B: Chem.*, vol.177, pp.964-969, Feb. 2013, DOI:10.1016/j.snb.2012.12.020.

Chapter 3. Optical fiber sensors

The development of optical fibers revolutionized the area of telecommunications, especially from the 1970s. Fiber optic-based technology quickly gained ground in the development of sensors, which stimulated its application in the most varied fields: biochemical, biological, environmental, biomedical, engineering and industrial [1].

There are many advantages of optical fibers that make the Optical Fiber Sensors (OFSs) excellent and promising detection tools, namely, reduced dimensions, low weight, flexibility, biocompatibility, low losses, are not influenced by electromagnetic interference, high degrees of integration, providing real-time measurements in a non-invasive and non-destructive way [2, 3].

Over the past few decades, OFSs reveal to be reliable, cost-effective and to have a high degree of sensitivity, when compared to other traditional sensors [4].

3.1. Optical fiber concept

The optical fiber is considered one of the biggest accomplishments in a technological field from the 20th century and has demanded a great effort on its development, both at a structural and material level.

The main base of fiber optic technology is the light orientation principle, established for the first time in 1840 by Colladon and Babinet. According to them, the light could be directed, and they prove it using a running water, which they called the "light fountain" [5].

In this way, optical fiber can transmit codified data in a light beam, without significative losses, through a phenomenon called total internal light reflection [6].

3.1.1. Structural and material characterization

The optical fiber corresponds to a flexible and transparent filament that can be made by glass or plastic. In relation to optical fiber geometry, it essentially corresponds to (1) core, (2) cladding and (3) coating, as is shown in **Figure 3.1**.

Since only glass fibers were used in this work, the following characterization refers exclusively to them.

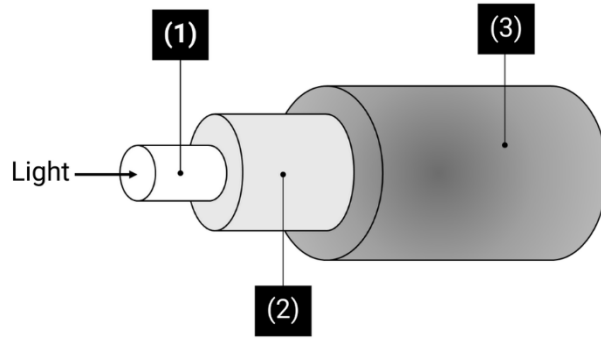


Figure 3.1. Schematic representation of an optical fiber. Adapted from [7].

The core is a dielectric, transparent medium, where light propagation occurs. The cladding typically has a diameter of $125\text{ }\mu\text{m}$ and is generally made of transparent glass. This structure, besides keeping the light inside the core, increases the fiber mechanical strength, and protects the core from contaminants. It also reduces light losses by transmission and scattering (optical fiber intrinsic losses, due to structural defects). Lastly, the coating is a plastic element, with a $250\text{ }\mu\text{m}$ diameter, whose principal responsibility is to protect the optical fiber from humidity and from thermal, mechanics and chemical effects [7, 8].

3.1.2. Physical operating mechanism

The light propagation along the fiber occurs through the physical principle of total internal reflection. The fiber core and the cladding have different refractive index (RI). To occur the total internal reflection and the light can propagate along the fiber, as expected, there are some conditions that must be satisfied: (1) the cladding RI must be lower than the core RI and (2) the light incident angle at the core-cladding interface must be higher than a certain angle – the critical angle [7].

A conventional optical fiber has a cladding made of silica and a core made of silica doped with germanium. The RI of these structures, cladding and core, is ~ 1.444 and ~ 1.468 RIU, respectively, for a wavelength of 1550 nm . Due to the optical properties of these constituent materials, the incident light is kept inside the fiber core, and it can propagate along the fiber, through successive total internal reflections, i.e., the fiber acts as a light guide [7, 8].

- **Total internal reflection and critical angle**

The RI of a certain medium is determined by the ratio between the speed of light in vacuum and the speed of light in the referred material [8].

When a light beam reaches the boundary of two different materials, i.e., with different RI, a physical phenomenon called light refraction happens – **Figure 3.2**.

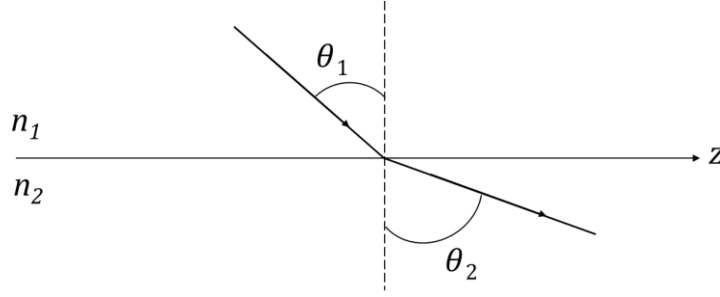


Figure 3.2. Light refraction representation. Adapted from [8].

In **Figure 3.2**, n_1 e n_2 correspond to the RI of media (1) and (2), respectively. The incident light propagates in medium 1 and reaches the interface created by medium (1) - medium (2) with an incident angle equal to θ_1 , relative to the normal of the interface created by the media.

When n_1 is higher than n_2 , the refracted light propagates at medium (2) with an angle, θ_2 , higher than the incident angle, θ_1 . This happens because medium (2) is optically less dense than medium (1), i.e., $n_1 > n_2$, and, therefore, the light propagates through medium (2) at higher speed, moving away from the normal to the plane of the medium's interface [8].

The relation between the incident angle, θ_1 , and the refraction angle, θ_2 , is given by Snell's Law, represented in **Equation 3.1**.

$$n_2 \sin \theta_2 = n_1 \sin \theta_1 \quad (3.1)$$

According to Snell's Law, a change in the direction of light propagation is proportional to the difference between the RI of media (1) and (2). Furthermore, when the incident angle (θ_1) increases, the refraction angle (θ_2) also increases, until a limit: when the refraction angle (θ_2) is

equal to 90° , in relation to the normal created by the media' interface. This limit is called critical angle (**Figure 3.3 a**).

The critical angle (θ_c) is determined through **Equation 3.2**, which is based on the Snell's Law, previously presented [8].

$$\theta_c = \sin^{-1}\left(\frac{n_2}{n_1}\right) \quad (3.2)$$

For incident angles higher than θ_c and $n_1 > n_2$, the light is totally reflected at the interface created between the media (1) and (2), as illustrated in **Figure 3.3 (b)**. In this case, a physical phenomenon called total reflection happens, which is the basic operating principle of fiber optic technology, as previously reported [7, 8].

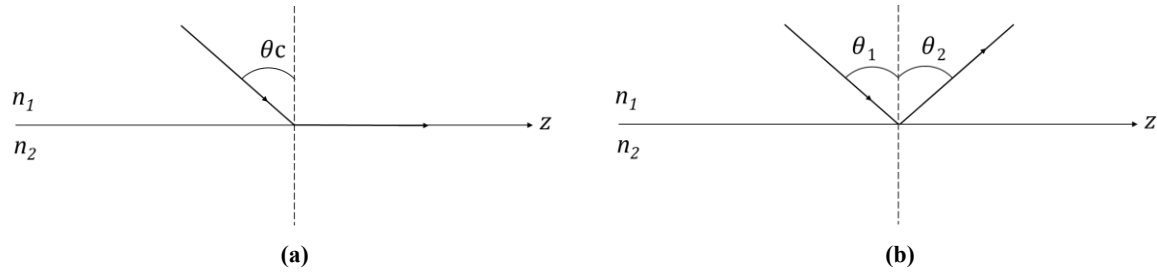


Figure 3.3. Total reflection: **(a)** critical angle; **(b)** total reflection representation. Adapted from [8].

- **Acceptance cone and light propagation within an optical fiber**

There are three different RIs at the entrance of an optical fiber: the RI of the medium that makes boundary with the optical fiber, n_0 , the RI of optical fiber core, n_{co} , and the RI of optical fiber cladding, n_{cl} . As illustrated in **Figure 3.4**, light reaches the boundary between the external medium and the optical fiber, with an angle \emptyset_0 . Passing by this boundary, the light is refracted with an angle of \emptyset_1 and it starts to propagate inside the fiber. The light is guided along the fiber through successive reflections, with an angle of θ_1 .

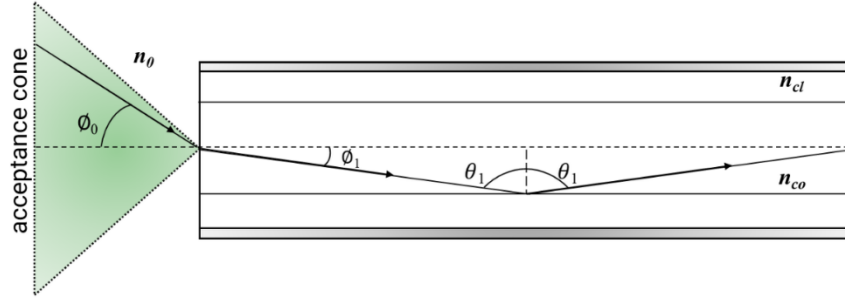


Figure 3.4. Schematic representation of the acceptance cone. Adapted from [8].

The phenomenon of total internal reflection inside the fiber can be performed by different incident angles, ϕ_0 . As illustrated in **Figure 3.4**, these angles can be identified through the acceptance cone. After the light refraction at the interface between the external medium, with a RI of n_0 , and the fiber core, with a RI of n_{co} , light beams with angles greater than the critical angle ($\theta_1 > \theta_c$) are reflected by total internal reflection at the interface created by the fiber core and cladding. In this way, light beams with angles smaller than the critical angle ($\theta_1 < \theta_c$), i.e., angles that do not belong to the acceptance cone, pass through the fiber coating (**Figure 3.4**).

- **Numerical aperture**

There is a relation between the fiber core RI, n_{co} , and the cladding RI, n_{cl} , which allows the characterization of the optical fiber numerical aperture [8].

The numerical aperture, NA , is a dimensionless quantity that evaluates the optical fiber capability to capture the light, and it ranges from 0.15 to 0.5 (**Equation 3.3**).

$$NA = \sqrt{n_{co}^2 - n_{cl}^2} \quad (3.3)$$

A numerical aperture close to 0.5 is associated with a high coupling rate between optical source and the optical fiber, but also to a high difference between normalized RIs. In this way, optical fibers with a higher numerical aperture have a higher capability to collect light, but also a higher tendency to promote light dispersion and attenuation (losses), because they can support different modes of propagation [7, 8].

3.2. Optical fiber classification

Optical fibers can be classified as Single-Mode Fiber (SMF) and Multimode Fiber (MMF), according to the number of modes that the fiber can support [8].

The modes of an optical fiber correspond to the guided electromagnetic waves that describe the light propagation along the fiber. Each mode has a specific pattern of electric and magnetic field distribution, which is repeated along the fiber at equal intervals.

SMF has a core with a small diameter, between 8 and 12 μm , and it can only support one mode of propagation. On the other hand, MMF has a core with higher dimensions, typically diameters of 50, 62 and 110 μm , and it support several modes of propagation [7, 8].

Optical fibers can be also classified according to their RI profile. SMF has a Step-Index (SI) profile, and MMF can have a SI or a Graded-Index (GI) profile.

At a SI profile, the fiber core RI is uniform and different from the cladding RI. In this way, the total internal reflection only occurs between the interface created by the core and cladding. At a GI-MMF profile, the core RI is not constant. It progressively decreases from the core central axis to its borders (interface core – cladding) and, for this reason, the path of light is helical [8].

Figure 3.5 resumes the main types of optical fiber and illustrates their RIs profiles.

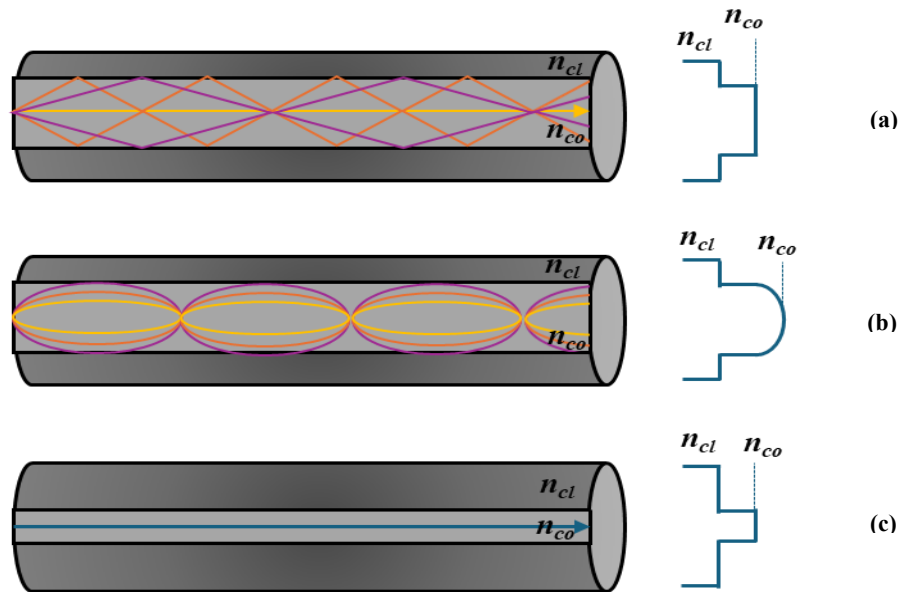


Figure 3.5. Refractive index profiles of optical fibers: (a) SI-MMF; (b) GI-MMF; (c) SMF. n_{co} and n_{cl} correspond to the core and to the cladding RIs, respectively. Adapted from [8].

3.3. Optical fiber as a sensing tool

A sensor corresponds to a device that responds in a specific way to a certain signal or external stimulus. The sensor response generally corresponds to an electrical, optical, or mechanical signal, which is then converted into a physical or biochemical parameter that can be measured and/or monitored [1].

The sensors are classified according to the type of energy measured. Regarding OFSs, they detect alterations of optical parameters, according to the variations of physical or biochemical parameters of the measured medium, i.e., the OFSs measure the alterations suffered by the light, caused by external stimulus (tension, pressure, temperature, concentration or chemical composition) [9].

The implementation of OFSs often requires the use of fiber optic technology, due to its interesting characteristics, especially, reduce dimensions, low weight, biocompatibility, high sensitivity, simple geometry, low implementation cost, easy integration and multiplexing capabilities [1-4].

Generically, a fiber optic-based sensing system is based on three principal elements: an (1) optical source, (2) a sensing element and a (3) detector.

The (1) optical source is responsible for the transmission of electromagnetic radiation, which energy is transmitted until the sensing element. The (2) sensing element allows the alteration of light properties, according to the measured medium, and the (3) detector is the element that collects and analyzes the light perturbations, caused by the variations of the measured medium [1, 9].

3.4. Classification of optical fiber sensors

OFSs can be classified through different ways. However, there are two main categories: (1) intrinsic sensors and (2) extrinsic sensors [9].

In the (1) intrinsic sensors, the sensing element is the optical fiber itself (the fiber works as a sensor). In this way, the external stimulus acts directly into the fiber, changing the optical properties of the light guided by the fiber. On the other hand, the (2) extrinsic sensors direct the light, coming from a given measured medium, to a detector, i.e., the external stimulus acts in an external region, in relation to optical fiber. The fiber only works as a light signal transmitter. The input fiber transmits the signal to the sensing element, though optical or electric components, and the information is then transmitted by the sensing element to the output fiber, which guides the

light to the detector. The detector collects and analyzes the light, allowing the interpretation of information contained in it [9].

There are other OFSs classifications, according to: modulation process (phase, polarization, wavelength and intensity), working principle (fiber attenuation, end coupling, bending loss, fiber interferometers, grating structures and scatterings), operating application (temperature, RI, humidity, strain, pressure, curvature, pH, and others) and spatial cope (single-point, multipoint or distributed) [1, 9, 10].

In this dissertation the optical fiber sensors modulated in intensity will be the one discussed in more detail.

3.5. Intensity modulated sensors

Intensity sensors are the first generation of optical fiber sensors and, besides their simplicity, they are used in several low-cost applications. In this case, the intensity of the light that propagates along the fiber is modulated. Usually, a physical perturbation, namely, pressure, strain and temperature, causes a variation in the intensity of the transmitted light. In this way, these sensors are capable of detecting variations in the amount of light, according to alterations in the measuring medium [9].

Figure 3.6 represents a generic system of an optical fiber sensor modulated in intensity. The light is transmitted by the optical source and then it is coupled to fiber. After that, the light is transmitted to the sensing head and modulated in intensity. This process can occur in two different modes: (1) reflection and (2) transmission [8-10].

In a reflection mode, the optical signal is reinjected again into the fiber and transmitted to the detector, which is generally implemented in the same emission unit. On the other hand, in a transmission mode it is necessary to use a second fiber path to guide the signal to the detector.

In this dissertation, the optical fiber sensors presented work in the reflection mode.

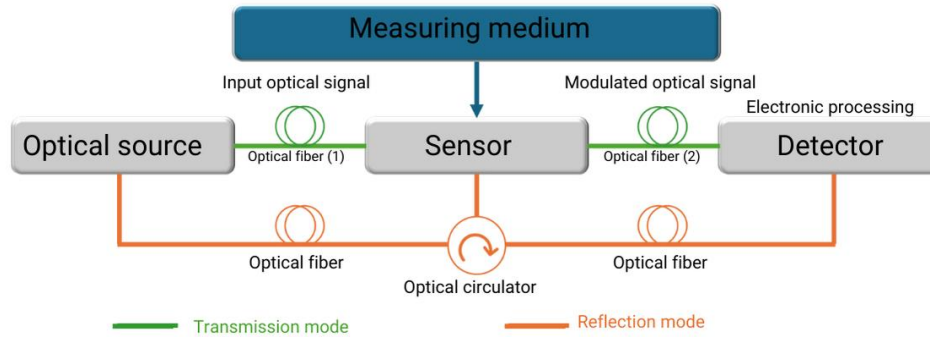


Figure 3.6. Generic representation of an optical fiber sensor modulated in intensity. Adapted from [9].

Although being commonly used, intensity sensors have some disadvantages, especially associated with optical losses. The intensity of radiation that propagates along the optical fiber is not totally conserved: it suffers losses. These losses can be intrinsic losses, associated with fiber structural defects and caused by scattering, absorption and dispersion of light, or they can be extrinsic losses, associated with operating conditions, splicing losses, connector losses or curvature losses [8, 9]. When dealing with these types of sensors, it is also important to consider the fluctuations of the light source intensity and the changes in the environmental conditions as factors that can induce errors in the measurements.

References

- [1] P. Roriz, O. Frazão, A. Lobo-Ribeiro, J. L. Santos, and J. A. Simões, “Review for Fiber-Optic Pressure Sensors for Biomedical and Biomechanical Applications”, *J. Biomed Opt.*, vol.18, n°5, 050903, May 2014, DOI:10.1117/1.jbo.18.5.050903.
- [2] P. Lu, N. Lalam, M. Badar, B. Liu, B. T. Chorpening, M. P. Buric, and P. R. Ohodnicki, “Distributed optical fiber sensing: Review and perspective”, *Appl. Phys. Rev.*, vol.6, n°4, 041302, Oct. 2019, DOI:10.1063/1.5113955.
- [3] R. Min, Z. Liu, L. Pereira, C. Yang, Q. Sui, and C. Marques, “Optical fiber sensing for marine environment and marine structural health monitoring: A review”, *Opt. Laser Technol.*, vol.140, 107082, Mar. 2021, DOI:10.1016/j.optlastec.2021.107082.

-
- [4] P. Gong, X. Li, X. Zhou, Y. Zhang, N. Chen, S. Wang, S. Zhang, and Y. Zhao, “Optical fiber sensors for glucose concentration measurement: A review,” *Optics & Laser Technology*, vol.139, 106981, Jan. 2021, DOI:10.1016/j.optlastec.2021.1069.
- [5] J. D. Colladon, “The Colladon Fountain”, *Sci. Am.*, vol.51, n°23, pp.359-360, Dec. 1884, DOI:10.1038/scientificamerican12061884-359a.
- [6] K. Ehrlich, H. E. Parker, D. K. McNicholl, P. Reid, M. Reynolds, V. Bussiere, G. Crawford, A. Deighan, A. Garrett, A. Kufcsák, D. R. Norberg, G. Spennati, G. Steele, H. Szoor-McElhinney, and M. Jimenez, “Demonstrating the Use of Optical Fibres in Biomedical Sensing: A Collaborative Approach for Engagement and Education”, *Sensors*, vol.20, n°2, 402, Jan. 2020, DOI: 10.3390/s20020402.
- [7] B. Saleh and M. Teich, *Fundamentals of Photonics*, 3rd ed., John Wiley & Sons: Hoboken, USA, 2019.
- [8] G. Keiser, *Optical fiber communications*, 1st ed., Springer Singapore: New York, USA, 2021.
- [9] J. L. Santos, and F. Farahi, *Handbook of optical sensors*, 1st ed., CRC Press: Florida, USA, 2014.
- [10] M. M. A. Eid, “Optical fiber sensors: review of technology and applications”, *Indones. J. Electr. Eng. Comput. Sci.*, vol.25, n°2, pp.1038–1046, Feb. 2022, DOI:10.11591/ijeecs.v25.i2.pp1038-1046.

Chapter 4. Optical fiber tips for refractive index sensing

4.1. Introduction

Optical fiber-based sensors have characteristics that make them excellent detection tools, both for physical and biochemical parameters [1]. Characteristics such as reduced dimensions, low weight, flexibility, low losses, no electromagnetic interference, multiplexing capacity and remote monitoring at specific spatial points (as a probe) or even in large areas (through multiple detection regions along the optical fiber), makes this type of sensors an asset for several sensing applications [2–5]. These sensors are also low-cost, minimally invasive and can be placed in direct contact with the medium under analysis. These direct measurements eliminate the need for sampling and avoid associated problems, namely, difficulty in accessing the sample, presence of an unrepresentative sample, and need of a recurrent sampling process that changes the material.

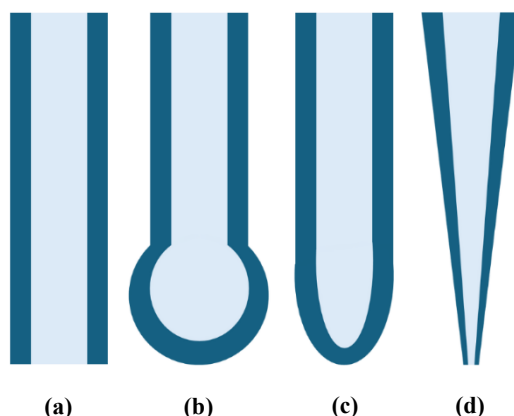


Figure 4.1. Schematic representation of different geometries of optical fiber tips sensors: **(a)** Cleaved; **(b)** Spherical; **(c)** Hemispheric; **(d)** Conical. Adapted from [6-18].

Some of the simplest optical fiber-based sensor configurations are fiber tips. These can have different geometries (**Figure 4.1**), and they are specially used as refractometers to monitor concentrations of some chemicals. However, according to literature, fiber tips can be used to detect other parameters. **Table 4.1** shows the different applicability of optical fiber tip sensors, with different configurations, in several areas, namely, in chemical, environmental and biomedical industries.

Table 4.1. Different configurations of optical fiber tip sensors reported in literature.

Year	Sensing head	Parameter	Application field	Reference
2008	conical multimode fiber tip	pH	biosensing applications	[6]
2010	tapered fiber tip	RI	biosensing applications	[7]
2012	hollow glass microsphere fiber tip	RI	chemical-sensing	[8]
2013	multimode half-taper fiber tip	temperature	oil exploration, high-power electrical systems and tunnel fire alarms	[9]
2014	cone-shaped fiber tip	RI	chemical, environmental and biomedical industries	[10]
2014	spherical fiber tip	RI	chemical, environmental and biomedical industries	[11]
2018	spherical fiber tip	RI, temperature	industry and medicine	[12]
2018	coreless silica fiber tip	RI, concentration	disease diagnosis, clinical analysis and quality monitor in food industry	[13]
2019	hollow-core fiber tip	viscosity	industry, chemistry, biology and pharmacy	[14]
2021	hollow-core fiber tip	temperature	industrial production and applications	[15]
2021	single-mode fiber tip	RI, concentration	chemical and biomedical industries	[16]
2022	tapered fiber tip	RI	Biomedical applications	[17]
2023	convex cone fiber tip	optical trapping	bioscience and medical research	[18]

As is possible to see in **Table 4.1**, optical fiber tips sensors experienced many applications in several fields during the last years. In the biomedical field, optical fiber tips represent a less invasive method with a high degree of biocompatibility. Also, these optical structures can be applied in the chemical industry, because they are able to detect the presence of specific analytes and control other process parameters, such as pH, viscosity, temperature, RI and concentration.

In **Table 4.1** the most referred parameter is RI. This happens because, in the past several years, RI measurement has performed an important role in several processing industries, such as, pharmaceutical, chemical, biological, medical, food industry and environmental [19, 20]. The growth of research and development in this field is driven by the need for quality control, which is often required by the end consumer. In this way, the development of refractometric sensors and

their improvement is a constant concern. In this chapter are presented two different geometries of optical fiber tips sensors for RI sensing.

4.2. Graded-index fiber tip sensor for refractometric analysis of ethanol-water binary solutions

Ethanol is a unique substance because it is miscible in non-polar and polar substances (such as water). This makes ethanol an element used as a solvent in several industries, namely, chemical, pharmaceutical and fuel industries [20, 21]. Especially in the fuel industry, ethanol has been receiving a lot of attention, because it can be used as a non-petroleum-based energy source, through the fermentation of sucrose. In this process, and in similar ones, the control of water present in ethanol is fundamental for the commercialization of the final product [22].

Nowadays, the laboratorial analyses performed to control the quality of ethanol-based products are time consuming and this is the main reason for the need for new monitoring systems [23].

In this way, the growth of research and development of this type of technology is driven by the need for fast and reliable results that can ensure quality control, reducing the product cost and the possibility of human errors, during the industry processes [21, 23].

Refractometric analyses are frequently used to determine the quality of a product, because the RI is a physical property used in the characterization and identification of liquid purity. However, the refractometric analysis of binary solutions of ethanol-water are difficult. These solutions present deviations from linear behavior and particular physical-chemical properties, when compared with ideal solutions [24].

The mixture of a hydrophobic solute, such as ethanol, in an aqueous solution, water, creates a non-common increase of entropy, which is associated with the formation of hydrogen bonding clusters. Because of this, the RI of the binary solutions of ethanol-water has a non-linear variation with the increase of ethanol concentration. There is a critical value, associated with a concentration of ethanol in solution, from which the determination of RI, i.e., the determination of ethanol proportion in the solution, is very ambiguous and difficult [21, 24].

To investigate hydrophobic interactions, present in these binary solutions of ethanol-water, ultrasonic detection has been applied. Also, some configurations of optical fiber sensors have been proposed to analyze aqueous primary alcohol mixtures, such as ethanol [21]. Some of the

configurations reported are usually based on a transmission scheme and have wavelength modulation, namely, etched Fiber Bragg Gratings [25], Long Period Gratings [26], two-mode interferometric probes [27] and Fabry-Perot interferometers [28]. However, they are used in a limited range of concentrations and conditions [21].

Despite the high sensitivity of wavelength-modulated sensors, they required complicated technology, and their measurement ranges are limited by high cross response to temperature and RI, which does not happen with intensity-modulated sensors [29, 30].

A multimode Graded-Index Fiber (GI-MMF)-based tip sensor, modulated in intensity, was developed to perform RI measurements of binary solutions of ethanol-water, for the range between 0 and 100% (v/v) of ethanol in water. This type of multimode fiber, GI-MMF, was chosen because it has higher bandwidth, lower attenuation than, for instance, Step-Index Fiber, which results in an improved performance and efficiency [31].

4.2.1. Sensing head and experimental setup

The sensing head developed for the ethanol-water samples measurements consists of a 500 μm GI-MMF section (GIF 625, core diameter of 62.5 μm and cladding diameter of 125 μm) spliced to a SMMF (SMF 28e, core and cladding diameters of 8.2 μm and 125 μm , respectively) and interrogated in reflection.

The GI-MMF was spliced to the SMF using a splicer machine (TYPE-72C, Sumitomo Electric) thus forming GI-MMF-based fiber tip. It should be noted that, before the splicing process, the coating from the fibers was removed using cutting pliers, followed by cleaning with acetone and/or ethanol. After that, the uncoated and cleaned end of the fibers was placed in a cleaver machine (FC-6RS, Sumitomo Electric). This way it was possible to ensure a perfect cut, as well as the perpendicularity of the cut surface (cleaved) in relation to the fiber axis (90°).

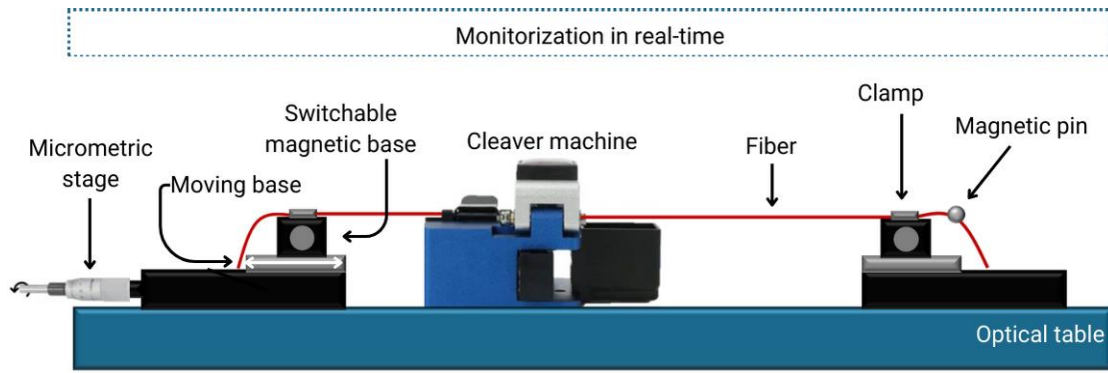


Figure 4.2. Schematic representation of the GI-MMF tip cleavage setup.

The specific and accurate length of the GI-MMF was achieved using a setup with a micrometric translation stage (**Figure 4.2**). In this way, the precise cut of the tip and, consequently, the sensor operating mechanism, were ensured. The fiber (SMF + GI-MMF) was clamped between two magnetic bases, ensuring that the SMF+GI-MMF spliced point was precisely aligned with the blade of the cleaver machine. The second clamp secured the end of the fiber between two magnetic pins, ensuring that it was under tension. When the fiber was correctly placed, the micrometric driver (151-411ME-H, Thorlabs) was engaged and rotated until the desired length was achieved (500 μm). As a result, the magnetic base, which was supporting the fiber, also moved, and it was possible to cleave the fiber with the desired length. Before this step, it was important to keep the cleaver machine open to facilitate the movement of the fiber (SMF+GI-MMF). The micrometric driver used had a travel range of 50 mm, with 10 μm travel, per division. The full procedure was monitored in real-time by an image acquisition program.

The interrogation system used is shown in Figure 4.3. An optical Broadband Source (BBS), with a central wavelength at 1550 nm, a bandwidth of 100 nm and an output power of 10 mW, was connected to an Optical Spectrum Analyzer (OSA, YOKOGAWA, model AQ6370D), by means of an optical circulator, to observe the spectral response of the sensing head. During the RI measurements, the OSA was replaced by an optical power meter (model Agilent 8163B).

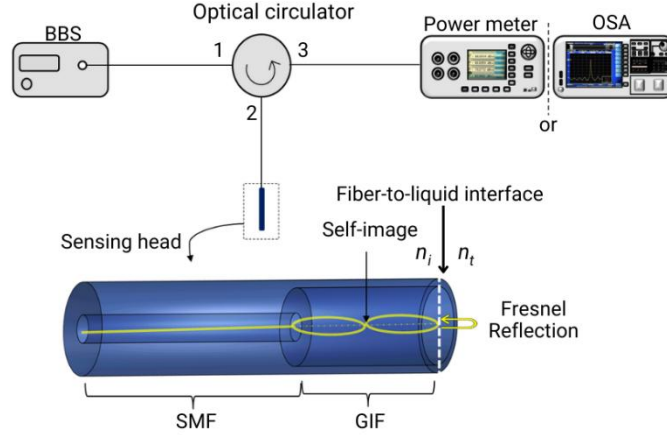


Figure 4.3. Scheme of the experimental setup used and detail of the sensing head.

The sensing head operating mechanism relies on the self-imaging phenomenon that occurs in a specific length of the GI-MMF used, in this case 500 μm . The light propagates through the incoming fiber, a standard SMF, and then it enters in a section of the GI-MMF, which self-focuses (self-image) the light beam. It should be noticed that a small variation (microns) in the GI-MMF length can lead to the loss of the self-image point. Concerning the fiber end, the GI-MMF was cleaved to ensure the Fresnel reflection.

As it is possible to see in **Figure 4.3**, the light is partially reflected when it reaches the surroundings. In this way, the measurement of RI variations is achieved with the intensity changes of the reflected optical signal. In this experiment, the ratio between the reflected light in the fiber-to-liquid interface and the incident light (Reflectance, R) can be estimated through the Fresnel equation for a reflection at a normal incidence, i.e., when the incident angle is equal to zero [32]:

$$R = \left(\frac{n_t - n_i}{n_t + n_i} \right)^2 \quad (4.1)$$

where n_i corresponds to the RI of the optical fiber core ($n_i = 1.468$ RIU) and n_t corresponds to the RI of liquid solutions ($n_t > 1$ RIU). According to **Equation 4.1**, less than 4% of the light guided by the fiber is reflected at the fiber-to-liquid interface monitored.

4.2.2. Output spectrum

The output spectrum of the configuration used, when the fiber tip is only in contact with air, at room temperature ($\sim 20^\circ\text{C}$), was obtained using the OSA – **Figure 4.4 (a)**.

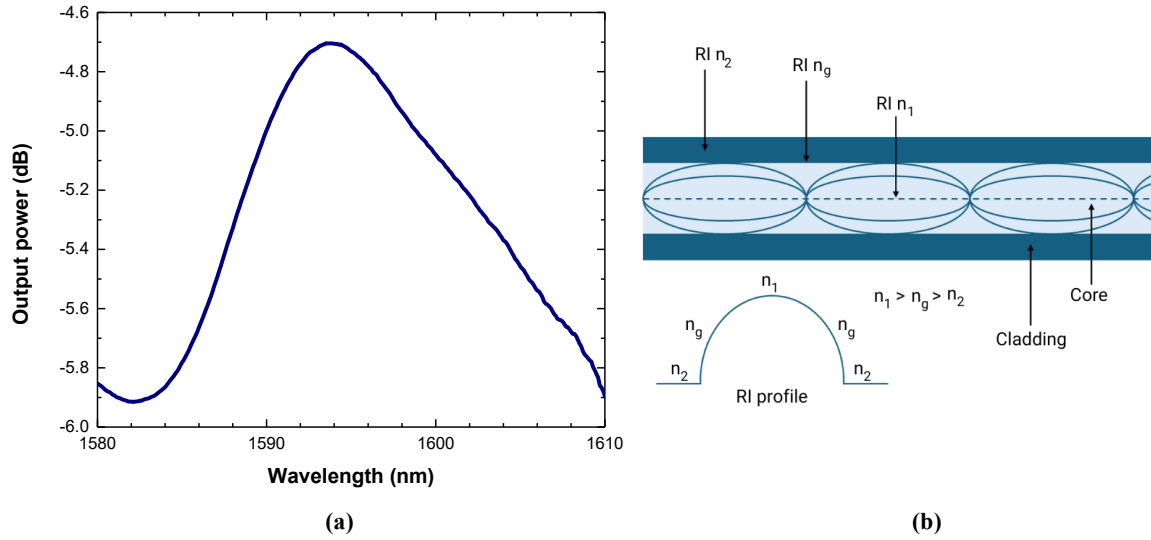


Figure 4.4. Characterization of a GI-MMF-based fiber tip: **(a)** Output spectrum; **(b)** Schematic representation of a GI-MMF refractive index profile, where n_1 corresponds to the fiber core refractive index, n_2 to the fiber cladding refractive index and n_g to the interface between the fiber core and cladding. Adapted from [33].

The output spectrum obtained shows the parabolic RI profile of a GI-MMF – **Figure 4.4 (b)**. The spectral analysis allowed to determine the losses produced by the developed sensing head, namely, ~ 30 dB.

4.2.3. Measurements of ethanol-water binary solutions

The RI measurements were performed using a set of 11 binary liquid solutions of ethanol-water (30 mL), for the range between 0 and 100% (v/v) of ethanol in water. The samples were prepared under a controlled laboratory environment, at room temperature ($\sim 20^\circ\text{C}$), using deionized water and ethanol-96%. The samples were stirred for 10 min, using a magnetic stirred (NAHITA), and then they were stored for 2 hours, for stabilization.

- **Calibration**

Initially, a RI characterization of the ethanol-water mixtures, at room temperature ($\sim 20^\circ\text{C}$) was performed. The RI was measured using an Abbe refractometer (ATAGO DR-A1) and the output power for each sample was obtained using the optical power meter (recall **Figure 4.3**). During the measurements, the sensing head was vertically immersed in each sample. **Figure 4.5** shows the relation between the RI of each sample and the output power measured by the sensor developed. To avoid contamination, the samples were measured in increasing order of % ethanol.

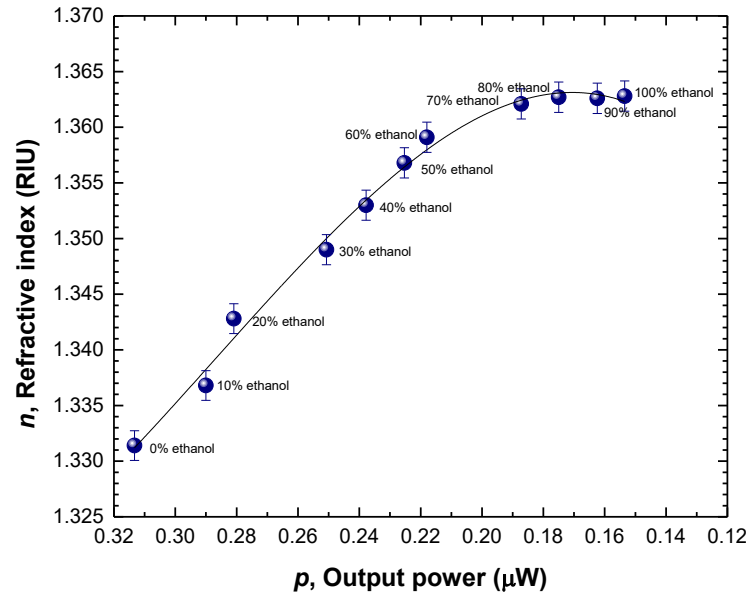


Figure 4.5. Characterization of ethanol-water binary liquid solutions at room temperature ($\sim 20^\circ\text{C}$).

A third-order polynomial approximation of the obtained measurements (**Figure 4.5**) was carried out. The data of this approximation is shown in **Table 4.2**.

Table 4.2. Parameters obtained by a third-order polynomial approximation when varying the %(v/v) of ethanol present in the ethanol-water binary liquid solutions properties ($n = a_0 + a_1p + a_2p^2 + a_3p^3$).

	a_0	a_1	a_2	a_3
Value	1.248	1.568	-6.543	7.602
Standard Error	$\pm(4.30 \times 10^{-2})$	$\pm(5.84 \times 10^{-1})$	2.568	3.670
R²	0.990			

As expected, the results show the non-linear dependence of the RI with the increase of ethanol concentration, which characterizes the ethanol-water mixtures [24]. The samples' refractive index increases when the ethanol concentration rises from 0% (v/v) to, approximately, 80% (v/v). Above this critical value, the RI decreases and, consequently, there is difficulty in the correlation between RI and ethanol concentration. This behavior is also reflected in the output power variations measured by the sensor, since the intensity variation of the reflection at the fiber-to-liquid sample interface is directly related to the RI of the sample. With the increase of RI, the intensity of the reflection is lower, as it is possible to see in **Figure 4.5**. In a common solution, with the increase of ethanol concentration, it should be expected a RI increase and an output power decrease. This result shows the ambiguity referred to in literature, associated with these ethanol-water mixtures [21, 24].

• Refractive index determination

The binary liquid solutions of ethanol-water were measured using the developed experimental setup (**Figure 4.3**). The sensing head was vertically immersed in each sample and the output power was obtained through the optical power meter. The samples were measured at different temperatures (20°C to 60°C). For that, each sample was subjected to a water-bath. The optical response obtained during the measurements is shown in **Figure 4.6 (a)**.

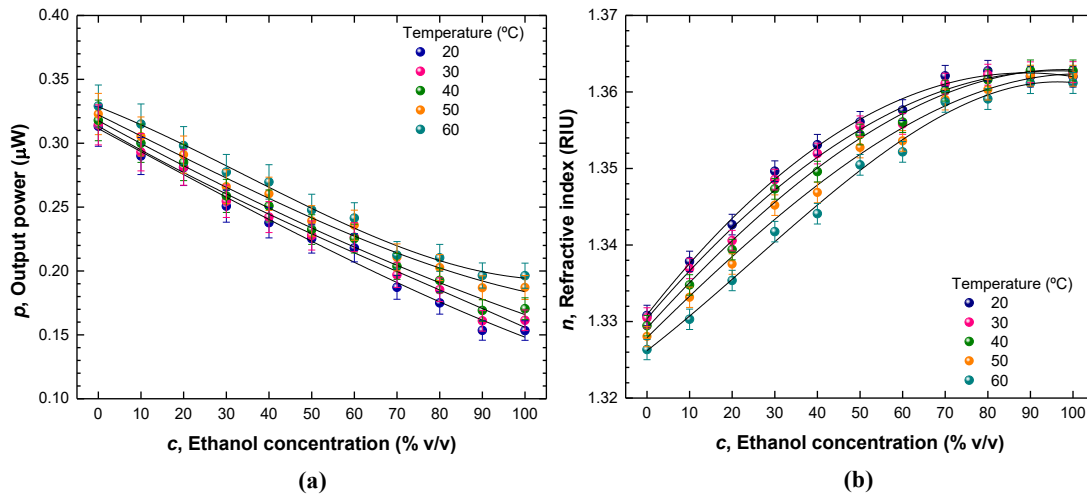


Figure 4.6. Refractive index dependence with ethanol concentration and temperature variations: **(a)** Fiber tip output power response for each sample measurement; **(b)** Refractive index determination of the ethanol-water samples at different temperatures.

The RI of each sample was determined using the previous calibration performed (**Figure 4.4**). As it is possible to see in **Figure 4.6 (b)**, the RI variation, according to the ethanol concentration (% v/v of ethanol in the sample), was fitted with a third-order polynomial function with coefficients of determination equal to or higher than 0.990 (**Table 4.3**).

Table 4.3. Determination of samples' refractive index. Functions of the third-order polynomial approximation when varying the %(v/v) of ethanol present in the ethanol-water binary liquid solutions at different T , temperature ($n = a_0 + a_1p + a_2p^2 + a_3p^3$).

T (°C)	Function	R^2
20	$n = 1.33 + (7.09 \times 10^{-4})p - (3.97 \times 10^{-6})p^2 - (1.38 \times 10^{-10})p^3$	0.993
30	$n = 1.33 + (6.55 \times 10^{-4})p - (3.13 \times 10^{-6})p^2 - (1.87 \times 10^{-9})p^3$	0.991
40	$n = 1.33 + (6.14 \times 10^{-4})p - (1.95 \times 10^{-6})p^2 - (8.08 \times 10^{-9})p^3$	0.993
50	$n = 1.33 + (5.50 \times 10^{-4})p - (8.03 \times 10^{-7})p^2 - (1.26 \times 10^{-8})p^3$	0.990
60	$n = 1.33 + (4.31 \times 10^{-4})p - (2.40 \times 10^{-6})p^2 - (3.20 \times 10^{-8})p^3$	0.992

The results show the non-linear dependence of RI with the increase of ethanol concentration, principally above the critical value, 80% (v/v) of ethanol in the mixture, which is not expected for a common solution. This phenomenon is associated with the ethanol-water clusters formation [24]. Also, it is possible to visualize that with the increase of temperature, for the same ethanol concentration in solution, the RI decreases. The temperature increase causes a reduction in the intermolecular interactions' intensity and a speed of light increase in the propagation medium [21]. As a result, the RI decreases, as is shown in **Figure 4.6 (b)**.

4.2.4. Influence of temperature

To evaluate the influence of temperature, as an external factor, in the sensor output power response, the sensing head was placed in an oven (especially designed for optical fiber tips sensors) and it was subject to temperature variations ($\sim 25^\circ\text{C}$ to 50°C). During the heating, the sensing head was only in contact with air and the output power response was obtained using an optical power meter (see **Figure 4.3**).

Figure 4.7 shows that the sensor measurements are not affected by the temperature as an external factor. The output power response remains approximately constant ($\sim 0.8 \mu\text{W}$), which proves that the sensor response is only related to the RI variations.

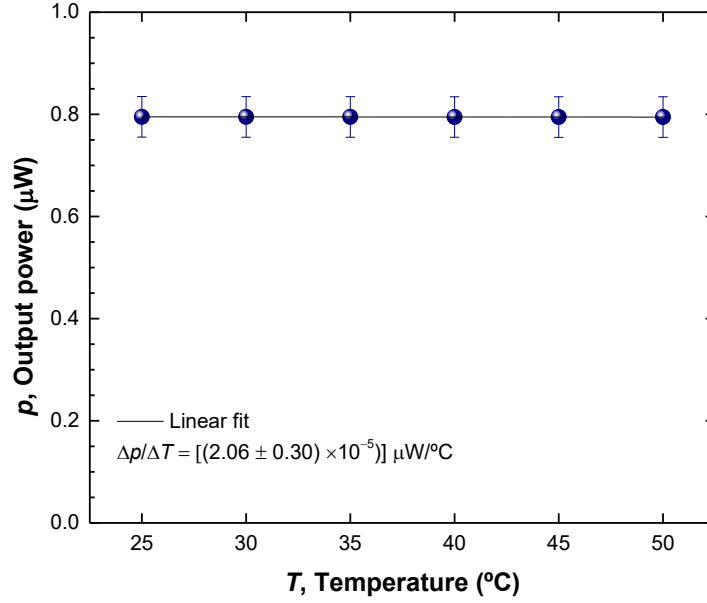


Figure 4.7. Influence of temperature, as an external factor, in the sensor output power response.

4.2.5. Concluding remarks

A GI-MMF-based tip sensor was developed and experimentally demonstrated to measure the RI of ethanol-water binary solutions. The sensing device was first calibrated using ethanol-water mixtures with different %(v/v) of ethanol in water and with known RI, measured at 20°C. Then, samples of ethanol-water mixtures with a range of ethanol %(v/v) between 0 and 100% were measured and characterized using the GI-MMF-based tip sensor, by varying its temperature between 20°C and 60°C (samples subjected to a controlled water-bath). The sensor response was determined through the measure of intensity variations of Fresnel reflection at the fiber-to-liquid sample interface.

The experimental results indicated that the developed sensor can be used to perform RI measurements of ethanol-water mixtures, even above the critical value of 80% (v/v) of ethanol concentration, eliminating the limitations associated to the ethanol concentration range referred in the literature, for other optical fiber sensors. It should be highlighted that the optical fiber sensor response was stable at different temperatures. This proves the sensor efficacy in measuring RI, regardless of temperature variations, as an external factor.

In this way, the developed sensor configuration can be used to perform in-line measurements of RI for the purpose of process control in several industries that use ethanol as a reagent.

4.3. Graded-index fiber tip sensor for crystallization process detection

Crystallization is one of the oldest processes used for the purification and separation of solid products. This process always involves a phase change and generally it allows a solid product (a crystal) to be obtained from a liquid solution, although the same can occur from a molten mixture or even a gas [34].

Crystallization is commonly used by several industries, including food, microelectronics, bulk, and fine chemicals and pharmaceuticals. Regarding the pharmaceutical field, crystallization is used to produce 90% of its products, the APIs [35, 36].

Generically, APIs are formed from a liquid solution, i.e., a mixture of a liquid solvent and a solid solute, forming a homogeneous phase. There is a maximum amount of solute, for a given pressure and temperature, that can be dissolved in the solvent, which is called solubility or saturation concentration [34]. To occur crystallization and the formation of a crystal, it is essential that the solution in question is supersaturated, that is, with a solute concentration higher than the saturation concentration [34, 37].

Usually, the most critical and least understood process of crystallization is the one associated with the APIs that have multiple polymorphic forms, such as the paracetamol.

Compounds can crystallize under different crystalline structures. In the specific case of paracetamol (**Figure 4.8**), there are three types of polymorphs: stable form I (monoclinic), metastable form II (orthorhombic), and unstable form III [38].

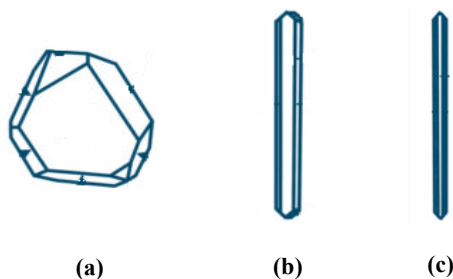


Figure 4.8. Schematic representation of paracetamol polymorphs: (a) Stable form I – Monoclinic; (b) Metastable Form II – Orthorhombic; (c) Unstable Form III. Adapted from [39].

During the crystallization process, there are several process parameters, such as crystallization surface, temperature and humidity, that can influence the properties and the quality of the final product, namely, the purity, the morphology, the crystalline phase, the size and, especially, the polymorph formed. In this way, it is important to have an appropriate design and control of crystallization methods [40, 41].

Regarding paracetamol, its crystallization displays a peculiar behavior. In 2012 a large comparison was demonstrated between several experimental conditions and crystallization patterns [42]. It was concluded that the enclosed samples were dominated by bulk crystallization into form III and the disclosed samples were outweighed by surface crystallization into forms I and II. This shows the importance of conducting a study survey on the characterization of polymorphs and crystallization process monitoring.

Despite being a very attractive process at an industrial level, crystallization is still a poorly understood and controlled process, especially, for APIs with polymorphism [43-46].

In this work, a simple configuration of a refractometer sensor based on a cleaved multimode fiber (MMF) tip, GI type, was implemented to monitor in real-time the crystallization process of an API, the paracetamol, by means of intensity variation based on the fiber tip–interaction concept.

4.3.1. Sensor characterization and operating mechanism

The proposed sensor corresponds to a refractometric sensor, modulated in intensity, and it is based on a section of a GI-MMF (10 cm fiber-length), with core and cladding diameters of 62.5 μm and 125 μm , respectively (see **section 4.2.1**), spliced to a SMF 28e (core and cladding diameters of 8.2 μm and 125 μm , respectively) – **Figure 4.9**. For this process, the coating of the fibers was removed, using cutting pliers, and after that the fibers were cleaned with ethanol. The uncoated fibers were then subjected to a cleaver machine (FC-6RS, Sumitomo Electric) to ensure a perfect perpendicular cut at the fiber-ends. The last step was the fibers splicing, using a splicer machine (TYPE-72C, Sumitomo Electric).

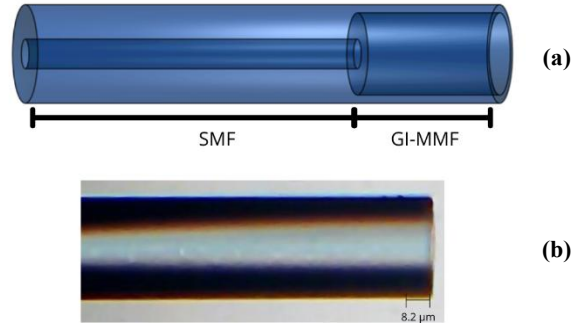


Figure 4.9. Sensor characterization: **(a)** Schematic diagram of the sensing head; **(b)** Microscope image of the multimode fiber.

It is important to notice that the end of the GI-MMF was also cleaved to obtain Fresnel reflection at the fiber tip (see **section 4.2.1**). The GI-MMF-based fiber tip configuration was chosen to ensure a higher amount of the reflected optical signal due to the larger area of the core. The operating mechanism of the fiber probe relies on the measurand-induced intensity variation of the Fresnel reflection at the fiber-to-interface monitored at a selected spectral window [32]. Upon reaching the surroundings, the light is partially reflected, as explained in **section 4.2.1**. In this way, the obtained optical spectrum is the result of the reflected wave, according to the RI of fiber surroundings. The measurement of RI variations is achieved by intensity changes of the reflected optical signal. The experimental setup, used to sensor characterization, is shown in **Figure 4.10**.

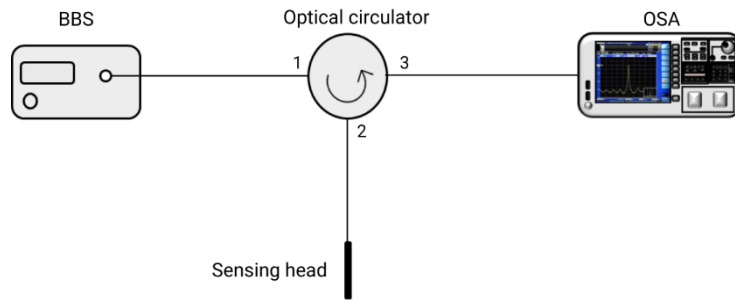


Figure 4.10. Schematic representation of the experimental setup implemented.

An 80 nm-wide BBS, centered at 1550 nm, is connected to the OSA by means of an optical circulator. The optical circulator directs the light clockwise and it is composed of three ports: the signal of BBS enters through port 1 and it is directed to the sensing head (signal comes out to port 2). The reflected signal re-enters port 2 and it is sent to port 3 (OSA). To test the sensitivity and

the resolution of the developed sensor to RI variations, it was used paracetamol liquid samples with different concentrations.

- **Paracetamol samples**

A series of samples consisting of different mass fractions of paracetamol dissolved in a solution of ethanol/deionized water (40% v/v) were previously prepared under a controlled laboratory environment at room temperature, $\sim 23^{\circ}\text{C}$. A magnetic stirrer was used to prepare the samples with a concentration range of ~ 50 to 260 g of paracetamol per kg of solvent.

The RI calibration of the samples prepared was then performed using an Abbe refractometer.

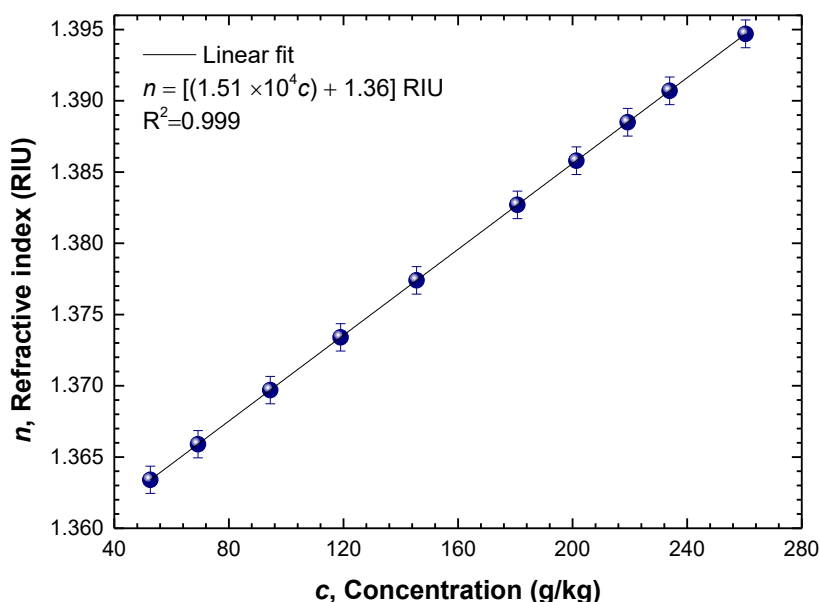


Figure 4.11. Characterization of paracetamol samples.

As is possible to see in **Figure 4.11**, it was found that a RI variation from 1.3634 to 1.3947 RIU. Also, a linear relation was obtained between the paracetamol concentration and the measured RI. As expected, this result indicates that with the increase of paracetamol concentration, the samples become optically denser and, consequently, their RI increases.

- **Sensor sensitivity**

After the RI characterization of paracetamol samples, the sensitivity of the sensor was determined. Each paracetamol sample was measured using the experimental setup shown in **Figure 4.10**.

The sensing head was vertically immersed in each paracetamol sample and the normalized spectral response was recorded using the OSA – **Figure 4.12 (a)**. Through the spectral response it was possible to determine the sensor optical power dependence to RI and paracetamol concentration variations – **Figure 4.12 (b) and (c)**.

It is important to refer to that the samples were measured by order, from the sample with the lowest concentration to the sample with the highest concentration. Also, after each sample measurement, the sensing head was cleaned with ethanol, to avoid possible contamination.

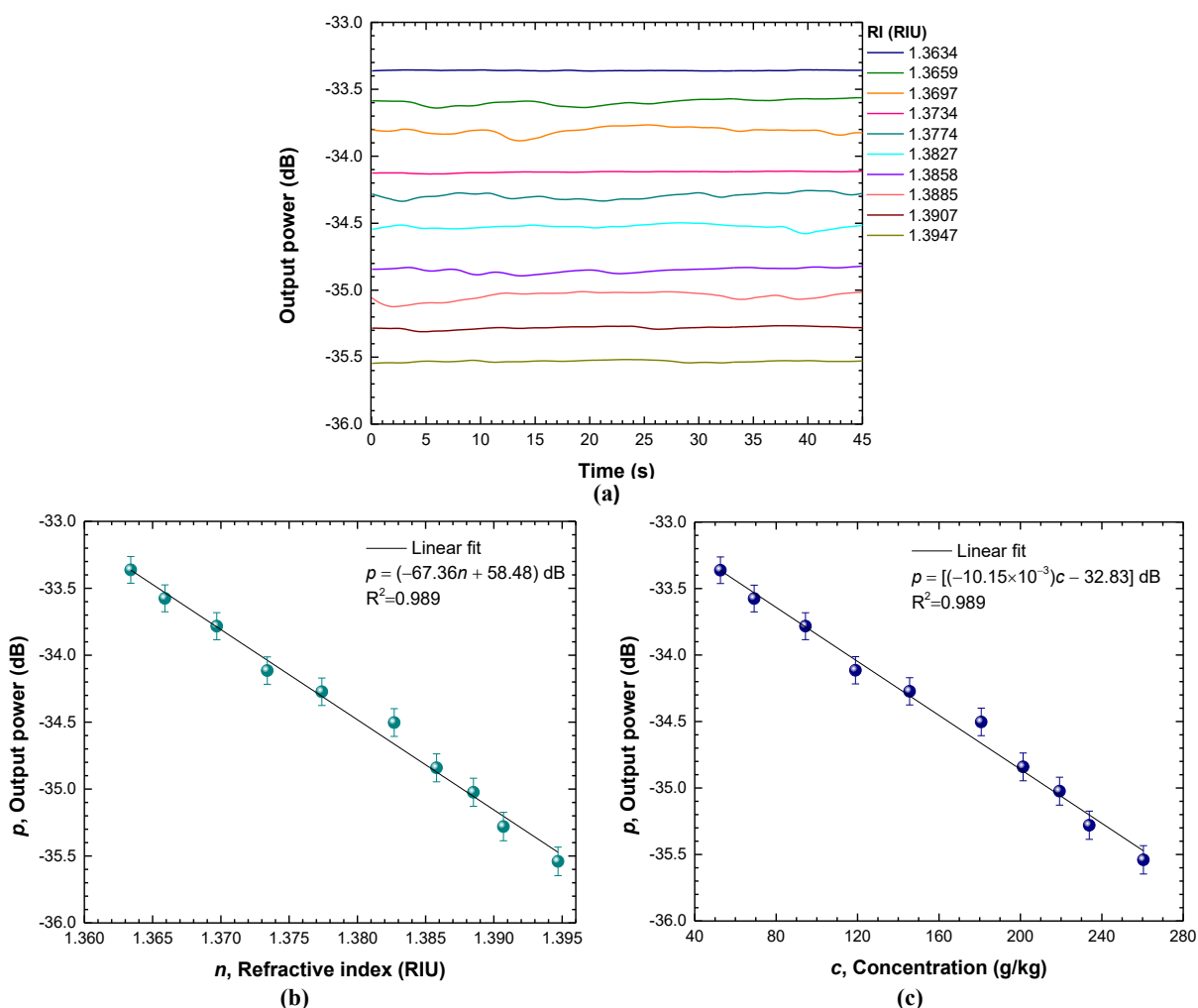


Figure 4.12. Optical power dependence on paracetamol concentration and respective refractive index. **(a)** Output spectrum for each paracetamol sample measured; **(b)** Sensor sensitivity to paracetamol refractive index variations; **(c)** Sensor sensitivity to paracetamol concentration variations.

From the results presented in **Figure 4.12 (b)**, a linear sensitivity to paracetamol RI of (-67.36 ± 2.35) dB/RIU was achieved, within the ranges of 1.3634 to 1.3947 RIU, which corresponds to a paracetamol concentration sensitivity of (-10.15 ± 0.35) dB/(g/g), within ranges from ~ 50 to 260 g/kg, – **Figure 4.12 (c)**.

- **Sensor resolution**

The resolution of the sensor was determined using the experimental setup presented in **Figure 4.10** for the sensitivity evaluation. The sensing head was vertically immersed in two samples of paracetamol with consecutive values of RI. The sensor output power response obtained during the measurements is shown in **Figure 4.13**.

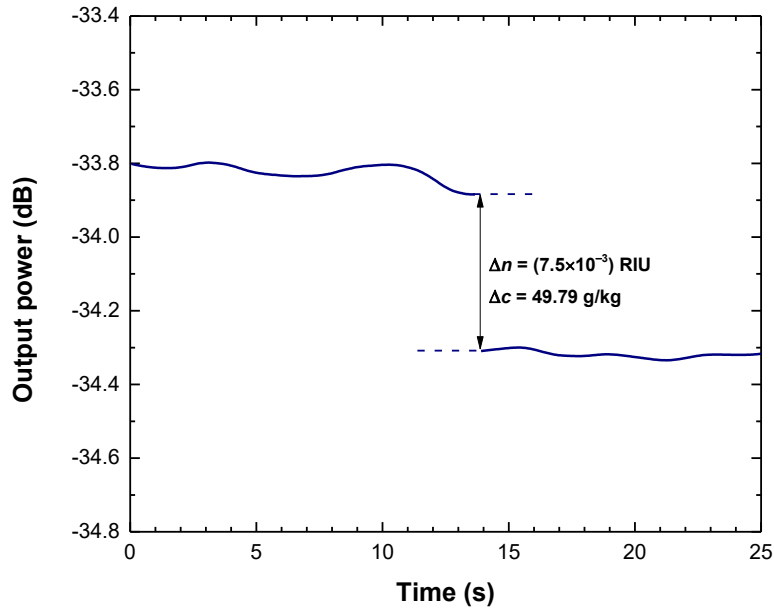


Figure 4.13. Determination of sensor resolution.

The minimum value of RI (δ_c) that the sensor could discriminate, i.e., the sensor resolution, was defined through the sensor response (**Figure 4.13**) and **Equation 4.2** [47]:

$$\delta_c = 2[(\sigma_p \Delta n) / \Delta P] \quad (4.2)$$

where σ_p is the maximum standard deviation of the output power (1.50×10^{-2} dB) for both values of RI (1.3659 and 1.3734 RIU), Δn is the variation of RIU (step of (7.50×10^{-3}) RIU, which corresponds to a variation of paracetamol concentration, Δc , of 49.79 g/kg), and ΔP is the mean displacement of output response between the two steps (4.23×10^{-1} dB).

Applying **Equation 4.2**, a resolution of (5.32×10^{-4}) RIU was obtained, which corresponds to, in terms of concentration, a (3.53×10^{-3}) g/g. It is important to mention that this value was also influenced by the spectral resolution of the equipment used for data acquisition.

4.3.2. Monitorization of crystallization process

The monitorization of paracetamol crystallization process was performed by analyzing the optical response of the sensor, i.e., the variation of the optical signal, interrogated in reflection, was analyzed. For this purpose, the experimental setup presented in **Figure 4.10** was used again, however the sensing head was fixed to a coverslip to control the crystal formation process microscopical, as represented in **Figure 4.14**.

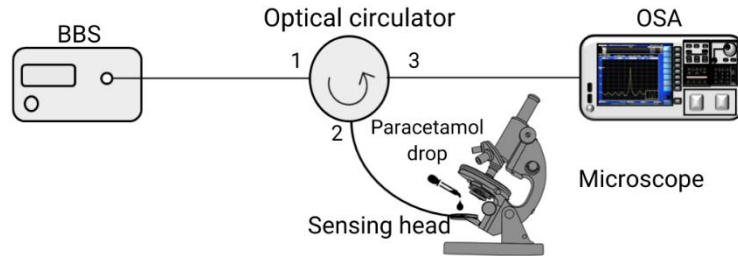


Figure 4.14. Experimental setup for the monitorization of paracetamol crystallization process.

As it is illustrated in **Figure 4.14**, the sensing head was placed horizontally on the coverslip and fixed, which provided sensor robustness, as well as the stability of the fiber.

Then, with the aid of a pipette, a drop of the previously prepared paracetamol sample (with a concentration of 200 g paracetamol/kg solvent, an ethanol/water mixture, 40% v/v) was deposited on the sensing head. In this process it was ensured that the sensing head was fully in contact with the liquid solution.

The crystallization process of paracetamol was induced by continued exposure to air, which led to the evaporation of ethanol and the consequent increase in supersaturation. All the process, since

the adding of paracetamol to the end of crystallization process, was video recorded. In **Figure 4.15** it is possible to observe the crystalline structures formed around the sensing head, acquired by video, verifying that they are essentially monoclinic polymorphs (Form I). At room temperature, this form of paracetamol crystal (Form I) is considered the more stable at room temperature conditions [48].

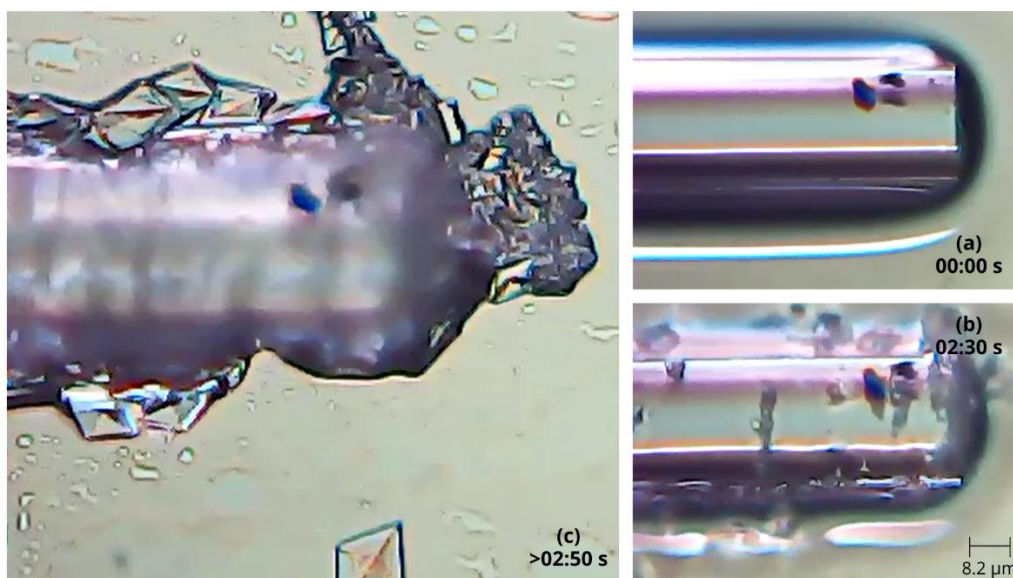


Figure 4.15. Monitorization of paracetamol crystallization process. Images acquired by video. **(a)** Drop of paracetamol in contact with the fiber tip sensor; **(b)** Beginning of paracetamol crystallization process with the continuous exposure to air; **(c)** Full evaporation of ethanol and formation of paracetamol crystalline structures.

Signal variation throughout the crystallization process, at a measuring wavelength of 1550 nm, is shown in **Figure 4.16**, where: (1) corresponds to the addition of paracetamol to the coverslip containing the sensing head, (2) to the beginning of air exposure, (3) to the beginning of the formation of crystalline structures and (4) the stabilization and termination of the crystallization process, in which the sensing head is surrounded by paracetamol crystals (see **Figure 4.15**). It is important to note that in phase (4) the crystals were still wet, which leads to slight instability by the sensor. It is also worth notice that the presence of the fiber tip sensor accelerated the crystallization process due to the capillarity effect, creating a cluster of crystals around optical fiber. Due to this, the presence of the fiber sensor enabled monitoring of the crystallization process of paracetamol.

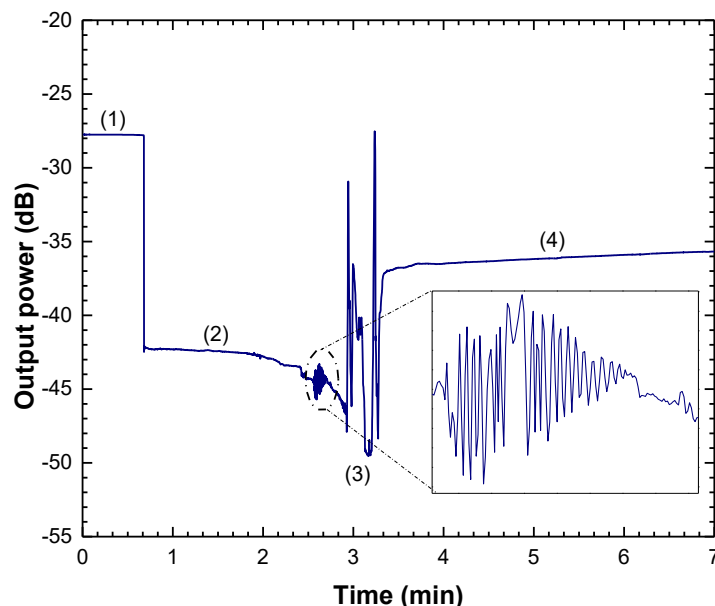


Figure 4.16. Sensor output power response during the paracetamol crystallization process: **(1)** Addition of the paracetamol drop; **(2)** Air exposure; **(3)** Initiation of crystallization process (zoom in between steps **(2)** and **(3)**); **(4)** Stabilization.

After the addition of the paracetamol sample in (1), there was a decrease in optical power, as expected, as the surroundings of the sensing head were optically denser (higher RI compared to air refraction). With continued exposure to air, in (2), the crystallization process was induced. The liquid-solid phase change occurred, presented in (3). At this phase, the sensor presented an unstable response, associated with the formation of crystalline structures around the sensing head, which interfered with light reflection at the end of the fiber tip.

At the end of the process of crystallization, in (4), the tip of the fiber sensor was surrounded by crystals, obtaining a response with some stability, as it is presented in **Figure 4.16**. Light was scattered in the presence of paracetamol crystals, where an effective index was considered, leading to an increase of the reflected signal intensity, in (4), although being lower than the intensity of the Fresnel reflection that resulted from the initial air/glass interface, in (1).

4.3.3. Concluding remarks

In this work a refractometric sensor based on a cleaved multimode fiber was developed for the monitorization of paracetamol crystallization process. The developed sensing head combines both the simplicity of its geometry and implementation. Also, the sensor reveals to have sensitivity to the refractive index variations that occur during the crystallization experiments. In this way, this sensor configuration may provide the monitorization of the crystallization process of different APIs, such as paracetamol, an asset for the pharmaceutical industry. Future developments may include this sensing head in a portable interrogation system to obtain a higher time resolution of the crystallization process. Also, the monitorization of other paracetamol polymorphs, namely, metastable form II and unstable form III, should be considered.

4.4. Final chapter remarks

Optical fiber tips sensors reveal to have an important role in different application fields.

In this chapter it is proved that a simple cleaved end of an optical fiber can be used for RI sensing, allowing the control of industrial processes, such as crystallization, or even the quality of the final products.

The sensor configurations proposed offer simplicity, reliability, and continuous capability of measurement. GI-MMF-based tip sensors allow RI measurements in a non-invasive and non-destructive way. This represents the potential to optimize production in processing industries: maximizing the use of reagents, avoiding the production of waste and, consequently, ensuring the cost reduction. On the other hand, the GI-MMF-based tip also represents an alternative to more expensive and complex analysis equipment used to monitor one of the most important processes in the pharmaceutical industry, crystallization.

To conclude, optical fiber tips sensors have great potential in the sensing field and, according to the geometry of the optical fiber, they can have sensitivity to different parameters, since its geometry controls the light distribution pattern on a specific sample, as well as the light collection efficiency.

References

- [1] Z. Y. Zhang, and K. T. Grattan, "Survey of US patent activity in optical fiber sensors". In *Optical Fiber Sensor Technology: Introduction and Overview*, Springer, Boston, MA, 2000.
- [2] R. Correia, R. Sinha, A. Norris, S. Korposh, S. Talbot, F. U. Hernandez, and S. P. Morgan, "Optical fiber sensing at the interface between tissue and medical device". In *Proceedings of the International Conference on Biophotonics V*, 103400X, Apr. 2017, Perth, Australia, DOI:10.1117/12.2269811.
- [3] S. Silvestri, and E. Schena, "Optical-Fiber Measurement Systems". In *Optoelectronics: Devices and Applications*, P. Predeep, Ed. Rijeka, Croatia: InTech, pp.205–224, 2011.
- [4] S. Silva, P. Roriz, and O. Frazão, "Refractive Index Measurements of Liquids Based on Microstructured Optical Fibers", *Photonics*, vol.1, n°4, pp.516-529, Dec. 2014, DOI:10.3390/photonics1040516.
- [5] R. Y. Shah, and Y. K. Agrawal, "Introduction to fiber optics: Sensor for biomedical applications", *Indian J. Pharm. Sci.*, vol.73, n°1, pp.17-22, Jan. 2011, DOI:10.4103/0250-474X.89752.
- [6] N. Fang, Y. Qiu, Z. Chen, Q. Chen, and Q. Lu, "Fiber-optic Nanoprobe Measurement of Intracellular pH in Single CA46 Cell Using pH-dependent Dye". In *proceedings of International Conference on BioMedical Engineering and Informatics*, vol.2, pp.619-623, Oct. 2008, Sanya, China, DOI:10.1109/BMEI.2008.190.
- [7] Y.- H. Tai, and P.- K. Wei, "Sensitive liquid refractive index sensors using tapered optical fiber tips", *Opt. Lett.*, vol.35, n°7, pp.944-946, Apr. 2010, DOI:10.1364/OL.35.000944.
- [8] B. Dong, J. Hao, T. Zhang, and J. L. Lim, "High sensitive fiber-optic liquid refractive index tip sensor based on a simple inline hollow glass micro-sphere", *Sensor Actuators B-Chemical*, vol.171, pp.405-408, May 2012, DOI:10.1016/j.snb.2012.05.001.
- [9] P. Wang, M. Ding, L. Bo, C. Guan, Y. Semenova, Q. Wu, G. Farrell, and G. Brambilla, "Fiber-tip high-temperature sensor based on multimode interference", *Opt. Lett.*, vol.38, n°22, pp.4617-4620, Nov. 2013, DOI:10.1364/OL.38.004617.

-
- [10] H. Nikbakht, H. Latifia, T. Aminib, and M. L. Zibaiia, "Tip Sensor Probe for Changing Refractive Index Measurement in Small Volumes", *Int. J. Opt. Photonics*, vol.8, n°2, pp.105-111, July 2014, Corpus ID:8020494.
- [11] M. Li, Y. Liu, S. Qu, and Y. Li, "Fiber-optic sensor tip for measuring temperature and liquid refractive index", *Optical Engineering*, vol.53, n°11, pp.116110(1)-116110(5), Nov. 2014, DOI:10.1117/1.OE.53.11.116110
- [12] Y. Liu, X. Liu, T. Zhang, and W. Zhang, "Integrated FPI-FBG composite all-fiber sensor for simultaneous measurement of liquid refractive index and temperature", *Optics and Lasers in Engineering*, vol.111, pp.167-171, Dec. 2018, DOI:10.1016/j.optlaseng.2018.08.007.
- [13] S. Novais, C. I. A. Ferreira, M. S. Ferreira, and J. L. Pinto, "Optical Fiber Tip Sensor for the Measurement of Glucose Aqueous Solutions", *IEEE Photonics Journal*, vol.10, n°5, pp.1-9, Oct. 2018, DOI:10.1109/JPHOT.2018.2869944.
- [14] A. D. Gomes, J. Kobelke, J. Bierlich, K. Schuster, H. Bartelt, and O. Frazão, "Optical Fiber Probe Viscometer Based on Hollow Capillary Tube", *J. Lightwave Technol.*, vol.37, n°18, pp.4456-4461, Sept. 2019, DOI:10.1109/JLT.2019.2890953.
- [15] Z. Zhang, B. Xu, M. Zhou, W. Bao, X. Xu, Y. Wang, J. He, Y. Wang, "Hollow-Core Fiber-Tip Interferometric High-Temperature Sensor Operating at 1100°C with High Linearity", *Micromachines*, vol.12, n°3, 234, Feb. 2021, DOI:10.3390/mi12030234.
- [16] P. N. S. S. Ja'afar, N. M. Razali, S. Ambran, and F. Ahmad, "Sodium Chloride Concentration Measurement via Optical Fiber Tip Sensor", *IOP Conf. Series: Materials Science and Engineering*, vol.1051, n°1, 012030, Feb. 2021, DOI:10.1088/1757-899X/1051/1/012030.
- [17] C. Lu, H. Nikbakht, M. Y. Erdolu, B. van Someren, and B. I. Akca, "Tapered tip optical fibers for measuring ultra-small refractive index changes with record high sensitivity", *Optics Letters*, vol.47, n°23, pp.6281-6284, Dec. 2022, DOI:10.1364/OL.477288.
- [18] C. Chen, W. Wang, Z. Liu, X. Zeng, K. Wang, and B. Zhang, "Optical fiber probe with a concave cavity for non-contact trapping", *Optics & Laser Technology*, vol.166, 109647, June 2023, DOI:10.1016/j.optlastec.2023.109647.
- [19] M. Gu, S. Yuan, Q. Yuan, and Z. Tong, "Temperature-independent refractive index sensor based on fiber Bragg grating and spherical-shape structure", *Opt. Lasers Eng.*, vol.115, n°1, pp.86-89, Nov. 2019, DOI:10.1016/j.optlaseng.2018.11.018.

-
- [20] J. Li, “A review: Development of novel fiber-optic platforms for bulk and surface refractive index sensing applications”, *Sensors and Actuators Report*, vol.2, n°1, 100018, 2020, DOI:10.1016/j.snr.2020.100018.
- [21] A. Bušić, N. Marđetko, S. Kundas, G. Morzak, H. Belskaya, M. I. Šantek, D. Komes, S. Novak, B. Šantek, “Bioethanol Production from Renewable Raw Materials and its Separation and Purification: A Review”, *Food Technol Biotechnol.*, vol.56, n°3, pp.289-311, July-Sept. 2018, DOI:10.17113/ftb.56.03.18.5546.
- [22] S. F. Memon, R. Wang, B. Strunz, B. S. Chowdhry, J. T. Pembroke, E. Lewis, “A Review of Optical Fibre Ethanol Sensors: Current State and Future Prospects”, *Sensors*, vol.22, n°3, 950, Jan. 2022, DOI:10.3390/s22030950.
- [23] J. Qiao, H. Cui, M. Wang, X. Fu, X. Wang, X. Li, H. Huang, “Integrated biorefinery approaches for the industrialization of cellulosic ethanol fuel”, *Bioresource Technology*, vol.360, 127516, Sept. 2022, DOI:10.1016/j.biortech.2022.127516.
- [24] F. K. Coradin, G. R. C. Possetti, R. C. Kamikawachi, M. Muller, J. L. Fabris, “Etched Fiber Bragg Gratings Sensors for Water-Ethanol Mixtures: A Comparative Study”, *J. Microw. Optoelectron. Electromagn. Appl.*, vol.9, n°2, pp.131-143, Dec. 2010, DOI:10.1590/S2179-10742010000200007.
- [25] N. Nishi, S. Takahashi, M. Matsumoto, A. Tanaka, K. Muraya, “Hydrogen bonding cluster formation and hydrophobic solute association in aqueous solution of ethanol”, *Journal of Physical Chemistry*, vol.99, n°1, pp.462-468, Jan. 1995, DOI:10.1021/j100001a068.
- [26] R. C. Kamikawachi, I. Abe, A. S. Paterno, H. J. Kalinowski, M. Muller, J. L. Pinto, J. L. Fabris, “Determination of thermo-optic coefficient in liquids with fiber Bragg grating refractometer”, *Opt. Commun.*, vol.281, n°4, pp.621-625, Feb. 2008, DOI:10.1016/j.optcom.2007.10.023.
- [27] G. R. C. Possetti, L. C. Côcco, C. I. Yamamoto, L. V. R. Arruda, R. Falate, M. Muller, J. L. Fabris, “Application of a long-period fibre grating-based transducer in the fuel industry”, *Meas. Sci. Technol.*, vol.20, n°3, pp.034012V-1–034012V-9, Feb. 2009, DOI:10.1088/0957-0233/20/3/034012.
- [28] Y. H. Kim, S. J. Park, S. -W. Jeon, S. Ju, C. -S. Park, W. -T. Han, and B. H. Lee, “Thermo-optic coefficient measurement of liquids based on simultaneous temperature and refractive

-
- index sensing capability of a two-mode fiber interferometric”, *Opt. Express*, vol.20, n°21, pp.23744–23754, Oct. 2012, DOI:10.1364/OE.20.023744.
- [29] C. -L. Lee, H. -Y. Ho, J. -H. Gu, T. -Y. Yeh, and C. -H. Tseng, “Dual hollow core fiber-based Fabry-Perot interferometer for measuring the thermo-optic coefficients of liquids”, *Opt. Lett.*, vol.40, n°4, pp.459-462, Feb. 2015, DOI:10.1364/OL.40.000459.
- [30] J. Ge, X. Cheng, C. Zhao, K. Gui, W. Zhang, F. A. Cheikh, and L. Ye, “Reflected light intensity-modulated continuous liquid level sensor based on oblique end face coupling optical fibers”, *IEEE Sens. J.*, vol.20, n°8, pp.4229-4236, Apr. 2020, DOI:10.1109/JSEN.2019.2962610.
- [31] T. Ma, A. Markov, L. Wang, and M. Skorobogatiy, “Graded index porous optical fibers – dispersion management in terahertz range”, *Optics Express*, vol.23, n°6, pp.7856-7869, Mar. 2015, DOI:10.1364/OE.23.007856.
- [32] L. Soares, R. A. Perez-Herrera, S. Novais, A. Ferreira, O. Frazão, and S. Silva, “Measurement of paracetamol concentration using an erbium-doped fiber ring Cavity” *Photonics*, vol.10, n°1, 50, Jan. 2023, DOI:10.3390/photonics10010050.
- [33] E. Hecht, *Optics*, 5th ed., Pearson: London, UK, 2015.
- [34] Thorlabs, “Graded-Index (GRIN) Multimode Fibers”.
https://www.thorlabs.com/newgrouppage9.cfm?objectgroup_id=358&pn=GIF625#11368
(accessed July 28, 2024).
- [35] A. M. Schwartz, and A. S. Myerson, “Solutions and solution properties”. In *Handbook of Industrial Crystallization*, 2nd ed., Butterworth-Heinemann: Oxford, 2002.
- [36] N. Saleemi, *Strategic feedback control of pharmaceutical crystallization systems*, Loughborough University, UK, 2011.
- [37] J. Chen, B. Sarma, J. B. Evans, and A. Myerson, “Pharmaceutical Crystallization”, *Cryst. Growth Des.*, vol.11, n°4, pp.887-895, Feb. 2011, DOI:10.1021/cg101556s.
- [38] J. M. Coulson, and J. F. Richardson, “Crystallisation”. In *Chemical Engineering*, 5th ed. Butterworth-Heinemann: Oxford, 2013.
- [39] P. Di Martino, P. Conflant, M. Drache, J. P. Huvenne, and A. M. Hermann, “Preparation and physical characterization of form II and III of paracetamol”, *J. Therm. Anal.*, vol.48, pp.447–458, Mar. 1997, DOI:10.1007/BF01979491.

-
- [40] C. Sudha, and K. Srinivasan, “Supersaturation dependent nucleation control and separation of mono, ortho and unstable polymorphs of paracetamol by swift cooling crystallization technique”, *CrystEngComm.*, vol.15, n°10, pp.1914–1921, Dec. 2013, DOI:10.1039/C2CE26681D.
- [41] Z. K. Nagy, G. Fevotte, H. Kramer, and L. L. Simon, “Recent advances in the monitoring, modeling and control of crystallization systems”, *Chem. Eng. Res. Des.*, vol.91, n°10, pp.1903–1922, Oct. 2013, DOI:10.1016/j.cherd.2013.07.018.
- [42] C. J. Brown, T. McGlone, S. Yerdelen, V. Srirambhatla, F. Mabbott, R. Gurung, M. L. Briuglia, B. Ahmed, H. Polyzois, and J. McGinty, “Enabling precision manufacturing of active pharmaceutical ingredients: workflow for seeded cooling continuous crystallizations”. *Mol. Syst. Des. Eng.*, vol.2018, n°3, pp.518–549, Jun. 2018, DOI:10.1039/C7ME00096K.
- [43] J. B. Nanubolu, and J. C. Burley, “Investigating the recrystallization behavior of amorphous paracetamol by variable temperature Raman studies and surface Raman mapping”, *Mol. Pharm.*, vol.9, n°6, pp.1544–1558, Apr. 2012, DOI:10.1021/mp300035g.
- [44] M. Birch, S. Fussell, P. Higginson, N. McDowall, and I. Marziano, “Towards a PAT-Based Strategy for Crystallization Development”, *Org. Process Res. Dev.*, vol.9, n°3 pp.360-364, Apr. 2005, DOI:10.1021/op0500077.
- [45] L. Simon, et al., “Assessment of Recent Process Analytical Technology (PAT) Trends: A Multiauthor Review”, *Org. Process Res. Dev.*, vol.19, n°1, pp.3-62, Jan. 2015. DOI:10.1021/op500261y.
- [46] L. X. Yu, R. A. Lionberger, A. S. Raw, R. D’Costa, H. Wu, and A. S. Hussain, “Applications of process analytical technology to crystallization processes”, *Adv. Drug Deliv. Rev.*, vol.56, n°3, pp.349-369, Feb. 2004, DOI:10.1016/j.addr.2003.10.012.
- [47] S. Novais, M. S. Ferreira, and J. L. Pinto, “Relative humidity fiber sensor based on multi-mode interferometer coated with agarose-gel”, *Coatings*, vol.8, n°12, 453, Dec. 2018, DOI:10.3390/coatings8120453.
- [48] J. R. Méndez del Rio, and R. W. Rousseau, “Batch and tubular-batch crystallization of paracetamol: crystal size distribution and polymorph formation”, *Cryst. Growth Des.*, vol.6, n°6, pp.1407–1414, May 2006, DOI:10.1021/cg060025v.

Chapter 5. Erbium-doped fiber lasers for refractive index sensing

5.1. Introduction

Laser technology was discovered in 1960 by T. H. Maiman and after that the optical fiber sensors were introduced and developed for several sensing applications [1, 2].

In 1961 Eli Snitzer demonstrated the possibility of using rare earth-doped optical fibers as gain medium in fiber lasers and fiber amplifiers [3]. The development of Erbium-Doped Fiber Amplifiers (EDFA), in the 1990s, marked a milestone in this type of sensing technology and after that the lasers were subjected to an intensified investigation [4].

5.1.1. Laser

Laser corresponds to the *Light Amplification by Stimulated Emission of Radiation*, i.e., the physical basis of laser is the amplification of incoming radiation [5].

The principle of stimulated emission of radiation was first described in 1916 by Albert Einstein. According to it, photons can propagate through a certain medium/gain medium (previously excited) and interact with the medium material. This interaction causes the production of more photons, identical to the incident photons – stimulated emission [5, 6].

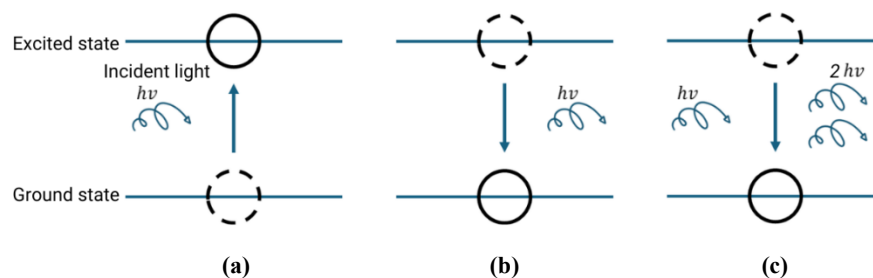


Figure 5.1. Schematic representation of absorption and emission, created by radiation-medium interaction, between two levels of energy. (a) Absorption; (b) Spontaneous emission; (c) Stimulated emission.

The circle represents the state of the atom before and after transition. The arrow represents the photons with energy given by $E = h\nu$, where h corresponds to the Planck's constant and ν to the frequency of radiation. Adapted from [8].

The incident photons can stimulate atoms (or ions of a certain gain medium) that store and release light energy. Atoms or ions have two main energy states: the ground state and the excited state. The ground state is the most stable and corresponds to the state with lowest energy. When the incident photons propagate through a medium, the atoms/ions in the ground state are excited and more of them passes to a higher energy level – occurs light absorption, **Figure 5.1 (a)**. When the atoms/ions at excited levels of energy back into a lower energy level, a photon is released. This is called light emission either spontaneous or by stimulated processes (**Figure 5.1 b** and **c**, respectively). When the atom/ion returns to a lower energy level randomly, a spontaneous light emission occurs. On the other hand, when a photon interacts with an atom/ion, at a specific energy level, causing it to return to a lower energy level, creating more photons, it is called stimulated emission. However, the energy of the first photon must be equal to the energy difference between the highest and the lowest energy level, related to the referred atom/ion transition. Besides its energy, the photons emitted by stimulated emission have also a definite time and phase relation to each other, creating a monochromatic output light with a high degree of coherence [7-8].

This stimulated emission creates the amplification of the initial spontaneous emission, originating a phenomenon called Amplified Spontaneous Emission (ASE).

To have amplification of light in the gain medium, it is necessary to have a population of atoms at an upper energy level greater than at a lower energy level. This causes a non-equilibrium distribution, called population inversion (**Figure 5.2**).

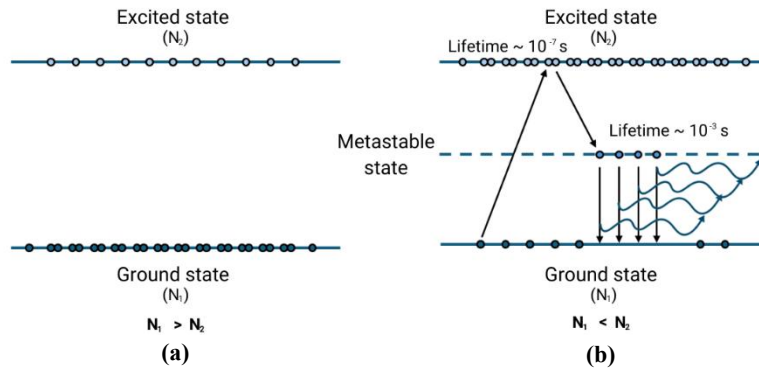


Figure 5.2. Schematic of population inversion and amplification of light. **(a)** Absorption without population inversion; **(b)** Population inversion and amplification of light in a three-level laser system. Adapted from [9].

As is possible to see in **Figure 5.2 (a)**, when the pumping of a gain medium is not enough, population inversion does not occur. In this case, the number of atoms in the lower energy state (N_1) is higher than that of the upper energy state (N_2): $N_1 > N_2$; the absorption of the light

overcomes the amplification of light. In this regime, light is absorbed rather than amplified, since stimulated emission cannot outpace absorption. On the other hand, when pumping is strong enough to achieve population inversion, i.e., $N_1 < N_2$, net optical gain becomes positive. In this case, stimulated emission is dominant, enabling amplification of light (**Figure 5.2 b**). Even in the absence of an optical cavity, Amplified Spontaneous Emission (ASE) can occur, i.e., spontaneously emitted photons are amplified as they pass through the gain medium. In systems with a cavity, ASE may still be present — especially below the lasing threshold — but once the threshold is reached, stimulated emission is reinforced by the feedback mechanism, leading to coherent laser emission [8, 9].

As is represented in **Figure 5.3 (a)**, when a laser is pumped and the pumping increases and reaches a certain threshold, it leads to population inversion. At this point, stimulated emission is the most dominant and the intensity increases – **Figure 5.3 (b)**, i.e., the “lasing” effect starts to appear, and the emission of identical photons causes the narrowing of the spectrum [8, 10].

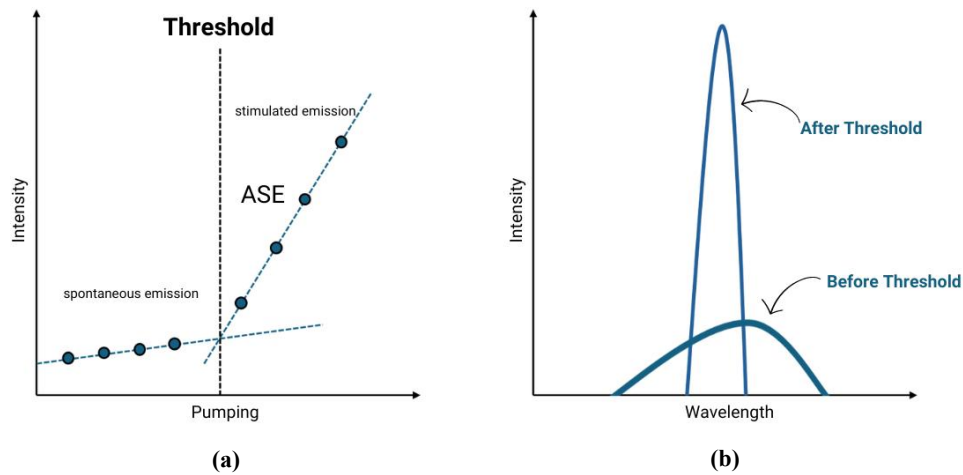


Figure 5.3. Lasing threshold. **(a)** Intensity of the spectra as a function of pumping rate; **(b)** Emission spectra before and after threshold. Adapted from [10].

As previously reported, the medium where the laser phenomenon occurs is called gain medium and it can take different forms, such as the rare earth-doped optical fibers. Regardless of the type of gain medium, they are always composed of the host (e.g. silica optical fibers) into which the active elements are introduced (e.g. erbium).

The host material is not responsible for light amplification, however it is responsible for the definition of some properties of the gain medium, such as the selection of the most suitable pumping. The pumping can be performed by optical radiation, chemical reactions, electrical discharge, or by the passage of an electrical current through the gain medium.

There are also two other important elements in a laser configuration: the laser cavity and the output coupler (**Figure 5.4**).

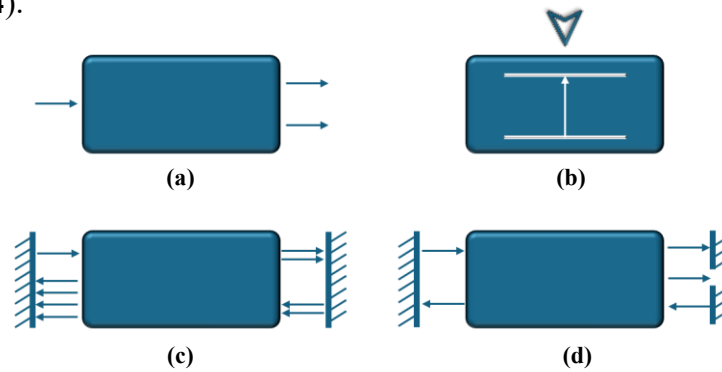


Figure 5.4. Schematic representation (simplified) of fiber laser elements. (a) Gain medium; (b) Pumping; (c) Laser cavity; (d) Output coupler. Adapted from [13].

The laser cavity is responsible for redirecting the emitted radiation back to the gain medium, increasing the amplification phenomenon. For that, optical reflectors are used. On the other hand, the output coupler allows the extraction of part of radiation from the laser cavity to the outside. It is important to notice that the amplification phenomenon is limited. It happens until the saturation state, which depends on the pumping and the doped element used [2, 6, 11-13].

5.1.2. Optical fiber lasers

A fiber amplifier can be converted into a laser, if it is placed inside a cavity that provides optical feedback. This type of laser is called fiber laser [11].

Fiber lasers are a type of solid-state lasers, which means that the gain medium is an optical fiber with a core doped with a rare-earth element, such as erbium. **Figure 5.5** shows a basic example of fiber laser configuration. As it is possible to see, the fiber cavity is composed of a segment of optical fiber with a core doped with rare-earth element and reflecting mirrors [2, 13].

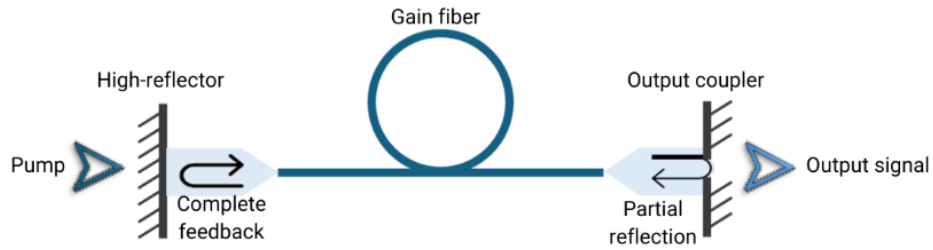


Figure 5.5. Schematic representation of a fiber laser and its principal elements. Adapted from [13].

The fiber cavities are very versatile and compact, despite their length. They are usually classified into two categories: the linear and the ring cavities [11]. The linear cavity is formed by two reflector elements at each side of the cavity. On the other hand, the ring cavity does not need reflector elements, because it is closed on itself (**Figure 5.6**).

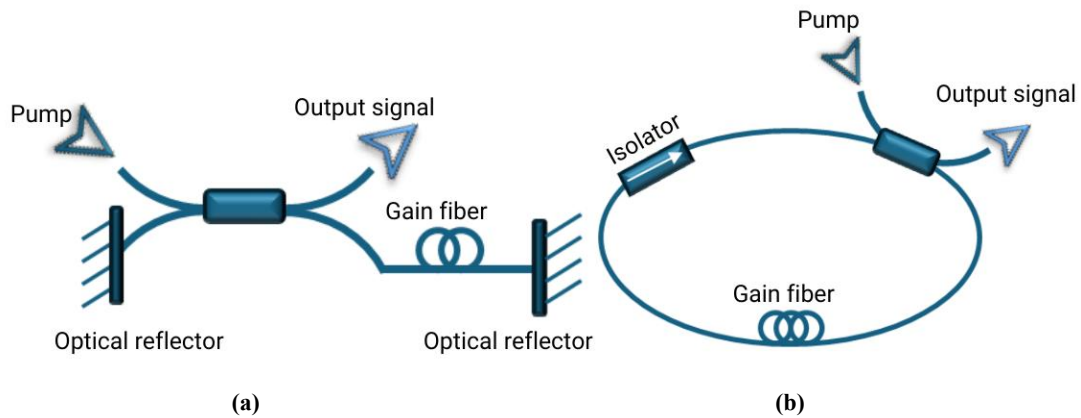


Figure 5.6. Schematic representation of: (a) Linear cavity; (b) Ring cavity. Adapted from [11, 13].

In a ring cavity it is important to use an optical isolator to ensure unidirectional operation and to avoid the Spatial Hole Burning (SHB) effect, which is characterized by the gain saturation, periodically, through the gain medium [11]. In a non-unidirectional operation, several light beams pass through a laser medium with inhomogeneous absorption. In this way, some areas of the gain medium experience a loss in gain, resulting in holes in the output signal. Some works have shown that optical isolators, in this type of configuration, can be replaced by optical circulators [14]. Regarding the linear cavity, as previously referred, it is formed by two optical reflectors, such as Fiber Bragg Gratings (FBGs) or fiber loop mirrors. One of the reflectors, ideally, has 100% of reflectivity, to maximize the signal feedback to the cavity, and the other one is a partial reflector

or an output coupler, because it allows to extract the signal out of the cavity, as well as provide the signal feedback to the cavity (see **Figure 5.5**). In this way, the signal repeatedly goes forward and back in the cavity, between the two reflectors and the stimulated emission from the gain medium is then allowed to amplify the signal. In relation to the laser pumping (**Figure 5.5**), it can be made through fiber optic-based components, such as the Wavelength Division Multiplexers (WDM). In these cases, the laser becomes extremely compact with excellent stability over time, because the configuration does not need other non-fiber-based components or additional alignments [11, 14].

5.1.3. Erbium-doped fiber lasers applications

In the 1990s fiber lasers became a very promisor technology in the telecommunications field. In this way, several amplifiers were developed and applied to fiber optic technology [2, 4].

The Erbium-Doped Fiber Amplifier (EDFA) is widely valued for its high efficiency, stability, resolution, and sensitivity, as well as its favorable Optical Signal-to-Noise Ratio (OSNR). It can provide gains of up to 40 dB and exhibits low gain dependence on light polarization, ensuring stable and high-quality optical signals [8, 11]. Together with the well-known characteristics of optical fiber sensors, namely, reduced dimensions, low weight, flexibility, low losses, no electromagnetic interference, multiplexing capacity, and remote monitoring at specific spatial points (as a probe) or even in large areas (through multiple detection regions along the optical fiber), fiber laser sensors became to be considered a technology with great potential for many optical sensing applications [15].

The erbium-doped fiber lasers (EDFLs) are the most well-known laser configuration because the erbium element allows signal amplification exactly in the region where the losses of an optical fiber are lowest. This is one of the reasons why the EDFA is the most used device in several applications, specifically, in the telecommunications networks field [2, 6, 7, 11].

EDFL configurations can be conceived and constructed in a linear or in a ring configuration. However, it was found that linear cavity lasers, compared with ring configurations, easily reach the saturation state, and have also low threshold pump power, high slope efficiency, high laser power and a high OSNR [14].

In the early 2000s, due to the collapse of telecommunications markets, fiber laser technology started to be applied in several areas, such as industrial material processing, and military, scientific

and medical fields, that require easily manufacturable systems, with a range of power levels and output quality [2, 7, 8].

EDFLs can be also used for measurements of several process parameters: temperature [16], strain [17], magnetic field [18], pressure [19], concentration [20], and RI [21].

Studies revealed that this technological approach has great potential for process parameters measurements with high resolution and accuracy in the sensing field [11, 16]. EDFLs correspond to a simple and robust technology, that can be used to perform in-line measurements in several processing industries to contribute to the quality control of their final products [16-21].

This chapter presents different configurations of EDFLs based on ring and linear configurations for RI sensing.

5.2. Erbium-doped fiber ring cavity configuration

An Erbium-Doped Fiber Ring Cavity (EDFRC) for measurements of RI in liquid solutions was implemented, as shown in **Figure 5.7**.

During all the experiments, the fiber handling was performed using the same material. The splicing was achieved using a splicer machine (TYPE-72C, Sumitomo Electric) and before every slicing process, the coating from the fibers was removed by cutting pliers and the fibers were cleaned with acetone or ethanol. Then, the fibers were cleaved by a cleaver machine (FC-6RS, Sumitomo Electric) to be prepared for splicing. The use of cleavers guaranteed the perpendicularity of the cleaved surface in relation to the fiber axis.

A 980/1550 nm WDM was responsible for injecting pump power into the EDFRC (976 nm), and the laser diode was temperature-controlled to ensure the stability of the laser output. The gain medium used consisted of 4 m of highly Erbium-Doped Fiber (EDF) with an active absorption coefficient of 5.0–6.7dB/m @1531 nm. The EDF was connected to the common port of the WDM and to a 3-port optical circulator, which, in turn, was connected to a 1×3 optical coupler by means of port 2. Port 1 of the optical coupler was connected to a commercial FBG; port 2 was used as a reference and port 3 was used as a sensing head.

An 8 mm-length commercial FBG was used, centered at 1543.65 nm, with a reflectivity of 97.59% and a bandwidth of 0.243 nm at -3 dB. In this configuration, the FBG acts solely as a highly reflective mirror of the laser cavity.

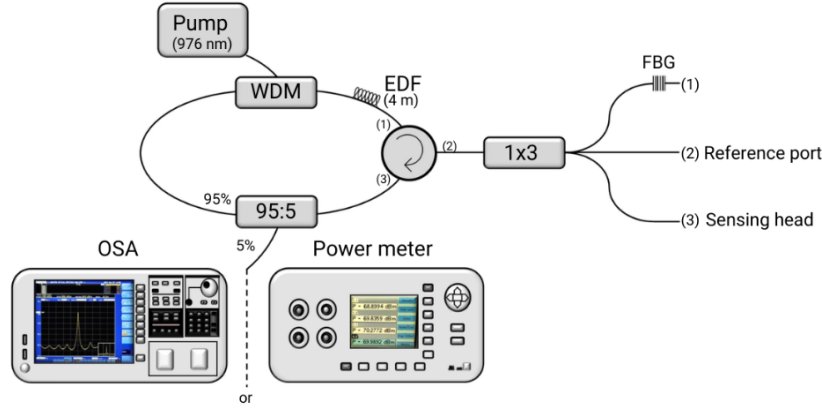


Figure 5.7. Experimental setup of the erbium-doped fiber ring cavity used for refractive-index measurements.

A 95:5 optical coupler was used to extract 5% of the signal from the ring to an OSA or to a power meter. It is important to note that the use of circulators ensured the unidirectional operation and avoided the SHB.

The fiber tips of the three output ports of the optical coupler were properly cleaved to ensure the Fresnel reflection. In the case of the fiber tip where the FBG was located, it was cleaved 20 mm after the FBG.

5.2.1. Sensing head structure and operating mechanism

The sensing head structure of this experiment corresponded to a SMF-based tip (SMF 28e, core and cladding diameters of 8.2 μm and 125 μm , respectively), that worked as a refractometric sensor, modulated in intensity, as it is shown in **Figure 5.8**.

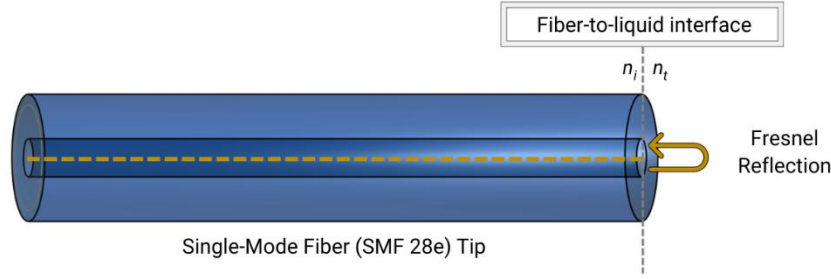


Figure 5.8. Schematic of the sensing head and its operating mechanism.

The physical principle related to its operating mechanism relies on measurand-induced intensity variation of the Fresnel reflection at the fiber-to-liquid interface monitored, as explained in **section 4.2.1 of Chapter 4** [22]. Upon reaching the surroundings, the light is partially reflected, as is illustrated in **Figure 5.8**. In this way, the measurement of RI variations is achieved with the intensity changes of the reflected optical signal.

5.2.2. Output spectrum

The output spectrum of the EDFRC was acquired using the OSA (YOKOGAWA, model AQ6370D), when the system was pumped with 20 nW at 976 nm, and the reference (port 2 of optical coupler) and the sensing head (port 3 of optical coupler) were only in contact with air – **Figure 5.9**.

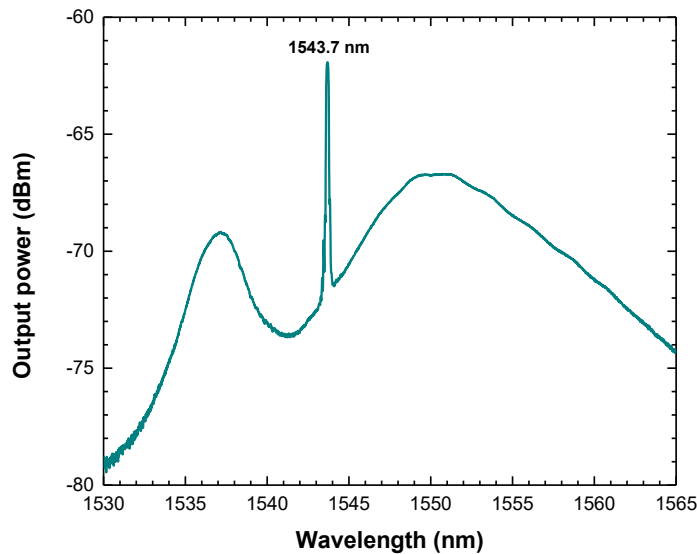


Figure 5.9. EDFRC output spectrum pumped by a 976-nm laser at 20 mW, when both output port 2 (reference port) and output port 3 (sensing head) were in air.

As is possible to see in **Figure 5.9**, the laser condition was not reached, due to the small amount of pump power. An output peak power of ~ -62 dBm was obtained, centered at 1543.7 nm, measured with an OSNR as low as 10 dB.

5.2.3. Fiber ring cavity characterization

Initially, an RI characterization was performed. Two of the three coupler output ports were vertically immersed in air, water, or alcohol (**Figure 5.10**). In each of these situations, the system output power response was acquired using the power meter (model Agilent 8163B).

The losses produced, as shown in **Figure 5.10**, were also evaluated in these situations:

(a) both, the reference and the sensing head, were in air, (b) the reference was immersed in water and the sensing head remained in air, (c) both were in water, (d) the reference was in alcohol and the sensing head in water, and (e) both, sensing head and reference, were immersed in alcohol. In addition, this analysis was also performed with (**Figure 5.10**, black line) and without (**Figure 5.10**, blue line) the FBG connected to the output port 1 of the optical coupler (**Figure 5.7**).

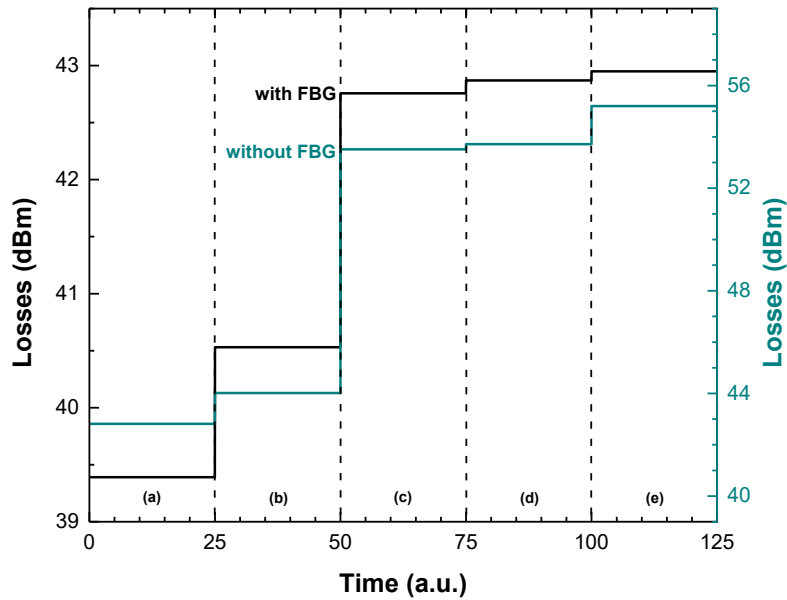


Figure 5.10. Sensor characterization with (black line) and without (blue line) FBG when: **(a)** both the reference and the sensing head were in air; **(b)** the reference was immersed in water and the sensor remained in air; **(c)** both were deep in water; **(d)** the reference port and the sensing head were immersed in alcohol and water, in that order; **(e)** both ports were immersed in alcohol.

As is possible to see in **Figure 5.10**, the variations in induced losses are lower when the FBG reflector is used, improving the characteristics of the interrogation system. When the FBG is used (black line), the losses introduced into the fiber ring cavity ranged from 39.4 dB to 42.95 dB in cases (a) and (e), respectively. However, these losses increase to 42.8 dB or 55.2 dB in cases (a) and (e), when the FBG is not connected to the fiber ring cavity (blue line). These experimental results demonstrate the importance of including the FBG as a reflector in the fiber ring cavity configuration.

5.2.4. Sensing applications

The EDFRC system capability to perform optical concentration measurements in liquid solutions was analyzed and experimentally demonstrated. For this purpose, eight standard liquid solutions of paracetamol (CAS number 103-90-02, min. 99% purity, supplied by Sigma-Aldrich) in a mixture of 40% (v/v) ethanol/deionized water were used.

- **Paracetamol liquid samples characterization**

The samples were prepared at room temperature ($\sim 20^\circ\text{C}$) and their concentration ranged from 52.61 to 219.25 g paracetamol/kg solvent, which corresponded to a RI range of 1.3637 to 1.3899 RIU. To determine the RI of said solutions, an Abbe refractometer (ATAGO, DR-A1) was used to measure the samples. As expected, **Figure 5.11** shows that, with the increase of paracetamol in solution, the samples become optically denser and, consequently, the RI linearly increased.

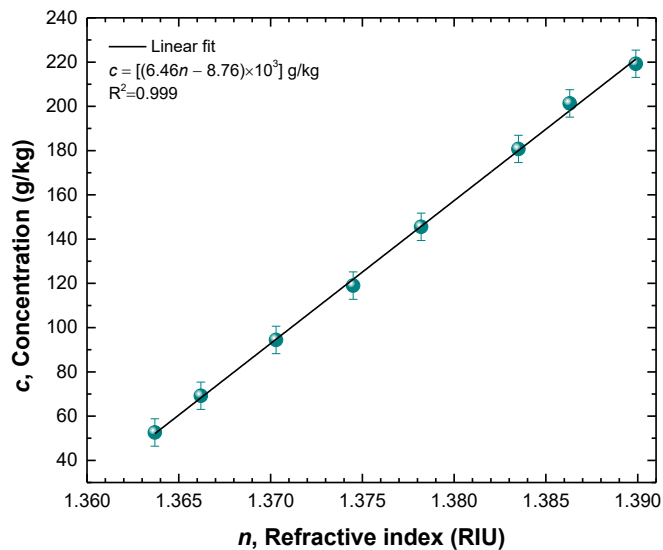


Figure 5.11. Concentration of paracetamol in solution as a function of refractive index.

In the first step, it was performed a RI characterization of the solvent used in the paracetamol standard solutions: a mixture of 40% ethanol and 60% deionized water. For this, mixtures of ethanol and deionized water with different percentages in volume were prepared. The samples were measured using the Abbe refractometer and it was obtained a RI range of 1.337 RIU to, approximately, 1.357 RIU. Using the EDFRC setup (recall **Figure 5.7**), the samples were also measured, and the output power response was acquired using the power meter.

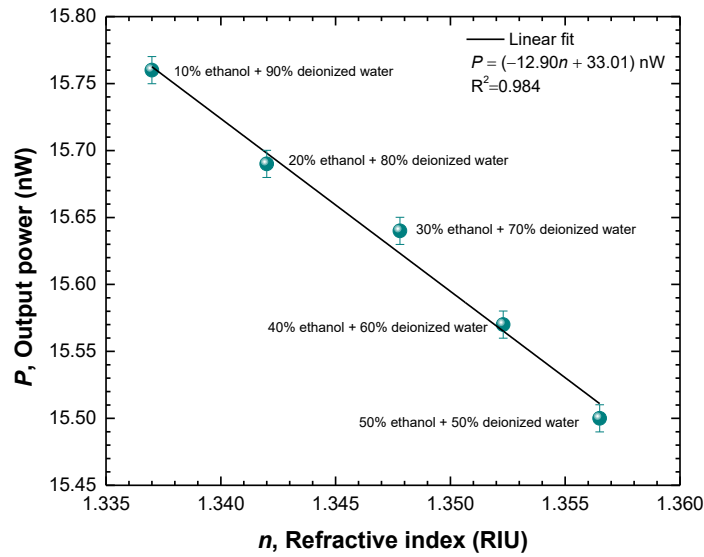


Figure 5.12. Refractive index characterization of ethanol and deionized water mixtures.

For the mixture of interest, i.e., 40% of ethanol and 60% of deionized water (reference medium), it was obtained an output power of 15.57 nW, for a refractive index of 1.352 RIU – **Figure 5.12**.

- **System sensitivity**

In the measurements of paracetamol samples, the EDFRC system reference (port 2 of optical coupler) was always immersed in the reference medium.

Figure 5.13 shows the output spectrum of the EDFRC system when the reference was immersed in the reference medium and the sensing head (port 3 of optical coupler) was placed in air. The EDFRC configuration was pumped with 20 mW at 976 nm.

As it is possible to see, the laser condition was not reached, due to the low level of pump power, allowing only the spontaneous emission condition.

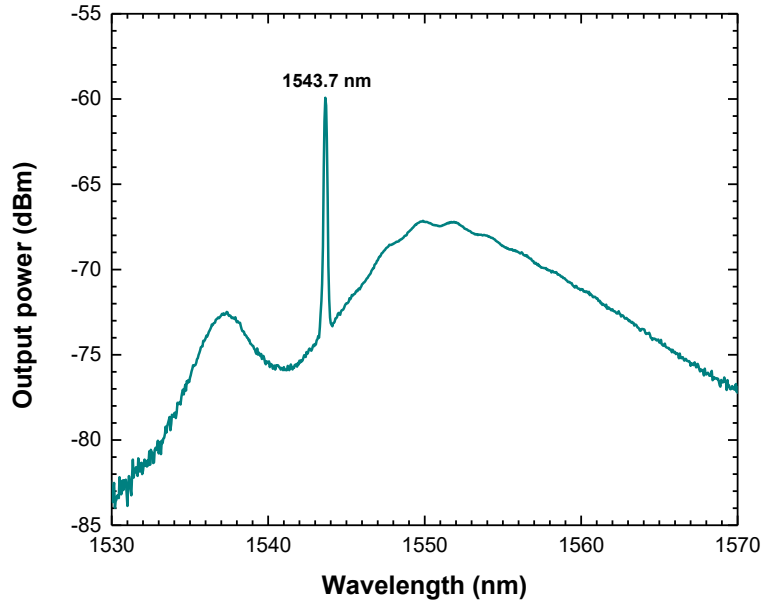


Figure 5.13. EDFRC output spectra pumped by a 976-nm laser at 20 mW, when the reference port was in the reference solution and sensing head was in air.

The paracetamol samples were measured at room temperature, and, for that, the sensing head was vertically immersed in each sample and the output power response was obtained using the power meter. **Figure 5.14** shows the linear dependence obtained between the output power sensor response and the paracetamol concentration (correlation factor of 0.995).

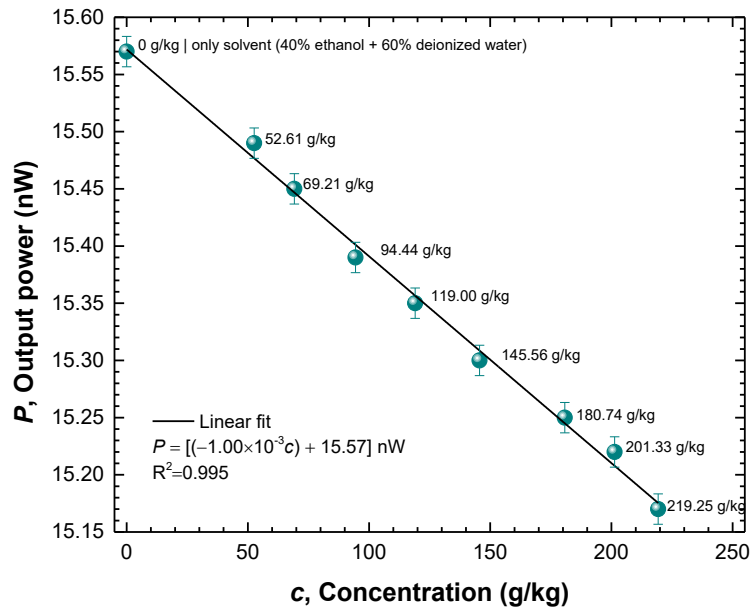


Figure 5.14. Output power levels as a function of paracetamol concentration in solution when the end of the reference port was immersed in the reference solution (40% of ethanol and 60% of deionized water) and sensing head was immersed in the paracetamol solutions.

A linear sensitivity of (-1.00 ± 0.05) pW/(g/kg) to the variation of paracetamol concentration was obtained, with ranges of 52.61 to 219.25 g/kg.

- **System resolution**

The resolution of the system was also evaluated. Two consecutive measurements of two samples with consecutive values of concentration was performed and the sensor output power response, during this process, was analyzed – **Figure 5.15**.

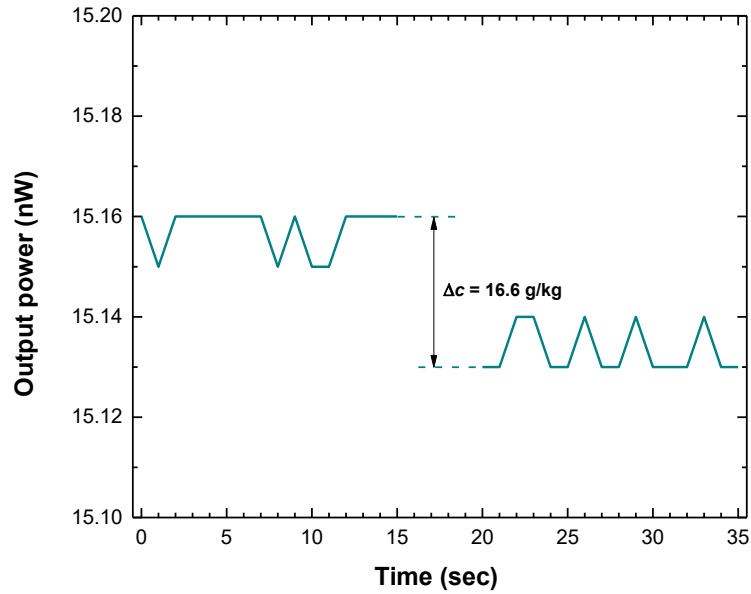


Figure 5.15. Evaluation of system resolution. The reference port was immersed in the reference solution (40% of ethanol and 60% of deionized water) and sensing head was immersed, consecutively, in paracetamol samples with consecutive values of concentration, 52.61 g/kg and 69.21 g/kg, respectively.

The minimum value of concentration (δ_c) that the sensor could discriminate, i.e., the sensor resolution, was determined as explained in **section 4.3.1 of Chapter 4** [23]. Through the sensor response (**Figure 5.15**), the variables values were obtained and present in **Table 5.1**.

Table 5.1. Determination of system resolution.

Variable	Unit	Value
σ_p	nW	5.0×10^{-3}
Δc	(g/kg)	16.6
ΔP	nW	3.0×10^{-2}
Resolution	(g/g)	5.53×10^{-3}

Using the previous values (**Table 5.1**) and applying **Equation 4.2** of **Chapter 4** (section 4.3.1), a resolution of (5.53×10^{-3}) g/g was obtained. It is important to mention that this value was also influenced by the spectral resolution of the equipment used for data acquisition.

5.2.5. Concluding remarks

In this study an interrogation system based on an EDFRC for RI measurements of liquid solutions has been presented and experimentally demonstrated. The cavity ring included a 1×3 optical coupler, where: one of the fiber output ports was used to increase the optical power of the system by means of an FBG used as a reflector and the other two ports were used as refractive sensing head and reference port, respectively. The ring cavity system did not reach the laser condition; however, it was able to perform RI measurements using only spontaneous emission and not stimulated one. This makes the developed system a more viable solution both in terms of power and economics, due to the low level of pumping power required to perform measurements. The influence of the measurand-temperature cross sensitivity effect on RI variations in this sensor interrogation system was also analyzed. The results prove, once again, the feasibility of this interrogation system for the detection of RI assisted by an FBG reflector. The system was applied to measure paracetamol liquid samples with different concentrations (range of concentrations between 52.61 to 219.25 g/kg). The sensing head allowed to measure paracetamol concentrations with a sensitivity of $[(-1.00 \pm 0.05) \times 10^{-3}]$ nW/(g/kg) and a resolution of 5.53 g/kg. These results show the potential of the configuration in monitoring the concentration of liquid solutions. Since concentration is one of the most important parameters in several processing industries, the developed ring cavity configuration can be used to monitor this parameter in real-time and in a non-invasive way, representing an alternative and low-cost technology.

5.3. Erbium-doped fiber laser based on linear cavity configuration

Two different configurations of fiber lasers based on linear cavities were developed to perform measurements of concentration in liquid solutions. In these configurations, an erbium-doped optical fiber was used as a gain medium. The fiber handling was also performed using the material referred to in **section 5.2** of this chapter.

5.3.1. Laser gain

The laser gain was provided by a commercial bi-directional EDFA. This device consists of two 3-port optical circulators and two conventional EDFAs, as is illustrated in **Figure 5.16**.

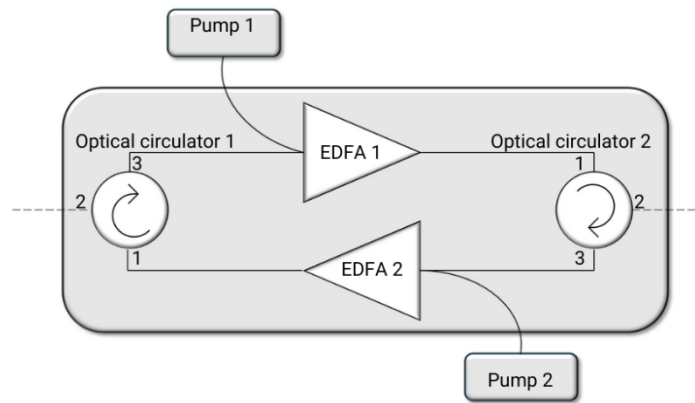


Figure 5.16. Schematic of the bidirectional erbium-doped fiber amplifier.

Each one of these pumps is independently controlled and, in this work, an appropriate pump power level was chosen to ensure laser stability. Also, the bidirectional EDFA used was fixed in a stable position to minimize the effects of bending and polarization losses.

5.3.2. Experimental configurations

The experimental setups, namely, Setup (A) and Setup (B), are shown in **Figure 5.17**.

In Setup (A), **Figure 5.17 (a)**, the linear cavity was obtained using two distinct mirrors: a fiber loop mirror and an FBG. The use of these two different mirrors results in an increase in the ASE, generated by the fiber tip (sensing head), and, simultaneously, an increase in the stimulated

emission by the FBG mirror. As illustrated in **Figure 5.17 (a)**, the fiber loop mirror allows the reflection of all the light obtained from the EDFA. A portion of this light is then reflected by the FBG mirror, resulting in stimulated emission, and the remaining light is reflected by the fiber tip, which contributes to generate ASE. Having these two laser effects, stimulated emission and ASE, it is possible to obtain a reference for the sensor implemented through this fiber laser system.

The FBG mirror used is a commercial grating, centered at 1567.8 nm, with a reflectivity of 97.59% and a bandwidth of 0.243 nm at -3 dB.

To acquire the laser optical power, a 99:1 optical coupler was used. In this way, during the measurements performed, 1% of the system signal was extracted by means of a power meter. Concerning the sensing head, it corresponds to a standard SMF 28e tip, that works as an intensity sensor, and it was cleaved at 20 mm after the FBG.

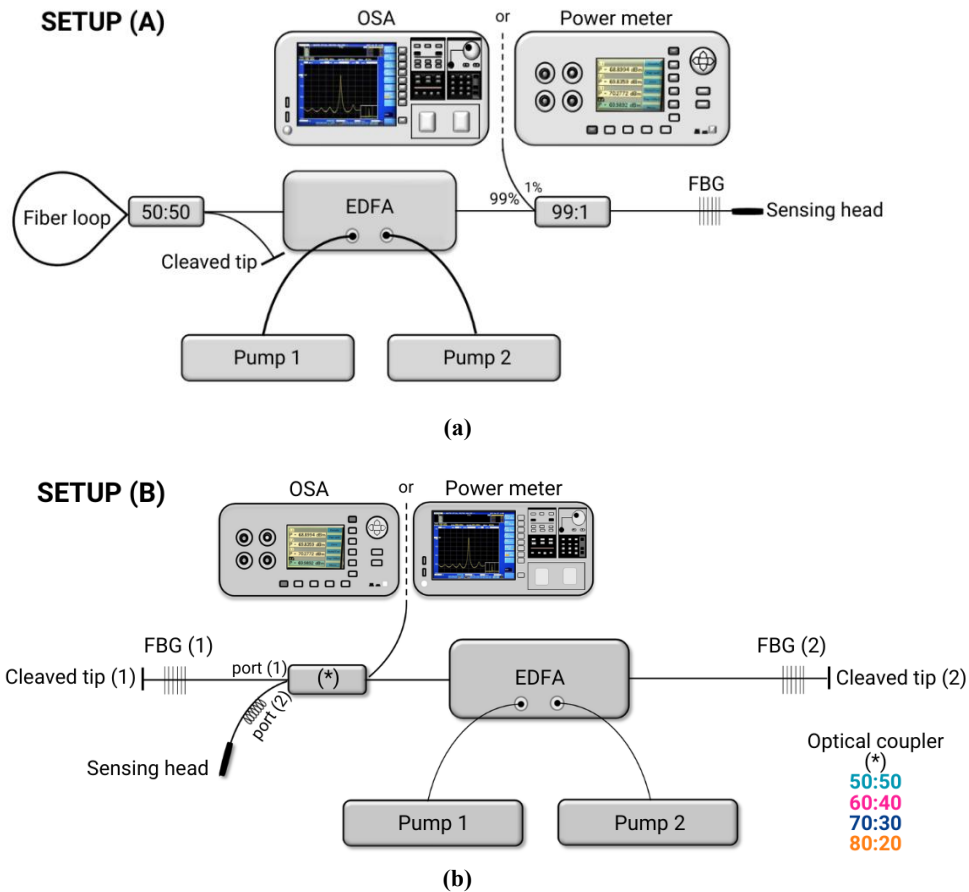


Figure 5.17. Experimental setup of the fiber laser systems based on linear cavities: **(a)** Setup (A); **(b)** Setup (B), where (*) represents the optical coupler used in each fiber laser configuration.

Regarding Setup (B), **Figure 5.17 (b)**, the linear cavity included two 8 mm length commercial FBG reflectors (FBG₁ and FBG₂), with a reflectivity of 99% and centered at 1560 nm, located at both ends of the linear cavity. To ensure the Fresnel reflection and simultaneously increase ASE, both optical fiber ends were cleaved as can be seen in **Figure 5.17 (b)**: cleaved tip (1) and cleaved tip (2). Located between these two reflectors were a 2×2 optical coupler and the bidirectional EDFA. Finally, FBG₁ was connected to the output port 1 of the fiber coupler while the sensing head, based on a standard SMF 28e tip, was connected to the output port 2.

During the experiments, using the configuration shown in **Figure 5.17 (b)**, different optical couplers with various coupling ratios were tested to extract part of the reflected optical signal to be measured. In the measurements performed, percentages of 50%, 40%, 30% or 20% of optical power were extracted and evaluated by using a power meter and an OSA.

It is important to notice that, and as it was also referred, in both configurations (**Figure 5.17**), the sensing head corresponds to a standard SMF tip, and its operating mechanism relies on the Fresnel reflection (see **Figure 5.8** of this **Chapter 5** and section 4.2.1 of **Chapter 4**).

5.3.3. Linear fiber lasers characterization

- **Output spectrum and threshold current**

The fiber laser systems, Setups (A) and (B), were characterized by the optical power meter and the OSA (recall **Figure 5.17**). The power meter was used to determine the relationship between the optical output power and the laser diode drive current, while the output spectrum of each fiber laser system was obtained using the OSA.

For Setup (A), a threshold current of 139 mA was obtained, as is shown in **Figure 5.18**. In the inset of **Figure 5.18** it is possible to see a maximum output power level of -12 dBm, centered at 1567.8 nm, measured with an OSNR of 54 dB, achieved with a laser diode drive current of 250 mA. The observed peak corresponds to the FBG filter.

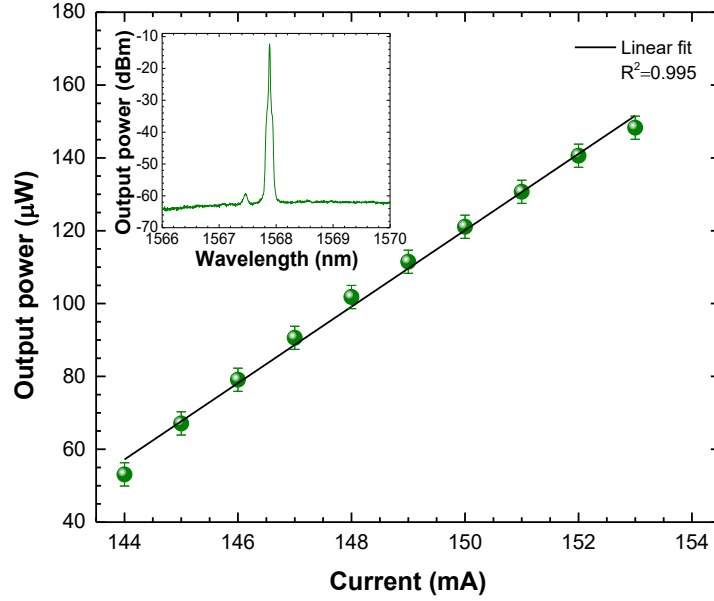
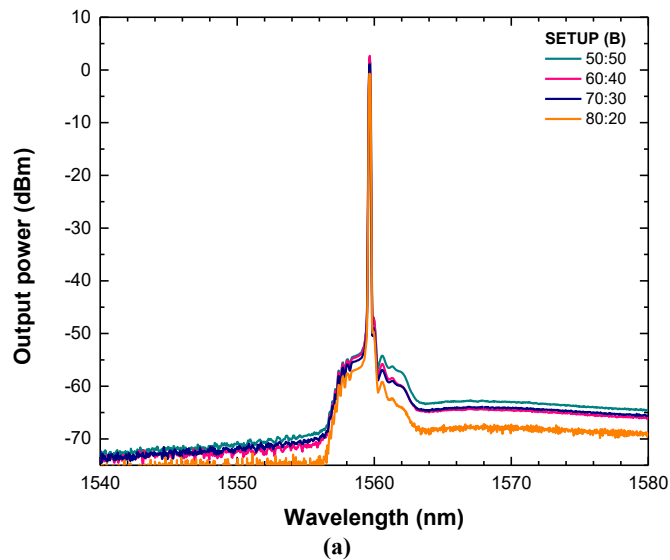


Figure 5.18. Relation between optical output power and laser diode drive current for Setup (A). Inset: Fiber laser system output spectrum.

For Setup (B), each situation tested with different optical couplers resulted in a threshold current of 150 mA for all the fiber laser systems (**Figure 5.19 c**), except for the one using a 50:50 optical coupler (**Figure 5.19 b**), which had a threshold current of 155 mA. This happens because the 50:50 optical coupler generates higher intern losses, compared to the other optical couplers used (60:40, 70:30 and 80:20).



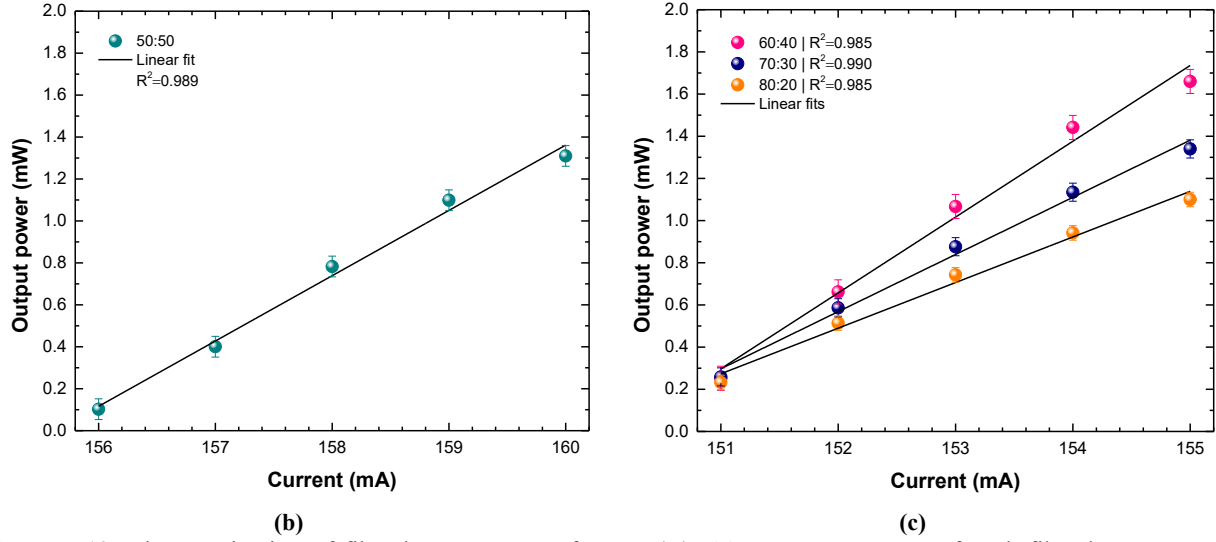


Figure 5.19. Characterization of fiber laser systems of Setup (B). (a) Output spectrum of each fiber laser system, using different optical couplers. Optical output power as a function of the laser diode drive current for the fiber laser system using the optical couplers: (b) 50:50; (c) 60:40, 70:30 and 80:20.

According to the output spectrum of each configuration (**Figure 5.19 a**), in all of them, a single emission line centered at 1560 nm, with an output power level higher than -5 dBm and with an OSNR of about 60 dB, were measured.

All the linear cavity configurations (see Inset of **Figure 5.18** and **Figure 5.19 a**) reached the laser condition, with a presence of both laser effects: ASE and stimulated emission.

• Influence of temperature

In both experimental configurations, Setups (A) and (B), commercial FBGs were used. For this reason, the influence of temperature in the output power response of the systems was analyzed. Only Setup (A) was used to perform this study (**Figure 5.17 a**), since in both configurations, the gratings perform the same role: they were used as optical mirrors/reflectors. For this, the FBG mirror used in Setup (A) was immersed in a temperature-controlled water bath (the sensing head remained in contact with air). During the water bath heating, the optical spectra of the fiber laser system were obtained through the OSA – inset of **Figure 5.20 (a)**, and the output power response was obtained using the optical power meter – **Figure 5.20 (b)**.

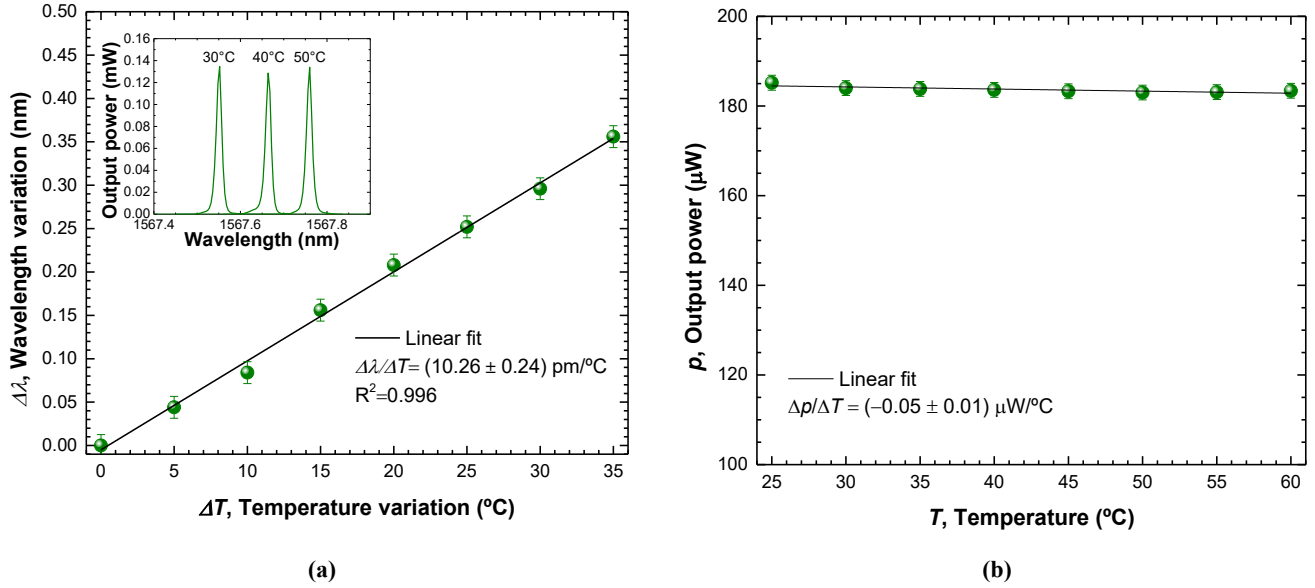


Figure 5.20. Influence of temperature in the fiber laser system output power response of Setup (A). **(a)** Variation of the FBG central wavelength as a function of temperature. Inset: output spectra, only presented in the FBG mirror spectral range; **(b)** Integrated output power response.

The results **Figure 5.20 (a)** show a wavelength dependence on temperature ($\sim 10 \text{ pm}/^{\circ}\text{C}$) during heating, caused by the thermo-optical effect that changes the material effective RI [24]. However, the output power response remains approximately constant ($\sim 0.18 \text{ mW}$) – **Figure 5.20 (b)**. This proves that the output power response of the system is not affected by temperature, as an external factor.

- **System stability**

The stability of the systems response during the measurements was also studied. For Setup (A), it was used a liquid sample with a RI of 1.3642 RIU and for the configurations of Setup (B) it was used a liquid sample with a RI of 1.3626 RIU. The sensing head was vertically immersed in the samples for 120 minutes and the output power level was recorded every 5 minutes using the optical power meter. The results (**Figure 5.21**) show that the output power level did not change significantly at room temperature over a long period of time, which proves the stability of all the systems response, during measurements.

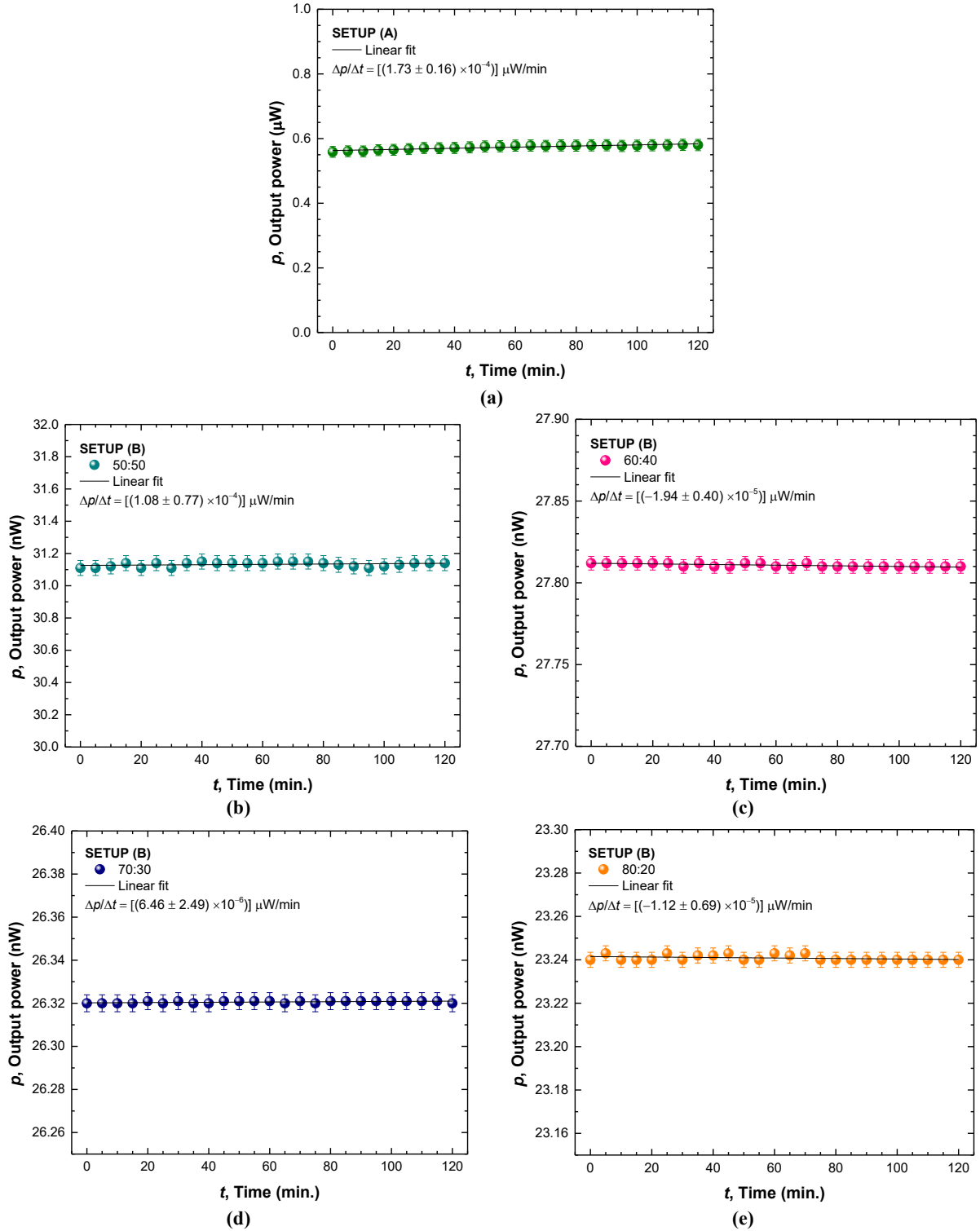


Figure 5.21. Long-term stability evaluation of fiber laser systems. (a) Setup (A); and for Setup (B), using different optical couplers: (b) 50:50; (c) 60:40; (d) 70:30; (e) 80:20.

5.3.4. Sensing applications

The sensitivity of the fiber laser systems for concentration measurements in liquid solutions was tested using paracetamol samples with varying concentrations. The samples were prepared in a controlled environment, as explained in **section 5.2.4**, and its characterization was performed using an Abbe refractometer. **Figure 5.22** shows this characterization for both samples set that were used during the experiments using the experimental Setup (A) and (B), respectively.

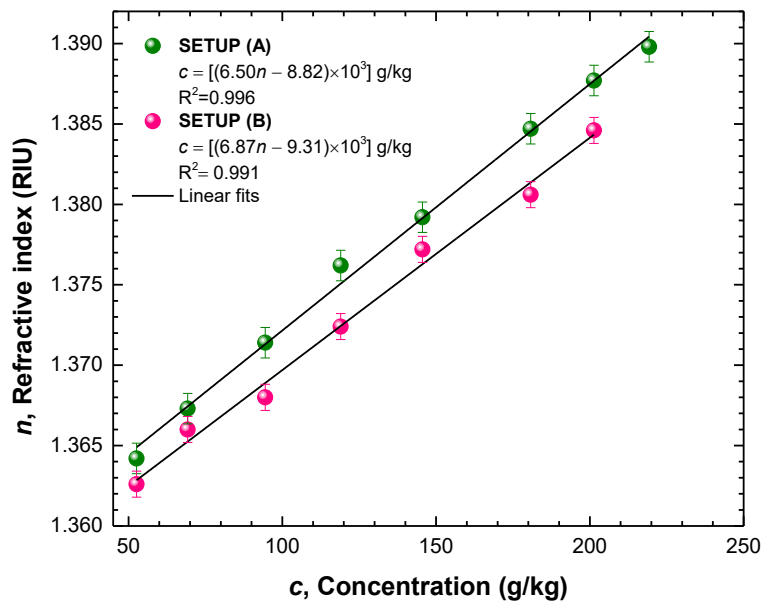


Figure 5.22. Characterization of paracetamol liquid samples. Concentration of paracetamol in solution as a function of RI, for each set of samples used in Setup (A) and Setup (B), respectively.

It is important to notice that, despite the samples having the same value of concentration, for each set of samples used in Setup (A) and Setup (B), respectively, the RI changes, because the measurements were realized at different times and under different conditions, such as different environment temperatures.

- **System sensitivity**

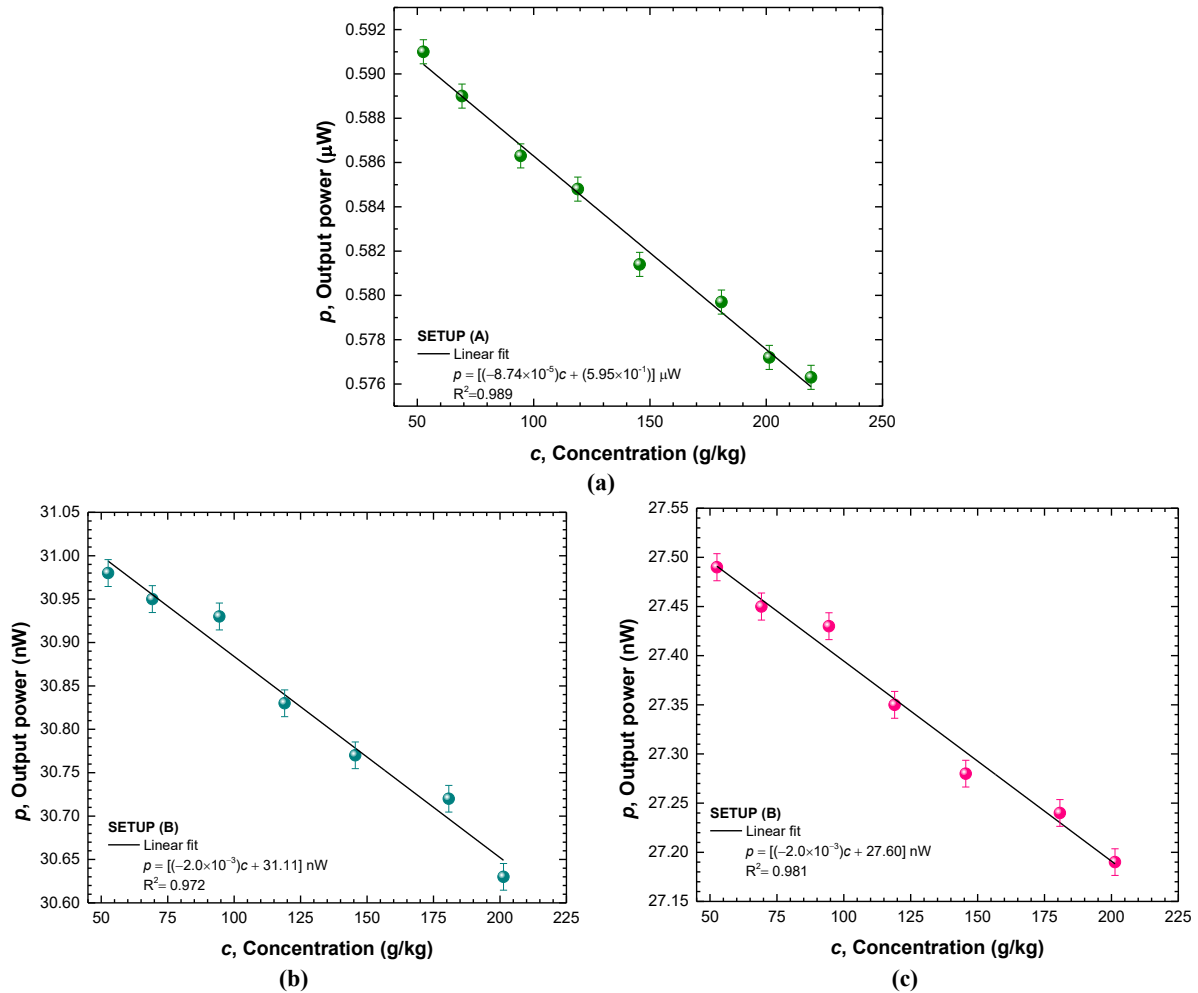
In all the measurements performed by Setup (A), a pumping rate above the threshold value, namely 150 mA, was used. However, with Setup (B), these measurements could only be performed at a

pumping rate equal to the experimentally obtained threshold current (see section 5.3.3), because, above the threshold current, the fiber laser system became insensitive to variations of paracetamol concentration (the sensor response became instable).

The sensing head of each setup (please recall **Figure 5.17**) was vertically immersed in each liquid sample and the output power level was obtained using the power meter. To avoid possible contamination and the formation of paracetamol residuals around the fiber, the sensing head was cleaned with ethanol, after each measurement.

Figure 5.23 shows the output power response obtained in each measurement as a function of paracetamol concentration for each fiber laser system.

As expected, all implemented fiber laser configurations show a linear sensitivity to changes in paracetamol concentration, within ranges of 52.61 to 219.25 g/kg for Setup (A), and of 52.61 to 201.33 g/kg for Setup (B) – **Figure 5.23**.



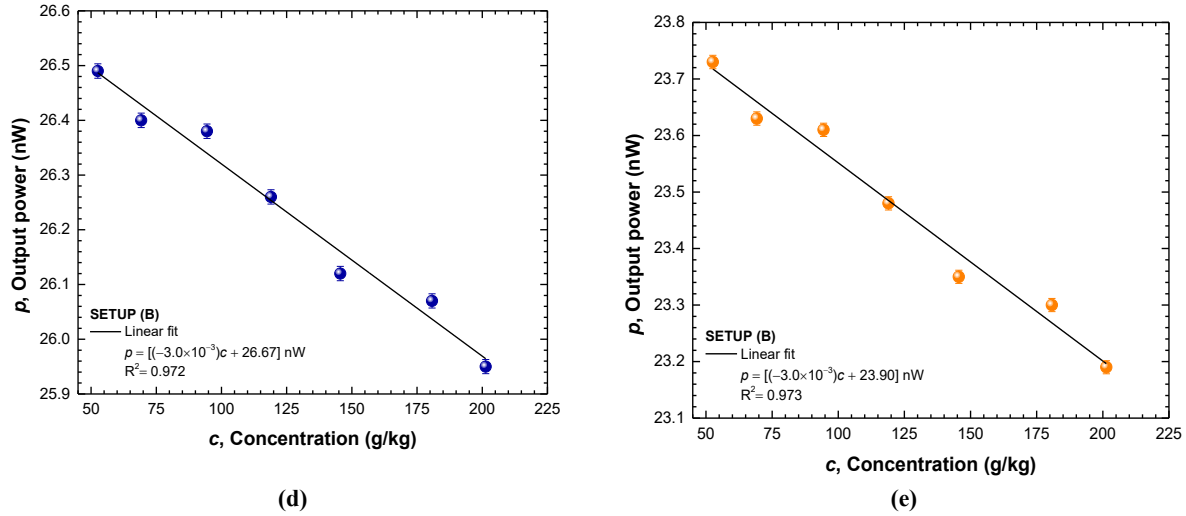


Figure 5.23. Optical output power as a function of paracetamol concentration for each fiber laser system. (a) Setup (A); and for Setup (B), using different optical couplers: (b) 50:50; (c) 60:40; (d) 70:30; (e) 80:20.

Table 5.2 summarizes the results obtained for all the setups in relation to its sensitivity.

Table 5.2. Sensitivity of fiber laser systems to variations of paracetamol concentrations.

Unit	Setup (B)				
	Setup (A)	50:50	60:40	70:30	80:20
pW/(g/kg)	(-87.44 ± 3.40)	(-2.00 ± 0.16)	(-2.00 ± 0.15)	(-3.00 ± 0.24)	(-3.00 ± 0.24)

As is possible to see in **Table 5.2**, Setup (A) presented the highest sensitivity value (**Figure 5.23 a**). Setup (B) presented distinct sensitivities depending on the coupling ratios used. For coupling ratios of 50:50 and 60:40, similar sensitivities were obtained (**Figure 5.23 b** and **c**, respectively). The other two configurations, using coupling ratios of 70:30 and 80:20, revealed to have the same sensitivity (**Figure 5.23 d** and **e**, respectively).

- **System resolution**

The resolution of both Setups, (A) and (B), was also evaluated, using the method explained in **section 4.3.1** of **Chapter 4**. The two samples of paracetamol with consecutives values of concentration used were: 52.61 g/kg and 69.21 g/kg.

For each setup, the sensing head was vertically immersed in each sample and the sensor response was acquired using the power meter. **Figure 5.24** shows the results achieved for each fiber laser configuration, i.e., for Setup (A) and for all the configurations of Setup (B), using different optical couplers.

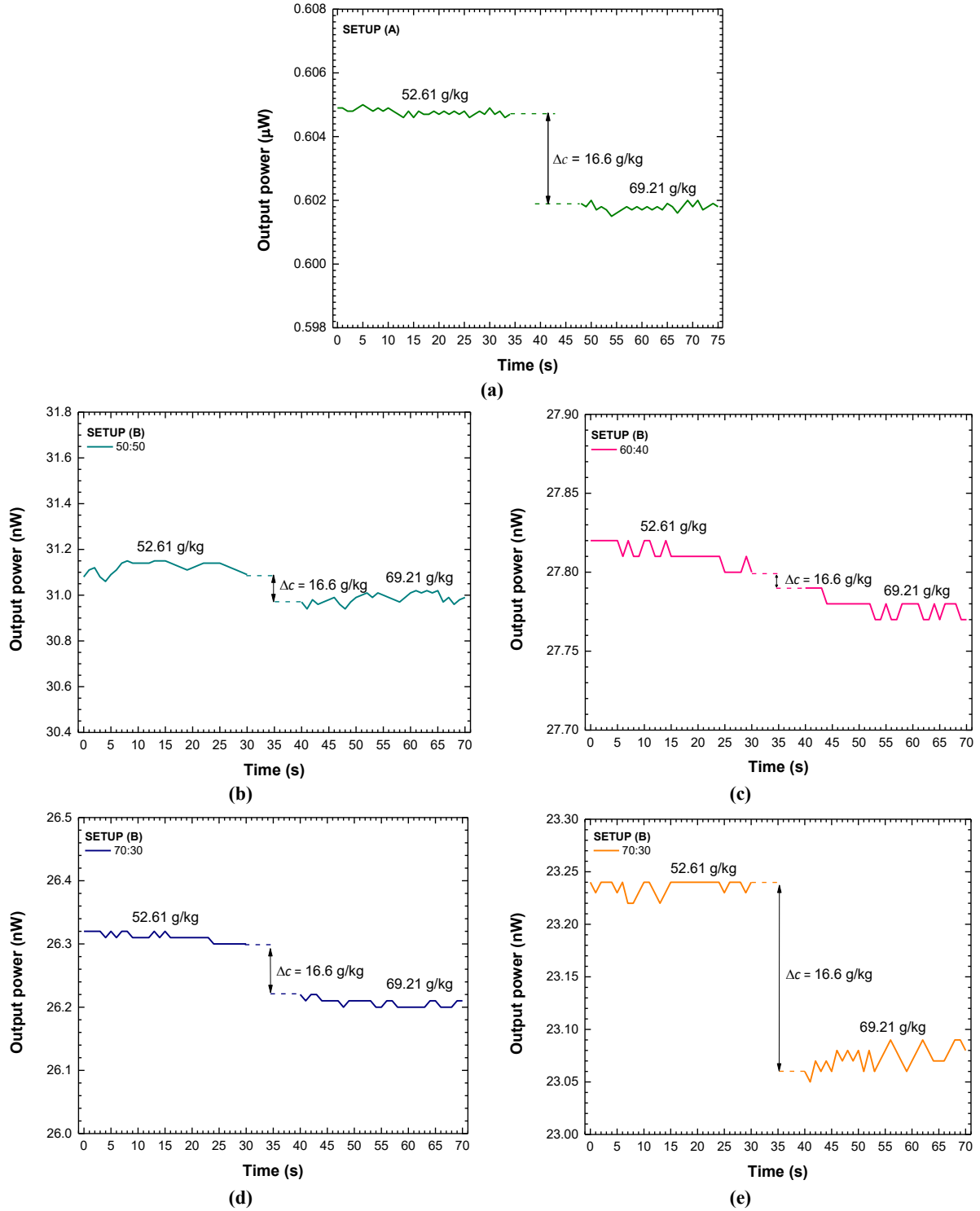


Figure 5.24. Resolution of the developed fiber laser systems. (a) Setup (A); and for Setup (B), using different optical couplers: (b) 50:50; (c) 60:40; (d) 70:30; (e) 80:20.

Through the sensor response shown in Figure 5.24, the resolution of each fiber laser configuration was calculated applying **Equation 4.2** of **Chapter 4 (section 4.3.1)** [23].

The variables used in this calculation and the corresponding results for each sensing system are presented in **Table 5.3**.

Table 5.3. Determination of fiber laser systems resolution.

Variable	Unit	Setup (B)				
		Setup (A)	50:50	60:40	70:30	80:20
σ_p	nW	0.25	0.04	0.01	0.01	0.01
Δc	g/kg	16.6	16.6	16.6	16.6	16.6
ΔP	nW	3.00	0.21	0.05	0.12	0.19
Resolution	g/g	(2.77×10^{-3})	(6.32×10^{-3})	(6.64×10^{-3})	(2.77×10^{-3})	(1.75×10^{-3})

It is important to refer that the resolution values calculated were also influenced by the spectral resolution of the equipment used for data acquisition (0.01 pW).

Considering Setup (B), **Table 5.3** reveals that the highest resolution was achieved with the configuration using the 80:20 optical coupler. In this case, the amount of light that propagates inside the laser cavity is higher, compared with the other configurations (using the optical couplers with other coupling ratios, namely, 50:50, 60:40 and 70:30), which causes an increase in the ASE effect.

5.3.5. Concluding remarks

In this work two different fiber laser setups based on linear cavities to perform paracetamol concentration measurements in liquid solutions were presented. Both setups had a cleaved single-mode fiber tip, as a sensing head, that worked as an intensity sensor.

The configurations reached the laser conditions, with the presence of both laser effects, ASE and stimulated emission. It was found that the sensor output power response of the configurations varied linearly with the concentration of paracetamol, within range of 52.61 to 219.25 g/kg for Setup (A), and of 52.61 to 201.33 g/kg for Setup (B), and the laser response is independent of the paracetamol concentration. In this way, it can be used as reference.

Regarding the performance of the system, Setup (A) showed the highest sensitivity of (-87.4 ± 3.40) pW/(g/kg) and the second better result of (2.77×10^{-3}) g/g to system resolution.

These results prove the potential of fiber laser sensors to perform concentration measurements in liquid solutions. The developed linear cavity configurations can be easily implemented, and it can be used to in-line liquid measurements of concentration for the purpose of process control in several processing industries.

5.4. Final chapter remarks

This chapter demonstrates different configurations of EDFLs configurations based on ring and linear cavities.

It was found that only linear configurations reached laser conditions, with the presence of both ASE and stimulated emission. In the spectrum of ring configuration, it was only possible to see the presence of amplified spontaneous emission.

The highest laser power and optical signal to noise ratio were obtained by the linear cavity configurations.

Regarding the paracetamol concentration measurements, the sensor response of each fiber laser configuration exhibited a linear behavior with the increase of paracetamol concentration. However, the linear configurations have the best performance, allowing the measurement of paracetamol concentration with higher sensitivity and resolution.

The developed fiber laser sensors reveal to have potential application in several processing industries to perform in-line liquid measurements of concentration.

References

- [1] T. H. Maiman, "Stimulated Optical Radiation in Ruby", *Nature*, vol.187, pp.493–494, Aug. 1960, DOI:10.1038/187493a0.
- [2] G. Nemova, "Recent Developments in Fiber Lasers", *Appl. Sci.*, vol.14, n°6, 2323, Mar. 2024, DOI:10.3390/app14062323.
- [3] E. Snitzer, "Optical Maser Action of Nd^{+3} in a Barium Crown Glass", *Phys. Rev. Lett.*, vol.7, n°12, pp.444-446, Dec. 1961, DOI:10.1103/PhysRevLett.7.444.
- [4] E. Desurvire, E., *Erbium-Doped Fiber Amplifiers: Principles and Applications*. John Wiley & Sons, Inc.: Hoboken, NJ, USA, 1994, ISBN:9780471589778.

-
- [5] R. Wayne, "A Reinterpretation of Stimulated Emission as Spontaneous Emission Under Non-Thermodynamic Equilibrium Conditions", *African Review of Physics*, vol.11, 0004, pp.17-22, Mar. 2016, ISSN:2223-6589.
 - [6] S. Addanki, I. S. Amiri, and P. Yupapin, "Review of optical fibers-introduction and applications in fiber lasers", *Results in Physics*, vol.10, pp.743-750, Sept. 2018, DOI:10.1016/j.rinp.2018.07.028.
 - [7] T. K. Subramaniam, "Erbium Doped Fiber Lasers for Long Distance Communication Using Network of Fiber Optics", *Am. J. Opt. Photonics*, vol.3, n°3, pp.34-37, Aug. 2015, DOI:10.11648/j.ajop.20150303.11.
 - [8] A. W. Naji, B. A. Hamida, X. S. Cheng, M. A. Mahdi, S. Harun, S. Khan, W. F. AL-Khateeb, A. A. Zaidan, B. B. Zaidan, and H. Ahmad, "Review of Erbium-doped fiber amplifier", *Int. J. Phys. Sci.*, vol.6, n°20, pp.4674-4689, Sept. 2011, DOI:10.5897/IJPS11.782.
 - [9] D. W. Ball, *Field Guide to Spectroscopy*, SPIE Press, Bellingham, WA, 2006, ISBN:9780819463524.
 - [10] S. Milanesea, M.L. De Giorgia, L. Cerdánb, M.G. La-Placab, P.P. Boixb, H.J. Bolinkb, and M. Anni, "Quantitative comparison between different methods for the determination of the amplified spontaneous emission threshold in dye-polymer blends and perovskite thin films", *Mater. Today: Proc.*, vol.67, n°7, pp.959-963, Apr. 2022, DOI:10.1016/j.matpr.2022.04.656.
 - [11] R. A. Perez-Herrera, and M. Lopez-Amo, "Fiber Lasers for Optical Sensing Applications". In *Proceedings of the 3rd WSEAS international conference on Advances in sensors, signals and materials*, pp.125-129, Nov. 2010, Faro, Portugal, ISBN:978-960-474-248-6.
 - [12] B. Jacquier, "Rare Earth-Doped Fiber Lasers and Amplifiers". In: Rotman, S.R. (eds) *Wide-Gap Luminescent Materials: Theory and Applications*. Electronic Materials: Science and Technology, vol.2, Springer, Boston, MA, 1997, DOI:10.1007/978-1-4615-4100-4_6.
 - [13] R. Paschotta, "Lasers", *RP Photonics Encyclopedia*. <https://doi.org/10.61835/9qy>, DOI:10.61835/9qy (accessed june 04, 2024).
 - [14] S. Ali, K. A. S. Al-Khateeb, and B. Bouzid, "Comparison of the Effect Structure on Ring and Linear Cavity Lasers of Er-Doped Optical Fibers". In *Proceedings of the International Conference on Computer and Communication Engineering*, pp.546-549, May 2008, Kuala Lumpur, Malaysia, ISBN:978-1-4244-1692-9.

-
- [15] R. Correia, R. Sinha, A. Norris, S. Korposh, S. Talbot, F. U. Hernandez, and S. P. Morgan, "Optical fiber sensing at the interface between tissue and medical device". In Proceedings of the *International Conference on Biophotonics V*, 103400X, Apr. 2017, Perth, Australia. DOI:10.1117/12.2269811.
- [16] R. Yang, Z. Lianqing, Y. Zhang, X. Lou, and M. Dong, "Erbium-doped fiber ring laser sensor for high temperature measurements based on a regenerated fiber Bragg grating", *Fiber and Integrated Optics*, vol.36, n°6, pp.252-261, Dec. 2017, DOI:10.1080/01468030.2017.1407972.
- [17] J. Tian, M.-J. Hou, Y. Jiang, H. Luo, and C.-Y. Tang, "Fiber ring laser cavity for strain sensing via beat frequency demodulation", *Optics Communications*, vol.476, 126326, Dec. 2020, DOI:10.1016/j.optcom.2020.126326.
- [18] I. M. Nascimento, J. M. Baptista, P. A. S. Jorge, J. L. Cruz, and M. V. Andrés, "Erbium doped optical fiber lasers for magnetic field sensing". In Proceedings of the *24th International Conference on Optical Fibre Sensors*, pp.9634-305, Sept. 2015, Curitiba, Brazil, DOI:10.1117/12.2195073.
- [19] S. M. Idris, F. Abdullah, M. H. Al-Mansoori, M. Z. Jamaludin, and N. M. Din, "Pressure Sensing Utilizing Linear Cavity Erbium-Doped Fiber Laser", *Laser Phys.*, vol.20, pp.855–858, Marc. 2010, DOI:10.1134/S1054660X10070133.
- [20] W. A. Khaleel, and A. H. M. Al-Janabi, "High-sensitivity sucrose erbium-doped fiber ring laser sensor", *Opt. Eng.*, vol.56, n°2, 026116, Feb. 2017, DOI:10.1117/1.OE.56.2.026116.
- [21] J. Liu, M. Wang, X. Liang, Y. Dong, H. Xiao, and S. Jian, "Erbium-doped fiber ring laser based on few-mode-single mode-few-mode fiber structure for refractive index measurement", *Optics & Laser Technology*, vol.93, pp.74-78, Aug. 2017, DOI:10.1016/j.optlastec.2017.02.008.
- [22] E. Hecht, *Optics*, 5th ed., Pearson: London, UK, 2015.
- [23] L. Soares, S. Novais, A. Ferreira, O. Frazão, S. Silva, "Detection of the Crystallization Process of Paracetamol with a Multi-Mode Optical Fiber in a Reflective Configuration", *Sensors*, vol.20, n°1, 87, Dec. 2019, DOI:10.3390/s20010087.
- [24] J. Du, and Z. He, "Sensitivity enhanced strain and temperature measurements based on FBG and frequency chirp magnification", *Opt. Express*, vol.21, n° 22, pp.27111–27118, Nov. 2013, DOI:10.1364/OE.21.027111.

Chapter 6. Monitorization of crystallization in an oscillatory flow crystallizer using optical fiber sensors

6.1. Introduction

Crystallization, with its ability to control the yield, polymorphic form, purity, particle size and shape of the final product, is one of the most important operations involved in the manufacturing of APIs. Nevertheless, it is still a relatively poorly understood and poorly controlled process and so can benefit greatly from the use of PAT [1].

As explained in **Chapter 2**, the term PAT covers a variety of tools that can be used to design, analyze, and control the manufacturing processes with the aim of ensuring the quality of the final product. Its implementation requires sensors that measure the variables of interest. Generally, non-invasive sensors, which can perform real-time measurements, are the more appealing sensors, because they did not disturb the process flow [2, 3]. Also, real-time measurements avoid sample preparation and time delays. They are also preferred when the sample is difficult to access, when the offline sample may not be representative, when the process of sampling changes the material, or even when frequent sampling is required [3]. Nevertheless, in the crystallization field, sometimes real-time measurements are not feasible, particularly when the vessel of the crystallizer is very small, and the probes cannot be immersed in the process flow. An example is monitoring the temperature of process flow and the concentration of an API in an OFC.

The OFC consists of a tubular crystallizer containing evenly spaced orifice baffles which are transversely assembled to a periodically oscillating flow. These crystallizers can be operated batchwise or continuously in horizontal tubes/channels or vertical columns. The development and application of OFCs has received significant attention in the past few decades due to the rise of continuous manufacturing in the pharmaceutical industry [4].

However, the use of PAT in these crystallizers is still limited by the diameters of the probes which typically exceed the diameter of the tubes/channels.

In literature it is possible to find studies in which the concentration of APIs and the temperature of process flow during the crystallization process were measured in real-time by different PAT tools, especially based on spectroscopy fundamentals [5-10]. However, all these works were performed

in Stirred Tank Crystallizers (STC), whereas the use of PAT in OFC-like crystallizers remains forgotten.

In view of the need to monitor the concentration of APIs in real-time and the temperature in crystallizers such as OFC, in this work, optical fiber-based sensors were fabricated and experimentally demonstrated to measure the concentration of paracetamol in crystallization experiments in an OFC, operating in continuous mode. **Figure 6.1** shows a schematic representation of a planar-OFC, similar to the OFC used as a model system to validate the fiber optic-based technology developed.

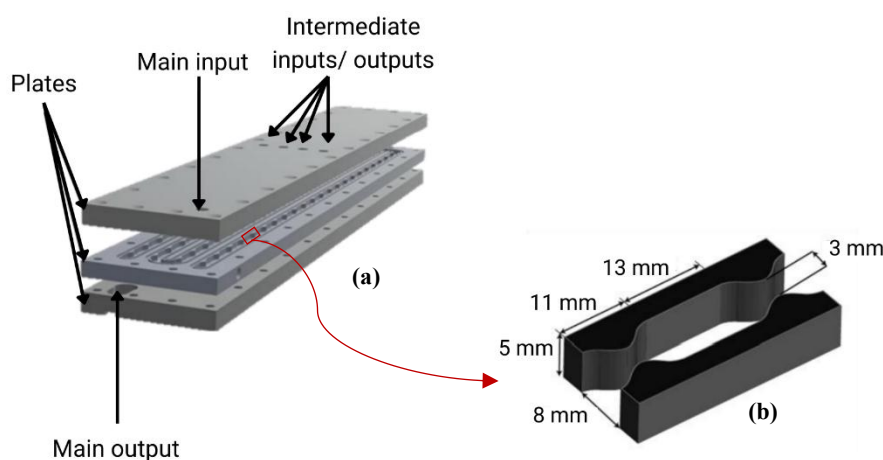


Figure 6.1. Schematic representation of planar-OFC: (a) OFC plates; (b) Dimensions of an inter-constriction cell.

The planar-OFC consists of a platelike crystallizer with three stacked plates screwed together: two polycarbonate plates, one at the base and one at the top, and one aluminum plate coated with Halar® (ECTFE, Ethylene-Chlorotrifluoroethylene, copolymer) in the middle – **Figure 6.1 (a)**. The crystallization process takes place in a channel designed with smooth periodic constrictions located between the middle and top plates, and the water of a cooling/heating jacket circulates in a straight channel located between the base and middle plates. The two channels were carved in the middle plate; the top plate seals the crystallization channel, and the base plate seals the jacket channel. The crystallization channel has 6 access points (one main input, one main output and four intermediate inputs/outputs) and comprises a volume of ~70 mL (operational volume). The dimensions of each inter-constriction cell are presented in **Figure 6.1 (b)**.

Two separate circuits of cooling/heating water were connected to the planar-OFC: cold water, generally, thermostated at 5°C by a cooling bath (Ministat 125, Huber), and hot water, generally, thermostated at 55°C by a heating bath (Ministat 125, Huber). Each circuit was controlled by two 3-way valves.

6.2. Monitorization of concentration *in situ*

A refractometric sensor was applied to measure in real-time the concentration of APIs in crystallization experiments. Paracetamol was used as a model system due to the extensive literature available for this API [11-13].

The refractometric sensor was fabricated by a simple and inexpensive method that consisted in splicing a short section of a multimode fiber (MMF) to a single mode fiber (SMF). The compact geometry of this sensor, with an external diameter of just 125 μm , allowed to measure in real-time the concentration of paracetamol both in a STC operating in batch, and in an OFC operating in continuous. Monitoring in the STC was carried out to compare the results obtained in this crystallizer with the results obtained during the monitoring in the OFC and thus, to validate the developed technique.

This technique shows the potential to monitor the concentration of APIs in crystallizers of different sizes and geometries, as an alternative to more expensive and complex analysis equipment.

6.2.1. Sensing head and portable interrogation system

The sensor used in this experiment is the same as presented in **Chapter 4 (section 4.3)** of this document. A section of a GI-MMF (core diameter of 62.5 μm), spliced to a SMF 28e (core diameter of 8.2 μm), was used as a refractometric sensor to measure the concentration of paracetamol in crystallization experiments. These fibers have a germanium doped silica core with a pure silica cladding (cladding diameter of 125 μm , for both fibers) and a mechanically strippable acrylate coating. As previously referred, the refractometric sensor was fabricated by splicing a section of MMF with a length of 10 cm to a SMF by means of a splicing fusion machine (TYPE- 72C), thus forming a MMF fiber tip. Before splicing, the fibers acrylate coating was removed by cutting pliers and then the fibers were cleaned with ethanol. The uncoated fibers were

cleaved using a cleaver machine (FC-6RS, Sumitomo Electric) to ensure the perpendicularity at the fiber-ends. The refractometric sensor was connected to an optical interrogator (Bragg METER FS22) and the response was recorded by data acquisition software (Bragg MONITOR SI) at 1550 nm.

The portable interrogation system, and the refractometric sensor operating in reflection, is presented in **Figure 6.2**.

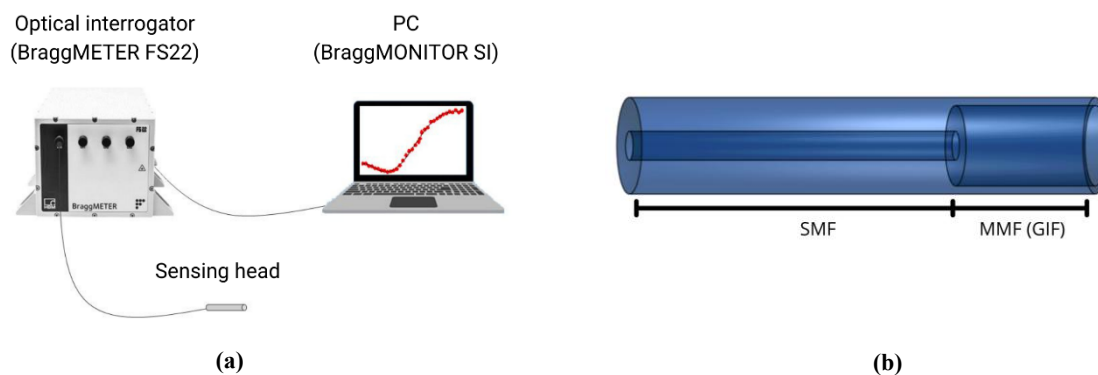


Figure 6.2. Schematic representation of the experimental setup and sensing head. **(a)** Portable interrogation system; **(b)** Detail of sensing head.

In relation to the refractometric sensor operating mechanism, it works as follows: the light propagates inside the fiber by total internal reflection; when the light reaches the fiber/liquid interface, it is partly transmitted into the liquid and partly reflected into the fiber. The sensor measures the spectrum and the optical power of the reflected wave light (please, see **Chapter 4, section 4.3.1**) [14].

6.2.2. Measurements of paracetamol liquid solutions

Ten standard solutions of paracetamol (CAS, Chemical Abstracts Service, registry number 103-90-02, min. 99% purity, supplied by Sigma-Aldrich) in a solvent mixture of 40% (v/v) ethanol/water were prepared at room temperature ($\sim 20^{\circ}\text{C}$). The concentration of the solutions ranged from 53 to 261 g/kg (g of paracetamol per kg of solvent), corresponding to a refractive index (RI) range of 1.3634 RIU to 1.3947 RIU – **Table 6.1** (please, see **Chapter 4, section 4.3.1**). The RI of each solution was measured by an Abbe refractometer (ATAGO, DR-A1) and as

expected, the increase of concentration lead to an increase of optical density of solutions, which resulted in an increase of RI.

Table 6.1. Characterization of paracetamol liquid samples.

Sample number	Refractive index (RIU)	Concentration (g/kg)
1	1.3634	52.61
2	1.3659	69.21
3	1.3697	94.44
4	1.3734	119.00
5	1.3774	145.56
6	1.3827	180.74
7	1.3858	201.33
8	1.3885	219.25
9	1.3907	233.86
10	1.3947	260.41

It is important to notice that the samples concentration range was chosen according to the variation of paracetamol concentration expected inside the OFC and STC crystallizers.

- **Calibration curve and system sensitivity**

The sensing head was vertically immersed in each standard solution and its optical power response was recorded and monitored – **Figure 6.3 (a)**. Through this optical power response, and at a measuring wavelength of 1550 nm, the calibration curve relating the RI/ concentration and optical power was plotted – **Figure 6.3 (b) and (c)**.

Posteriorly, this calibration allowed the concentration of paracetamol in the crystallizers to be monitored during the crystallization process.

As it is possible to see in **Figure 6.3 (b) and (c)** the optical power response of the sensor shows a linear dependence according to the samples concentration/RI. This response was obtained with a sensitivity to paracetamol RI variation of (-64.63 ± 2.27) dB/RIU, which corresponds to a concentration sensitivity of (-9.73 ± 0.34) dB/(g/g).

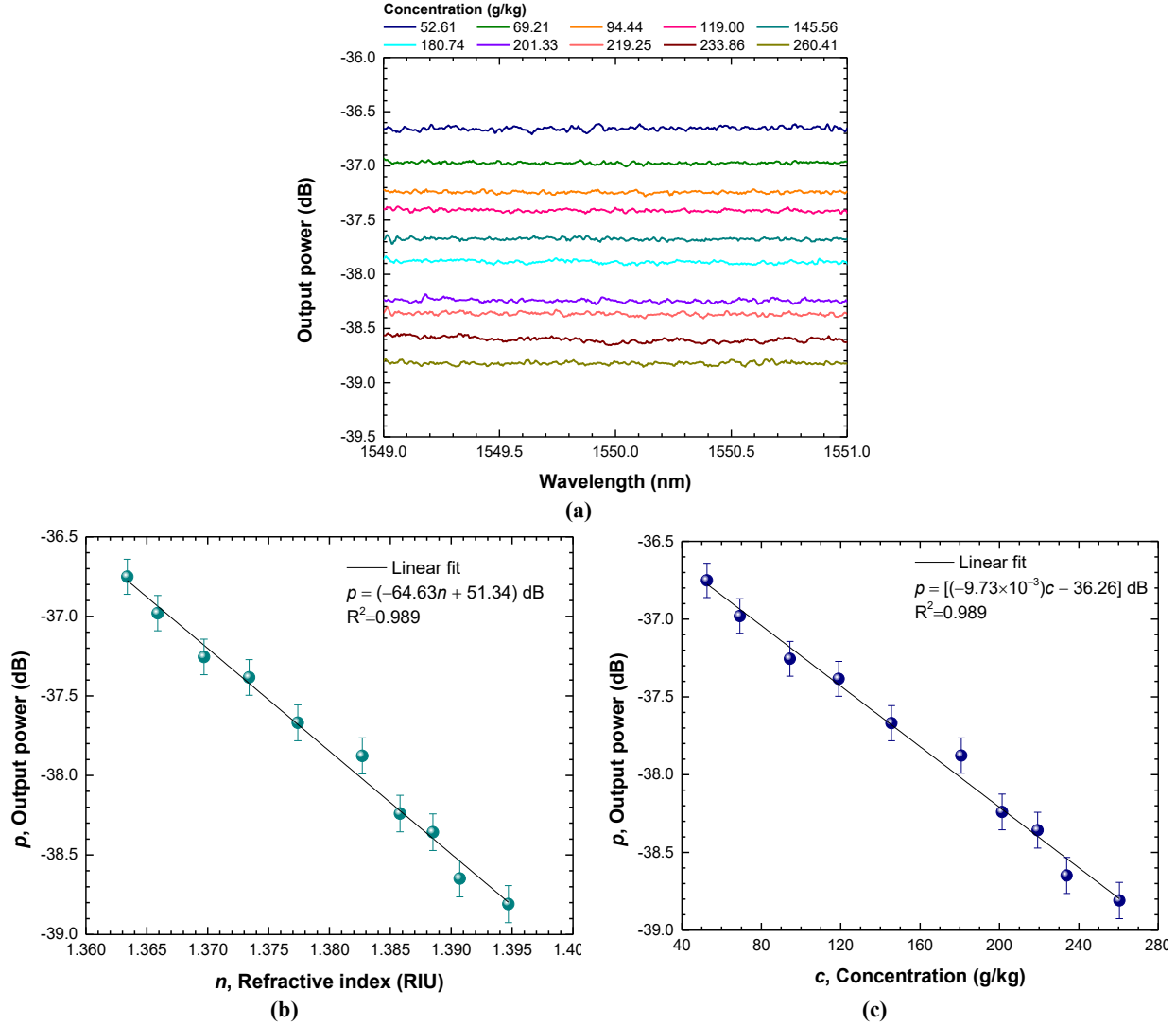


Figure 6.3. Sensor calibration. (a) Output spectrum for each paracetamol sample measured; (b) Sensor calibration to paracetamol refractive index; (c) Sensor calibration to paracetamol concentration variations.

- **Influence of temperature on system performance as external factor**

Using the same experimental setup (Figure 6.2), the influence of temperature in the performance of the fabricated sensor, as an external factor, was also evaluated. During the crystallization, the process flow is subjected to variations of temperatures. In this way, it is important to evaluate the influence of this parameter on sensor performance.

For this, the sensing head was immersed in a temperature-controlled water bath (range of temperatures from 25°C to 70°C) and the sensor optical power response was obtained and analyzed, at a measuring wavelength of 1550 nm (Figure 6.4).

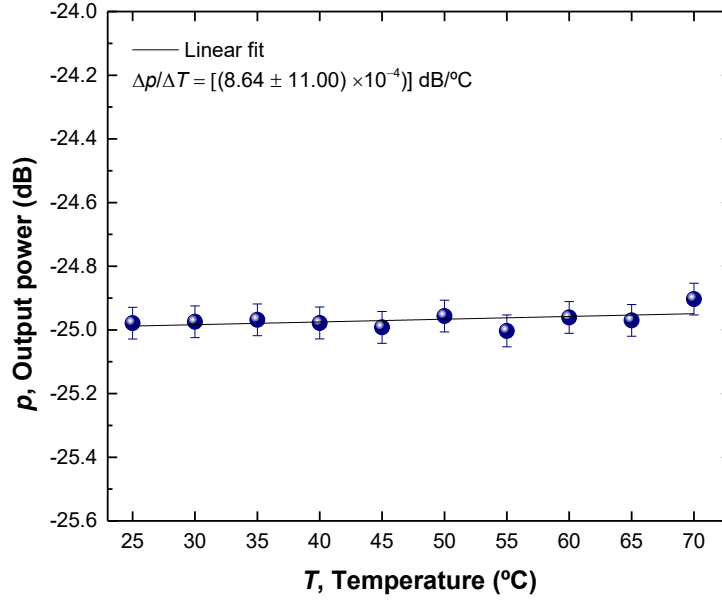


Figure 6.4. Influence of temperature in the sensor performance.

The results revealed a residual sensitivity of $[(8.64 \pm 11.00) \times 10^{-4}]$ dB/°C to temperature variations, which proved that the performance of the sensor developed was not affected by temperature fluctuations.

- **System limit of detection**

The system limit of detection (LOD) was determined. The LOD corresponds to the smallest value of the measurand, in this case, the small value of RI and/or concentration, that sensor can reliably detect and distinguish from the background noise or baseline signal, typically with a level of certain equal to 95% [15].

In a linear regression, the calculation of LOD can be expressed as:

$$LOD = 3\hat{\sigma}/b \quad (6.1)$$

In **Equation 6.1**, $\hat{\sigma}$ and b correspond to the standard deviation of y-residuals and to the slope of the regression line, respectively.

Regarding the standard deviation of y-residuals, $\hat{\sigma}$, it is calculated using **Equation 6.2**, where y_i corresponds to the observed value/experimental value, \hat{y}_i is the predicted value, and n is the number of observations, i.e., number of samples measured [16].

$$\hat{\sigma} = \sqrt{\frac{1}{(n-2)} \times \sum_{i=1}^n (y_i - \hat{y}_i)^2} \quad (6.2)$$

Applying **Equations 6.1** and **6.2**, LOD values of (3.45×10^{-3}) RIU, in relation to RI, and of ~ 0.02 g/g, in relation to concentration, were obtained.

Table 4.2 summarizes the variable values used in these calculations. It is important to notice that the slope values, b , i.e., system sensitivities, were previously determined (**Figure 6.3 a and b**).

Table 6.2. Determination of system LOD (values rounded to the nearest hundredth).

Variable	Value
$\hat{\sigma}$	0.07
n	8
b	$-64.63 \text{ dB/RIU} \mid -9.73 \text{ dB/(g/g)}$
LOD	$(3.43 \times 10^{-3}) \text{ RIU} \mid 0.02 \text{ g/g}$

- **System resolution**

The resolution of the system developed (**Figure 6.2**) was determined using the same method shown in **Chapter 4, section 4.3.1**.

The sensing head was consecutive immersed in two paracetamol samples, with two consecutive values of RI/concentration. The system output power response obtained during these measurements is shown in **Figure 6.5**.

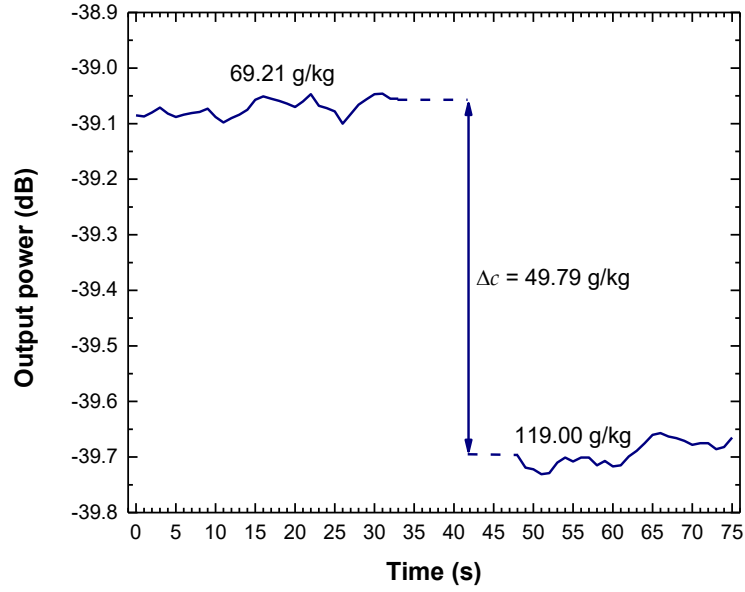


Figure 6.5. Resolution of the developed system.

The system resolution, or the minimum value of RI (δ_c) that the sensor could discriminate, was then determined through the previous response (**Figure 6.5**) and applying **Equation 4.2** (**Chapter 4**) [17]. **Table 6.3** shows the variable used in this calculation.

Table 6.3. Determination of system resolution (values rounded to the nearest hundredth).

Variable	Unit	Value
σ_p	dB	(1.98×10^{-2})
$\Delta n \mid \Delta c$	RIU \mid (g/kg)	$(7.50 \times 10^{-3}) \mid 49.79$
ΔP	dB	(5.88×10^{-1})
Resolution	RIU \mid (g/g)	$(5.06 \times 10^{-4}) \mid (3.36 \times 10^{-3})$

A resolution of (5.06×10^{-4}) RIU was obtained, which corresponds to a resolution of (3.36×10^{-3}) g/g, in terms of concentration.

6.2.3. Monitorization of concentration in crystallizers

The concentration of paracetamol was monitored in real-time, under the same experimental conditions, in a STC operating in batch and in an OFC operating in continuous. The purpose was

to compare the results obtained in the two monitoring to prove the potential of the developed technology to monitor API concentrations in crystallizers, regardless of their geometry.

- **Stirred Tank Crystallizer (STC)**

The STC consists of a 1 L jacketed glass flask with a built-in stirring system. The temperature inside the flask is measured by a thermometer and controlled by a water-cooling bath circulating in the jacket. Usually, during the crystallization process in this type of crystallizer, the concentration of the mother liquor is measured using an expensive tool, the Attenuated Total Reflectance (ATR) immersion probe (Katana 6, Hellma). In this experiment, the concentration of paracetamol in the STC mother liquor was measured by the developed refractometric sensor, as suggested in **Figure 6.6**.

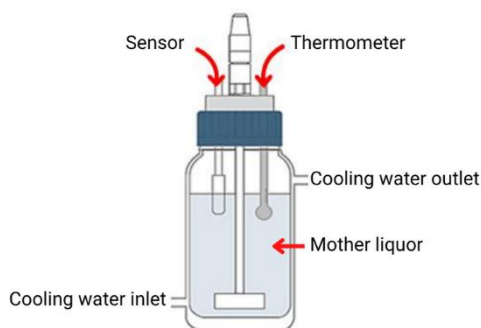


Figure 6.6. Experimental setup of the Stirred Tank crystallizer.

A 200 g/kg solution of paracetamol in 40%(v/v) ethanol/water was stirred at 150 rpm and kept at 45°C. The temperature of the solution gradually decreased when the temperature of the cooling bath was reduced to 25°C. When the temperature of the solution reached 25°C, seeds of paracetamol were introduced. The addition of seeds prevented the formation of crystals on the surface of the refractometric sensor, which could interfere with the signal measured by the sensor. The inset of **Figure 6.7** shows the evolution of the optical power measured by the sensor during the crystallization process in the STC. Through the calibration curve (please, recall **Figure 6.3**) it was possible to determine the variation of paracetamol concentration in the mother liquor, during all the process and the respective RI variation – **Figure 6.7**.

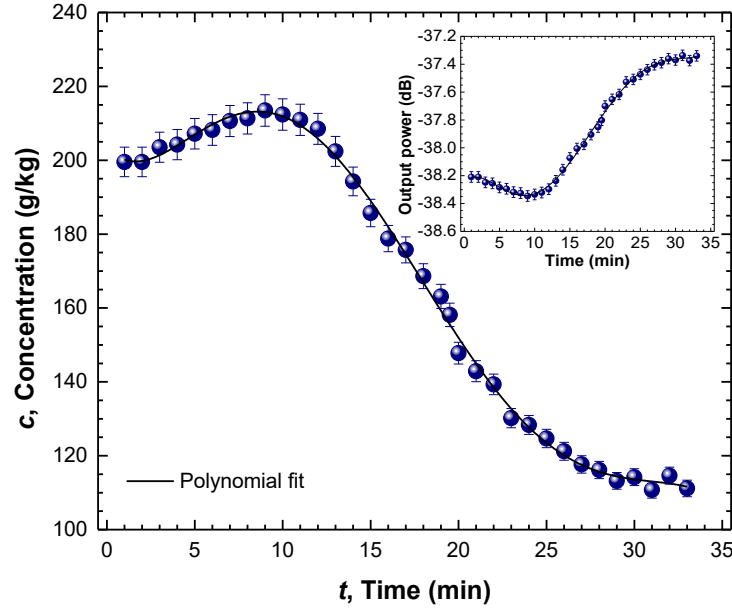


Figure 6.7. Paracetamol concentration during crystallization in the STC. Inset: Evolution of the optical power of the fiber tip sensor during crystallization.

Initially, the sensor measured a concentration close to 200 g/kg, when paracetamol was fully dissolved. When the seeds were introduced, there was a slight increase in concentration due to the increase of optical density/RI. Then, the concentration of paracetamol decreased due to crystal growth and secondary nucleation, which reduced the optical density and the RI of the solution. When the concentration approached the solubility of paracetamol at 25°C, the system reached the thermodynamic equilibrium, and the concentration of paracetamol stabilized at 100–120 g/kg, respectively. The evolution of paracetamol concentration during the crystallization process shown in **Figure 6.7** also presented a sixth-order polynomial approximation. The data of this approximation is demonstrated in **Table 6.4**.

Table 6.4. Variation of paracetamol concentration during crystallization process in the STC. Function of the sixth-order polynomial approximation ($c = a_0 + a_1t + a_2t^2 + a_3t^3 + a_4t^4 + a_5t^5 + a_6t^6$).

	a_0	a_1	a_2	a_3	a_4	a_5	a_6
Value	203.57	-5.29	2.13	-0.23	(9.43×10^{-3})	$-(1.64 \times 10^{-4})$	(9.90×10^{-7})
Standard Error	± 3.77	± 2.82	0.68	$\pm (7.31 \times 10^{-2})$	$\pm (3.86 \times 10^{-3})$	$\pm (9.81 \times 10^{-5})$	$\pm (9.60 \times 10^{-7})$
R²	0.997						

- **Oscillatory Flow Crystallizer (OFC)**

The experimental setup of the OFC is presented in **Figure 6.8**.

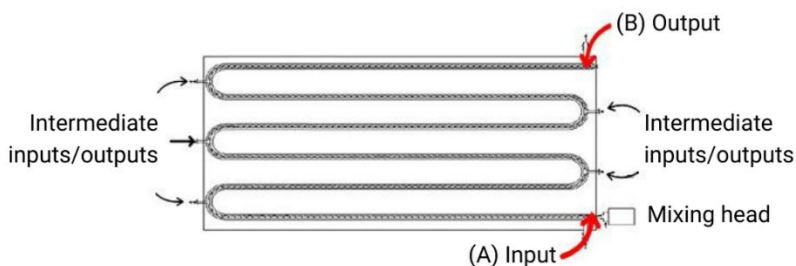


Figure 6.8. Experimental setup of the Oscillatory Flow crystallizer.

As previously referred, the OFC was constructed with three plates: (1) a Teflon plate at the base, (2) a Teflon plate at the middle, and (3) a polycarbonate plate at the top.

In the middle plate, two channels were carved: one channel designed with smooth periodic constrictions at the top where the crystallization takes place, and a straight channel at the base where the water of a cooling bath circulates.

Besides its optimized geometry, the OFC has also optimum dimensions that allow the maximizing rentability of crystallization process [17]. It is important to refer that, because of the OFC channels dimensions, the ATR-probe is not used to determine the concentration of the process flow, during the crystallization process.

Initially in this experiment, the OFC was filled with ethanol and thermostated at 25°C. The frequency and the amplitude of oscillation were set at 4 Hz and 4 mm (peak-to-peak in the piston), respectively. Then, a 200 g/kg solution of paracetamol in 40%(v/v) ethanol/water at 45°C was fed into the OFC by a peristaltic pump (BT300-2J, supplied by Longer Pump) at 40 mL/min. The solution became supersaturated due to the decrease in temperature, which provided the driving force required for crystallization. The crystals of paracetamol were then collected at the end of the OFC. The concentration of paracetamol was measured by two refractometric sensors, placed at the input, point (A), and at the output, point (B), of the OFC system as shown in **Figure 6.8**.

The optical power response of both sensors, acquired during the crystallization process in the OFC, is shown in the inset **Figure 6.9**. The concentration of the process flow was then determined from the previous calibration performed (**Figure 6.3**).

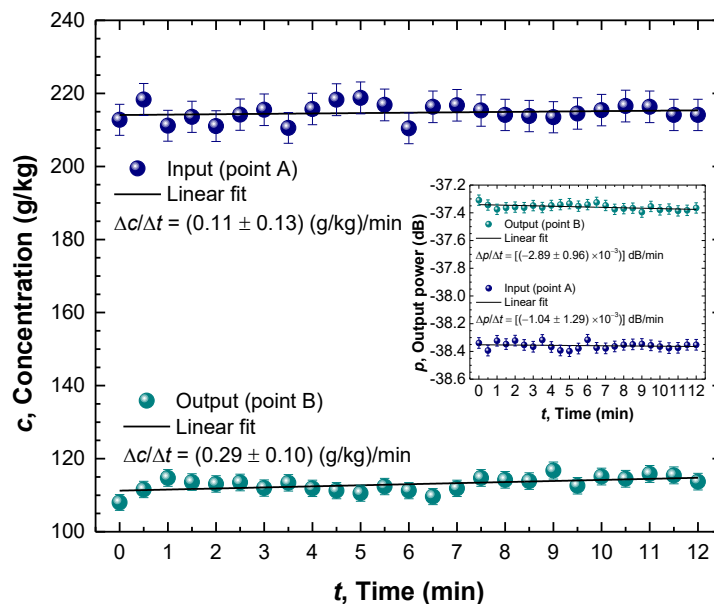


Figure 6.9. Paracetamol concentration during crystallization in the OFC. Inset: Evolution of the optical power of the fiber tip sensor during crystallization.

As expected, the signal of optical power measured by the sensor at the input was lower than that measured by the sensor at the output (inset of **Figure 6.9**). Additionally, the signal remained constant at both locations, suggesting that crystallization occurred under steady-state conditions. At the input (point (A) of OFC, **Figure 6.8**), the concentration of paracetamol fluctuated between 200 and 220 g/kg, when paracetamol was fully dissolved. Then, the solution cooled inside the OFC and became supersaturated. The supersaturation was then gradually consumed as paracetamol crystallizes. At the output (point (B) of OFC, **Figure 6.8**), the concentration fluctuated between 100–120 g/kg, which suggests that the solution reached solubility before leaving the OFC. The results obtained in the OFC agreed with those obtained in the STC as the concentration at the input of the OFC was comparable to the concentration at the beginning in the STC (200–220 g/kg), and the concentration at the output of the OFC was comparable to the concentration at the end in the STC (100–120 g/kg).

These results prove the viability of the portable interrogation system to monitor the concentration of paracetamol in STC-like systems operating in batch or in OFC-like systems operating in continuous. Most previous studies on the crystallization of paracetamol in OFCs have not reported the use of any PAT to monitor the concentration of the process flow [18]. The study of Jiang and

Ni [19] is the exception, but even in this case the concentration of paracetamol had to be measured offline in a High-Performance Liquid Chromatography (HPLC) system, coupled to an Ultraviolet (UV) detector.

6.2.4. Concluding remarks

In this work, a portable interrogation system was used to monitor the concentration of paracetamol in an OFC system in real-time. To measure concentration, a refractometric sensor, based on a small section of a multimode fiber, was used. The sensor was capable of measure optical power as a function of concentration. It was found that the optical power varied linearly with the concentration of paracetamol in the concentration range of 53–261 g/kg. Therefore, the concentration of paracetamol can be obtained directly as a function of optical power without diluting the solution. The refractometric sensor was also used in an STC to calibrate the paracetamol crystallization process.

It was found that this solution allows it to be applied in OFC systems due to the reduced dimensions, allowing them not to disturb the process inside of the crystallizer. The results obtained in this work show the potential of this sensor in monitoring in real-time the concentration of APIs in crystallizers of different sizes and geometries, such as the OFC. This technique can respond to the needs pointed out in this sense, being an alternative to more expensive and complex analysis equipment.

6.3. Monitorization of temperature *in situ*

The FBG is an optical fiber device, modulated in wavelength, commonly used for temperature and strain sensing, with sensitivities of ~ 10 pm/°C and ~ 1.1 pm/ $\mu\epsilon$, respectively [20].

Sensors based on FBG structures have been widely used in a range of industrial and environmental applications. Since these structures can be written in commercial optical fibers, they have all the advantages normally attributed to optical fiber sensors (please, see **Chapter 3**) [21-25].

The FBGs measurand information is typically encoded in the resonant wavelength of the grating structure, which consists of the periodic perturbation of the optical fiber core.

The periodic structure is created by exposing the optical fiber to an interference pattern of UV light or femtosecond radiation [26-28]. The grating structure is characterized by the periodicity of the RI modulation, Λ , and by the effective RI of the waveguide mode, n_{eff} . In this way, the grating corresponds to a wavelength selective mirror, i.e. rejection filter, defined by the Bragg resonance wavelength, λ_B , as **Equation 6.3** suggests [28].

$$\lambda_B = 2n_{eff}\Lambda \quad (6.3)$$

Figure 6.10 represents the FBG principle of operation: light from a broadband source is injected into the optical fiber and only the light within a given very narrow spectral region, centered at the Bragg wavelength, is reflected. The remaining light continues its path, without losses, through the optical fiber. The peak wavelength of the reflected signal is defined by the Bragg resonance wavelength, λ_B , which is dependent on periodicity of the RI modulation, Λ , and by the effective RI of the waveguide mode, n_{eff} (**Equation 6.3**) [28].

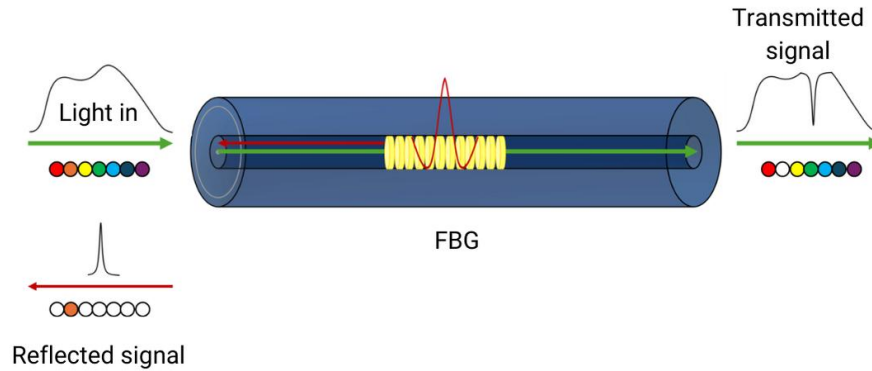


Figure 6.10. Schematic representation of the operation principle of an FBG. Adapted from [27].

In this work, four optical fiber tip sensors, based on low-reflectivity FBG structures, were developed for temperature sensing in an OFC, specifically, in four different channels of OFC. According to the OFC dimensions and geometry, it was thought that fiber tips based on FBG structures could be used to monitor the temperature of the process flow, during crystallization experiments.

6.3.1. Experimental setup

The optical fiber tip sensors fabricated were obtained by cleaving FBGs within their physical length. In this way, the sensing heads consist of 8 mm-length FBG sections that were cleaved in the middle, forming fiber tips with FBGs of 4 mm-length inscribed at their ends (**Figure 6.11**). The cleavage was performed using a cleaver machine (FC-6RS, Sumitomo Electric) to guarantee the perpendicularity at the fiber-ends.

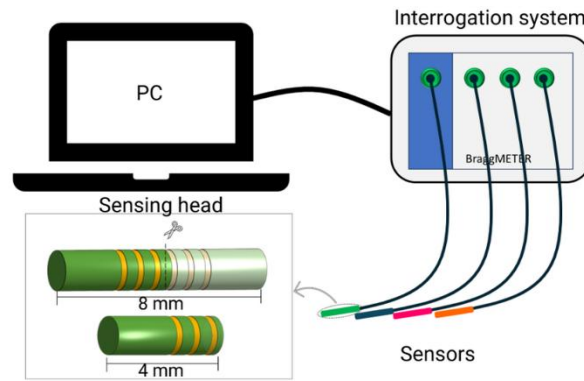


Figure 6.11. Representation of the experimental setup used to monitor the temperature in an OFC.

As it is also illustrated in **Figure 6.11**, the sensors were interrogated in reflection through a portable interrogation system (Bragg METER FS22) and their responses were recorded by a data acquisition software (BraggMONITOR SI/PC).

- **Output spectrum**

Initially, it was performed a spectral characterization of each FBG before and after the cleavage – **Figure 6.12**.

Before the cleavage, for each FBG, it is possible to see a common output spectrum for an FBG. **Figure 6.12** shows that three of the FBGs had a Bragg resonance wavelength, λ_B , equal to 1554 nm and the other one had a λ_B equal to 1562 nm. After the cleavage, the output spectrum of each sensor maintained a maximum power level near to these values (1554 nm and 1562 nm). However, the spectrum signal that is reflected by each optical fiber tip sensor has the overlap of the FBG reflection spectrum combined with its own transmission spectrum, which is reflected at

the tip of the cleaved fiber. Therefore, a Fresnel reflection at the interface fiber-air happens, creating the output spectrum shown in **Figure 6.12 (a to d)**. Regarding the characteristics of FBGs, it is expected that, during temperature variations in the OFC process flow, the response of each sensor shows a wavelength dependence on temperature, which is caused by the thermo-optical effect that changes the effective RI of the measurand material [29].

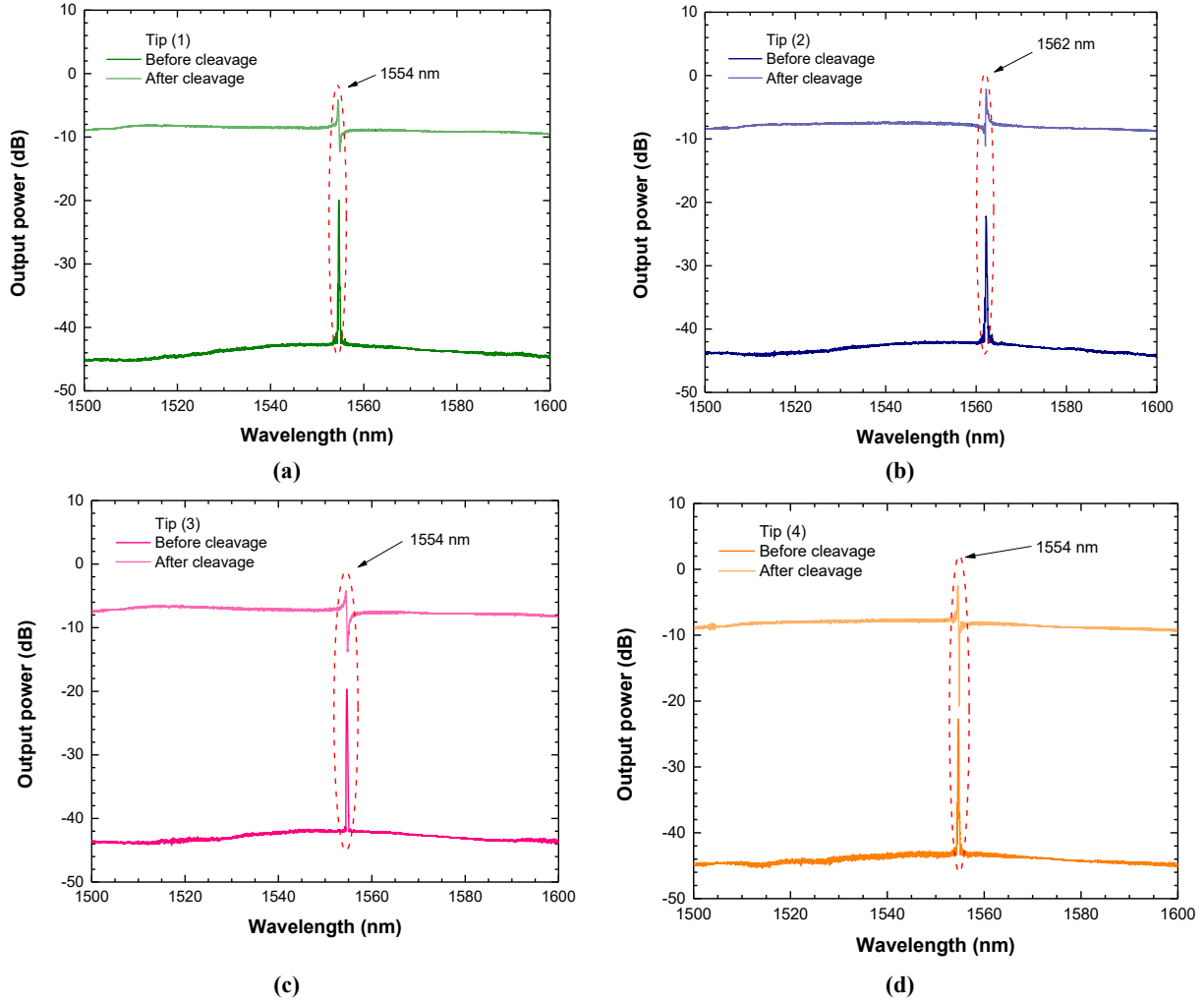


Figure 6.12. Spectral characterization of the optical fiber tip sensors fabricated, before and after the FBG cleavage. (a) Tip (1); (b) Tip (2); (c) Tip (3); (d) Tip (4).

- **Calibration curve and sensitivity**

The influence of temperature in the output spectrum of each sensor was analyzed. For this, each sensing head was immersed in a temperature-controlled water bath ($\sim 10^{\circ}\text{C}$ to 60°C) and the wavelength dependence on temperature was determined, through the sensor's response, acquired

using the experimental setup illustrated in **Figure 6.11**. After each 5°C increase in water bath temperature, the variation of Bragg wavelength as a function of temperature, for each sensing head, was analyzed – **Figure 6.13**.

As expected, for all the sensing heads, a linear approximation of the obtained calibration was carried out, with correlations factors equal to 0.999.

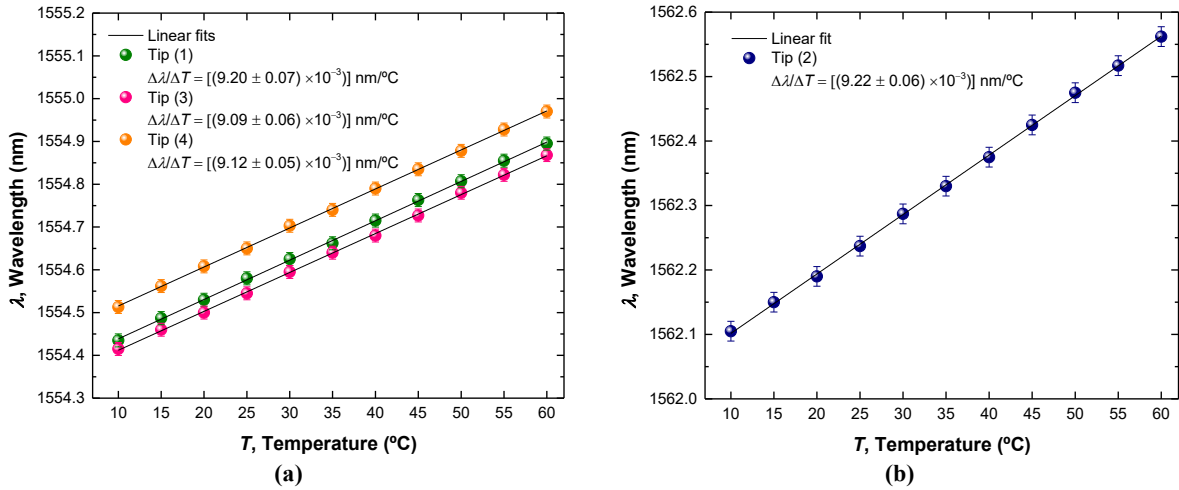


Figure 6.13. Sensor's calibration. Variation of Bragg wavelength as a function of temperature, for each optical fiber tip sensor. (a) Tip (1), Tip (3) and Tip (4); (b) Tip (2).

The data of this approximation are given in **Table 6.5**, as well as the sensitivity of each sensing head/ optical fiber tip sensor to temperature variation. Expected values for FBG sensors were obtained. The temperature sensitivity observed for each sensor is near 10 pm/°C, i.e., the slope values are near to 10 pm/°C.

Table 6.5. Variation of Bragg wavelength as a function of temperature. Linear approximation ($\lambda = mT + b$).

Fiber tip	m	b	R^2
(1)	(9.20×10^{-3})	1554.35	0.999
(2)	(9.22×10^{-3})	1562.01	0.999
(3)	(9.09×10^{-3})	1554.32	0.999
(4)	(9.12×10^{-3})	1554.42	0.999

- Limit of detection**

The smallest value of temperature that the developed sensors can detect, i.e., the LOD, were determined, as explained in **section 6.2.2**. **Table 6.6** shows the variables values used in the

calculations performed, by applying **Equation 6.1**, for each optical fiber tip sensor. It is important to notice that the standard deviation of y-residuals was determined using **Equation 6.2** and the slope of the regression line, for each sensor, was previously presented in **Table 6.5**. A LOD value of $\sim 1^{\circ}\text{C}$ was obtained for each sensor.

Table 6.6. Determination of sensors LOD (values rounded to the nearest hundredth).

Variable	Values for each fiber tip			
	(1)	(2)	(3)	(4)
$\hat{\sigma}$	(3.41×10^{-3})	(2.94×10^{-3})	(3.20×10^{-3})	(2.69×10^{-3})
n	9	9	9	9
b	$(9.20 \times 10^{-3}) \text{ nm}/^{\circ}\text{C}$	$(9.22 \times 10^{-3}) \text{ nm}/^{\circ}\text{C}$	$(9.09 \times 10^{-3}) \text{ nm}/^{\circ}\text{C}$	$(9.12 \times 10^{-3}) \text{ nm}/^{\circ}\text{C}$
LOD	1.11°C	0.96°C	1.05°C	0.88°C

6.3.2. Monitorization of temperature in an OFC

The temperature monitorization was performed in four different channels of the OFC, as is shown in **Figure 6.14**: (1) input, (2) e (3) intermediates and (4) output channels. The sensing heads were vertically immersed in each channel, according to their numeration (please, see **Table 6.4**).

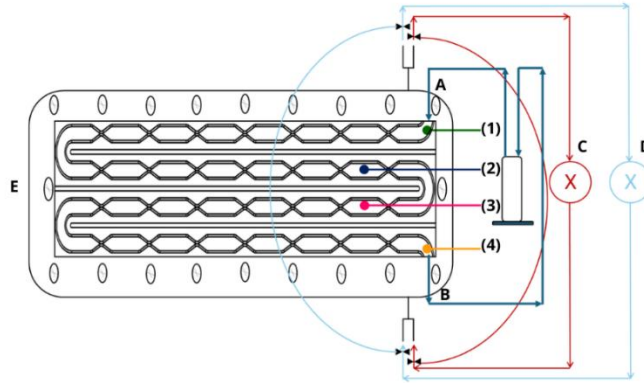


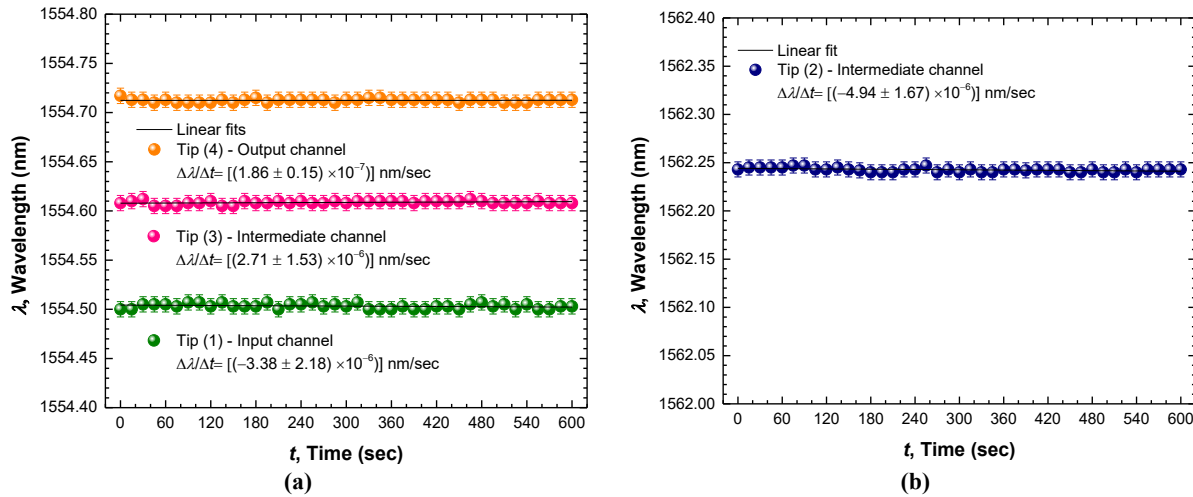
Figure 6.14. Experimental setup for in-situ temperature monitorization in the OFC. (1), (2), (3) and (4)–optical sensors; A–water input; B–water output; C–heating bath; D–cooling bath; E–planar OFC.

The temperature monitorization was performed with the OFC filled with water and under three different conditions: (1) without oscillation and with a flow rate of 28 mL/min; (2) without oscillation and with a flow rate of 58 mL/min; and (3) with oscillation and a flow rate of

58 mL/min. In all these conditions, the water at 15°C was fed into the OFC by a peristaltic pump (BT300-2J, supplied by Longer Pump) and the OFC was thermostated at 35°C. The variations of temperature (from 15°C to 35°C) were ensured by a heating bath, as suggested in **Figure 6.14**. The heating bath circulates in a straight channel, located between the base and middle plates of OFC. During all the monitorizations, the sensors response was acquired using the experimental setup shown in **Figure 6.11** and then, through the previous calibration performed (**Figure 6.13**), the temperature in each OFC channel was determined.

(1) Without oscillation and flow rate of 28 mL/min

The water was fed into the OFC by the peristaltic pump at 28 mL/min and the sensors response was acquired, during the experiment – **Figure 6.15 (a) and (b)**. Through the calibration performed (**Figure 6.13**) it was possible to determine the temperature at each channel of the OFC, as is shown in **Figure 6.15 (c)**.



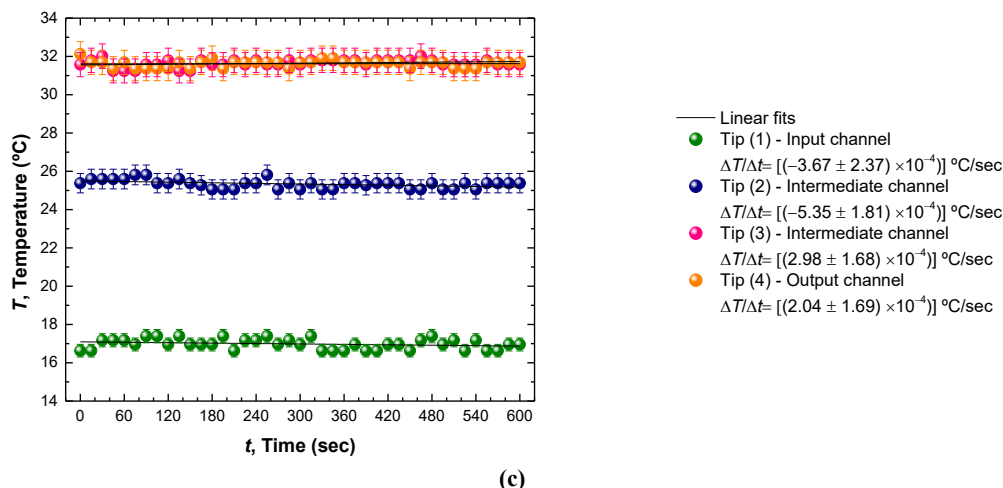


Figure 6.15. Temperature variation inside the OFC when the crystallizer was fed with a flow rate of 28 mL/min and without oscillation. **(a)** Sensors' response at the input, output and second intermediate OFC channels; **(b)** Sensor's response at the first intermediate OFC channel; **(c)** Determination of temperature at all-channels.

The water was fed into the OFC at 15°C and with a flow rate of 28 mL/min. As expected, at the input channel, a temperature value higher than 15°C was obtained (**Figure 6.15 c**), because the residence time at the OFC is enough to promote the heat gain around the input channel. Due to the heat transfer, the water temperature increased to ~17°C.

The heating bath, as previously reported, was thermostated at 35°C. In this way, at the first intermediate channel, a temperature value higher than 15°C and lower than 35°C was expected. At this channel it was observed a temperature value higher than 25°C.

Finally, at the second intermediate channel and at the output channel, it was expected similar temperature values of ~35°C, since the heating bath was thermostated at this value and, according to the OFC geometry, it is expected similar conditions at these two sections. A temperature of ~32°C was observed for these two channels. The difference between the temperature thermostated (35°C) and the observed temperature (32°C) is related with the heat losses between the heating bath and the external environment. In this way, to guarantee that at the output OFC channel a temperature of 35°C is obtained, the heating bath needs to be thermostated at a higher temperature, to compensate for these heat losses.

(2) Without oscillation and flow rate of 58 mL/min

The second experiment was performed at same conditions, however the flow rate was increased to 58 mL/min. The sensors response during the experiment is shown in **Figure 6.16 (a) and (b)** and the corresponding temperature was determined and illustrated in **Figure 6.16 (c)**.

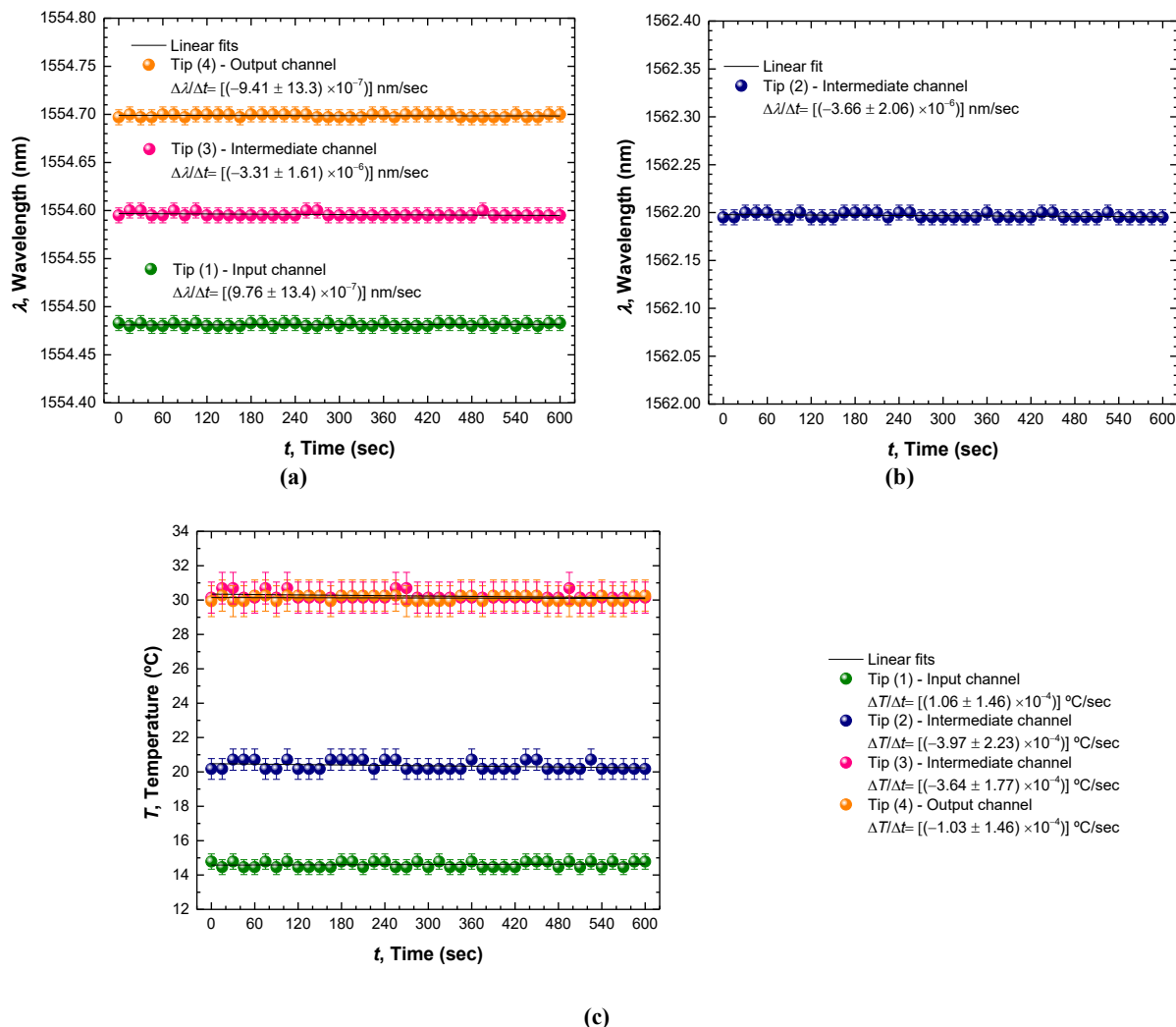


Figure 6.16. Temperature variation inside the OFC when the crystallizer was fed with a flow rate of 58 mL/min and without oscillation. **(a)** Sensors' response at the input, output and second intermediate OFC channels; **(b)** Sensor's response at the first intermediate OFC channel; **(c)** Determination of temperature at all-channels.

As is possible to see in **Figure 6.16 (c)**, the increase in flow rate created a decrease in temperature in all-OFC channels, compared to the previous results (**Figure 6.15 c**). This happened because the flow rate increased from 28 mL/min to 58 mL/min and, in this way, the residence time at the OFC decreased. This led to a lower heat transfer rate and to a lower temperature value, observed at these

OFC channels, maintaining the other conditions (water fed at 15°C and heating bath thermostated at 35°C).

(3) With oscillation and flow rate of 58 mL/min

The last experiment was performed with similar conditions. The flow rate was maintained at 58 mL/min; however, the OFC operating mechanism was set at 4 Hz and 9 mm of frequency and amplitude of oscillation, respectively. The amplitude of oscillation represents an important role in axial dispersion and the frequency is related to the radial dispersion in each OFC compartment. The results obtained during this experiment are shown in **Figure 6.17**.

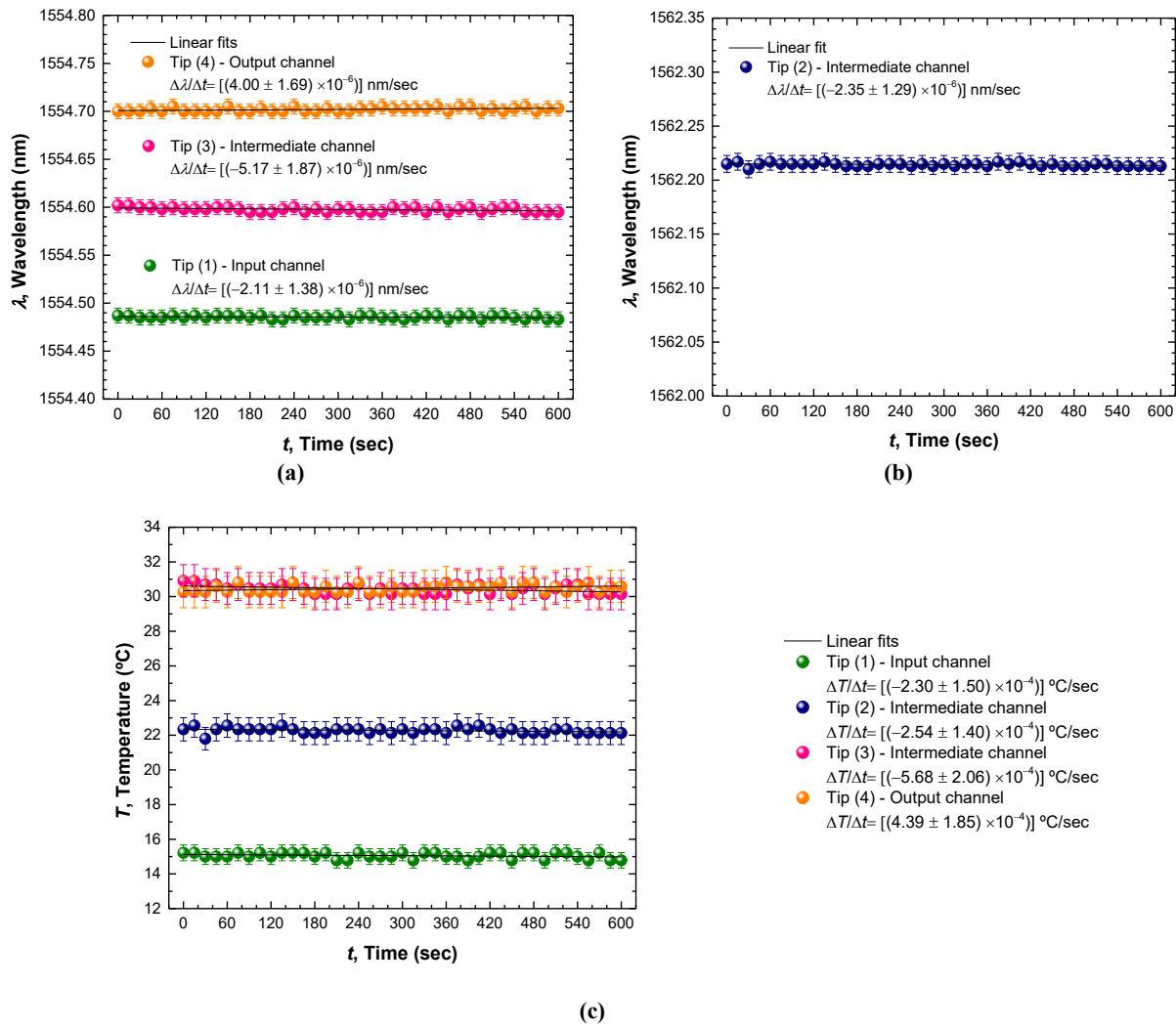


Figure 6.17. Temperature variation inside the OFC when the crystallizer was fed with a flow rate of 58 mL/min and with oscillation. **(a)** Sensors' response at the input, output and second intermediate OFC channels; **(b)** Sensor's response at the first intermediate OFC channel; **(c)** Determination of temperature at all-channels.

Figure 6.17 (a) and (b) show the response of the sensors in each OFC channel. Through the previous calibration performed (**Figure 6.13**) the corresponding temperature was determined. As it is possible to see in **Figure 6.17 (c)** the temperature obtained for each OFC channel is similar to the obtained in the last experiment (**Figure 6.16 c**). The most notorious difference is related to the first intermediate channel. It seems that the oscillation created an increase of temperature in this site of monitoring, from 20°C to 22°C, when compared to the last experiment (performed under the same conditions, however without oscillation – **Figure 6.16 c**). At the second intermediate channel and at the output channel, an increase of ~1°C, when compared to the previous results (**Figure 6.16 c**), was also observed. These results were the expected, since oscillation promoted heat transfer, so the observed temperature at these OFC sites was higher than without oscillation.

6.3.3. Monitorization of temperature in an OFC during a crystallization experiment

In this experiment, the temperature was monitored in two OFC channels, during the paracetamol crystallization process, using two of the developed sensors and the experimental setup presented in **section 6.3.1**. The sensors were placed at the input and output channels of the OFC, as shown in **Figure 6.18**.

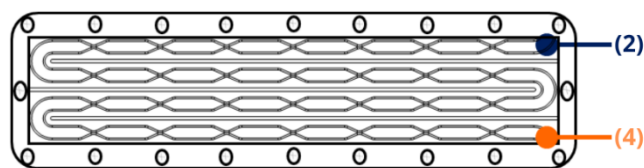


Figure 6.18. Experimental setup for in-situ temperature monitorization in the OFC during paracetamol crystallization process. (2) and (4) represent the optical fiber sensors, placed at input and output OFC channels, respectively.

A 180 g/kg solution of paracetamol in 40%(v/v) ethanol/water at 37.5°C was fed into the OFC by a peristaltic pump at 75 mL/min. The frequency and the amplitude of the OFC oscillation were set at 3 Hz and 9 mm (peak-to-peak in the piston), respectively. The crystallization process was induced by the decrease in temperature, so the cooling bath was thermostated at 30°C.

Table 6.7 summarizes the main characteristics of the sensors used in this monitorization, based on the results present in **section 6.3.1**, where the sensors' performance was characterized.

Table 6.7. Experimental setup for in-situ temperature monitorization in the OFC during paracetamol crystallization process. (2) and (4) represent the optical fiber sensors, placed at input and output OFC channels, respectively.

Fiber tip	OFC channel	Sensitivity	LOD
(2)	Input	(9.22×10^{-3}) nm/°C	0.96°C
(4)	Output	(9.12×10^{-3}) nm/°C	0.88°C

During the monitorization, the sensors response was acquired using the experimental setup shown in **Figure 6.11**. Then, through the previous calibration performed (**Figure 6.13**) for the FBG tip sensors (2) and (4), the temperature at the input and output OFC channels was determined, respectively. **Figure 6.19 (a)** shows the sensors' response used to determine the temperature at each OFC channel – **Figure 6.19 (b)**.

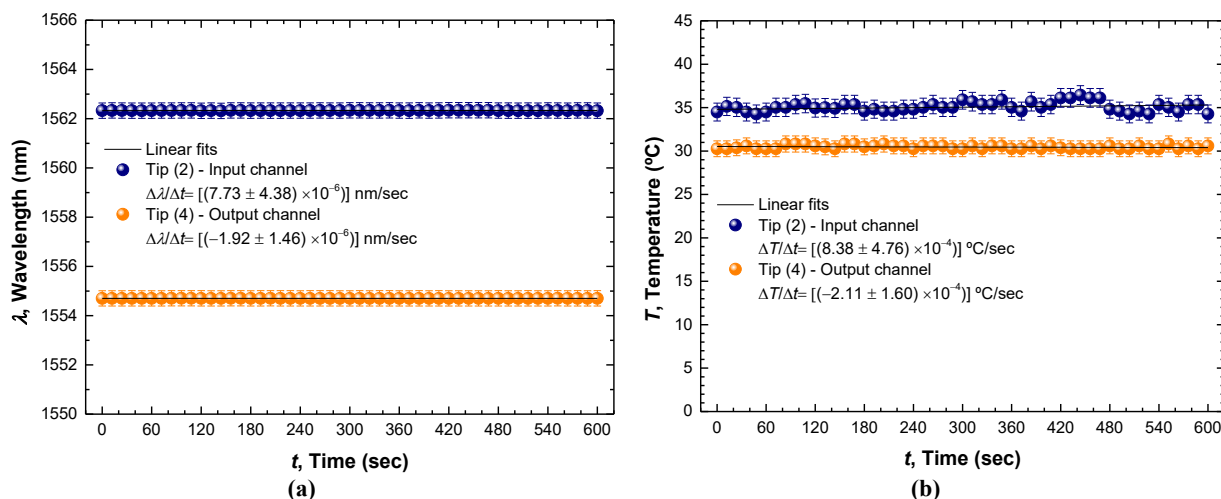


Figure 6.19. Temperature variation inside the OFC during paracetamol crystallization process. **(a)** Sensors' response at the input and output OFC channels; **(b)** Determination of temperature at the input and output OFC channels.

The paracetamol solution was fed into the OFC at 37.5°C and with a flow rate of 75 mL/min. A temperature value lower than 37.5°C was obtained (**Figure 6.19 b**) at the input channel. This value (~35°C) was expected due to the heat transfer to the environment. Since the paracetamol crystallization was promoted by the decrease in temperature, the OFC-plate was thermostated at 30°C and the cooling-bath (please, see **Figure 6.14**) promoted the cooling of paracetamol solution, as it is possible to see in **Figure 6.19 (b)** for the output channel.

6.3.4. Concluding remarks

In this work a portable interrogation system was used to monitor *in-situ* the temperature of process flow in an OFC.

The sensors used correspond to optical fiber sensors, based on FBGs inscribed at the fiber tips ends. The gratings wavelength dependence on temperature allowed to measure the temperature in specific points/channels of the OFC, without disturbing the process flow and independently of the OFC operating settings.

In this way, the technology developed can be applied in OFC systems and other crystallizers with different types of geometries due to the reduced dimensions of the fiber, suppressing the need pointed out in this sense.

6.4. Simultaneous measurements of concentration and temperature in an OFC during a crystallization experiment

As referred in **section 6.3**, FBGs are commonly used for temperature and strain sensing [20]. However, other studies prove that it is possible to create a solution based on this optical device and its technology, to perform RI/concentration measurements in liquid solutions. According to its authors, when an FBG-based fiber tip sensor is immersed in liquid solutions with different RI, the baseline of the FBG, which is the normalized spectrum of the broadband source, varies due to the Fresnel reflection at the cleaved fiber tip-end. Whereas the peak associated with the FBG remains constant, if the samples are measured at the same temperature [14, 30].

In this experiment, the possibility of the sensors used in **section 6.3.3** (FBG-based fiber tip sensors) performing temperature and concentration measurements simultaneously, during paracetamol crystallization, was tested.

After the previous experiments (**sections 6.3.2** and **6.3.3**), the fibers handling caused damage of sensing heads (please, see **Table 6.5**). Only the fiber tip (2) was still able to perform the measurements.

For this reason, the sensor response obtained in **section 6.3.3** for the input channel (**Figure 6.18**), using the fiber tip sensor (2), was used to determine the paracetamol concentration at this OFC channel.

To determine the paracetamol concentration at the output OFC channel, a second cycle of paracetamol crystallization process was performed, under the same conditions. Besides the results provided by two cycles of crystallization, it was expected consistent results, since the adjusted crystallization parameters were equal, and the OFC performance is very stable.

More information and experimental data about the use of the FBG-based fiber tip sensors to perform RI measurements can be found in **Appendix B**.

6.4.1. Calibration curve and sensitivity

Initially, the influence of paracetamol concentration in the output spectrum, specifically in the left side of the FBG peak, for fiber tip sensor (2), was analyzed.

Solutions of paracetamol (CAS, registry number 103-90-02, min. 99% purity, supplied by Sigma-Aldrich) were prepared at room temperature ($\sim 20^\circ\text{C}$) in a solvent mixture of 40% (v/v) ethanol/water. The concentration of the solutions ranged from 102.20 to 183.93 g/kg (g of paracetamol per kg of solvent), corresponding to a RI range of 1.3677 RIU to 1.3733 RIU.

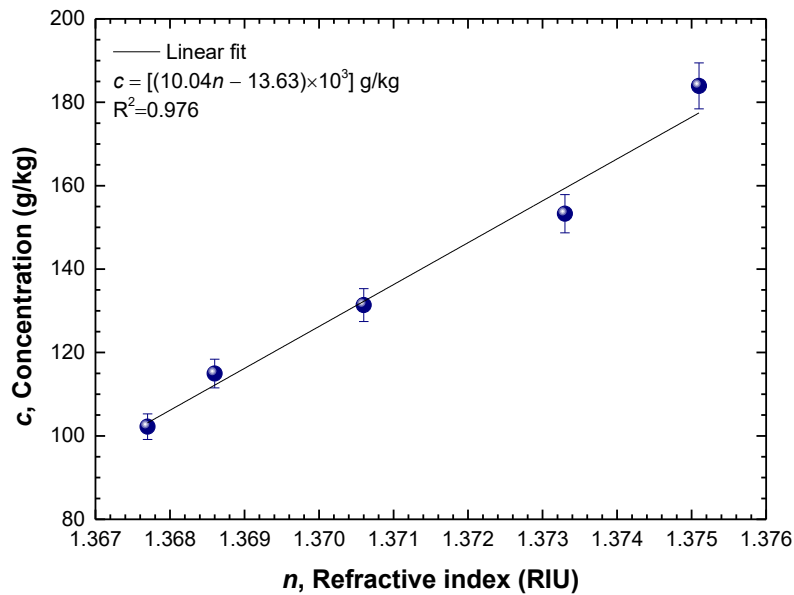


Figure 6.20. Characterization of paracetamol samples. Paracetamol concentration dependence on the refractive index.

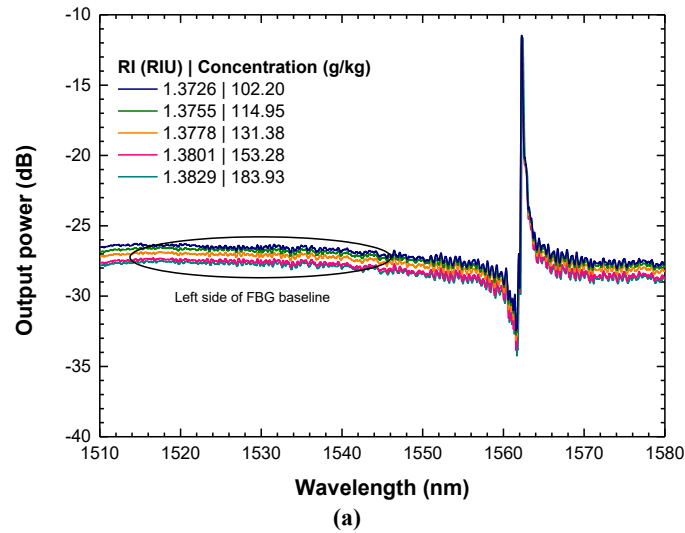
The RI of each solution was measured by an Abbe refractometer (ATAGO, DR-A1).

Figure 6.20 shows the paracetamol concentration dependence on RI. A linear relation was obtained with a correlation factor equal to 0.976. The increase in concentration led to an increase in the optical density of the solutions, which resulted in a higher RI.

After the sample's characterization, each paracetamol sample was measured by the sensing head (2), using the experimental setup shown in **Figure 6.11**.

The sensing head was vertically immersed in each paracetamol sample and through the recorded spectral response (**Figure 6.21 a**) it was possible to determine the dependence of the FBG optical spectrum (left side of the FBG baseline) on RI and paracetamol concentration variations – **Figure 6.21 (b)** and **(c)**, respectively.

The samples were measured, at room temperature, $\sim 20^\circ\text{C}$, by order: from the sample with the lowest concentration to the sample with the highest concentration. After each sample measurement, the sensing head was cleaned with ethanol, to avoid possible contamination. The left side of the FBG baseline is identified in **Figure 6.21 (a)** and a measuring wavelength of 1520 nm was considered during the experiment.



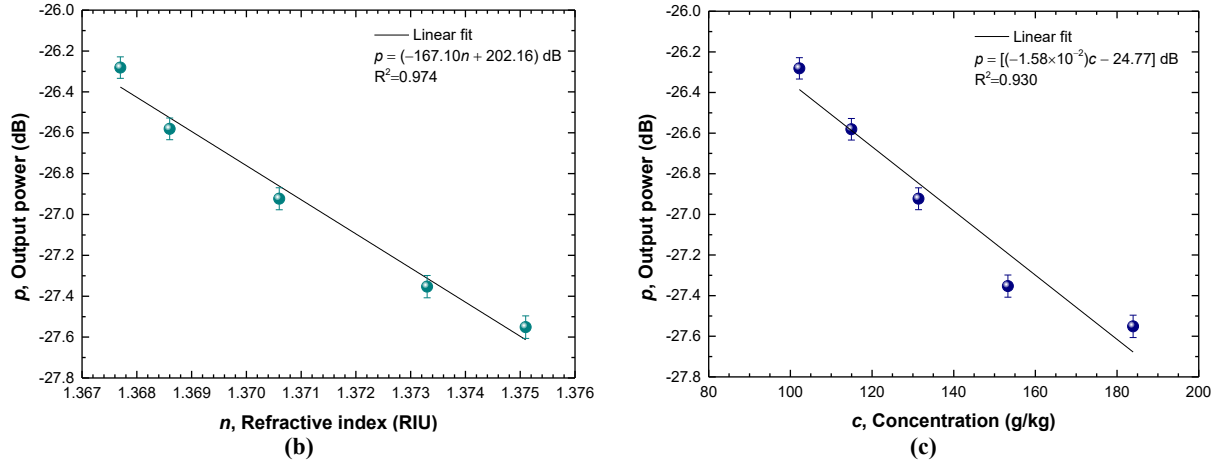


Figure 6.21. Sensor calibration. (a) Output spectrum for each paracetamol sample measured; (b) Sensor calibration to paracetamol refractive index; (c) Sensor calibration to paracetamol concentration variations.

The optical power response of the sensor, at a measuring wavelength of ~ 1520 nm (left side of FBG baseline), demonstrated a linear dependence, according to the samples RI/concentration – **Figure 6.21 (b) and (c)**, respectively. A linear sensitivity to paracetamol RI variation of $(-167.10 \pm 13.54) \text{ dB/RIU}$, which corresponds to a concentration sensitivity of $(-15.80 \pm 2.15) \text{ dB/(g/g)}$, was obtained.

This calibration (**Figure 6.21 c**) allowed the monitorization of paracetamol concentration during the crystallization process.

In relation to temperature, the optical fiber tip sensor (2) presented a linear sensitivity of $9.22 \text{ pm/}^\circ\text{C}$, as reported in **section 6.3.1**.

- **Cross-sensitivity**

The developed sensor was sensitive to temperature and concentration/RI variations. For this reason, the influence of temperature on concentration measurements was analyzed, i.e., the cross-sensitivity was studied.

In this case, the cross-sensitivity, S_{cross} , was calculated through **Equation 6.4** [31]:

$$S_{cross} = m_T/m_C \quad (6.4)$$

Where, m_T is the slope of temperature calibration (variation of sensor response, with the variation of temperature, while the concentration is kept constant), and m_c is the slope of concentration calibration (variation of sensor response, with the variation of concentration, while the temperature is kept constant).

The m_c value is equal to the optical fiber tip sensor (2) sensitivity, (-15.80 ± 2.15) dB/(g/g), determined in **section 6.4.1**, **Figure 6.21 (b)**, where samples of paracetamol, with different concentration values, were measured by the sensor at room temperature ($\sim 20^\circ\text{C}$).

To determine the value of m_T , the optical power response of sensor to variations of temperature, keeping the concentration constant, was analyzed. The optical spectra obtained for optical fiber sensor tip (2) was analyzed, when the calibration present in **section 6.3.1** was performed. In the mentioned section, the sensor was used to measure water at different temperatures, i.e., there was a temperature variation, while the concentration was kept constant.

Figure 6.22 shows the sensor's optical power response to the variations of temperature, at measuring wavelength of 1520 nm (left side of FBG baseline).

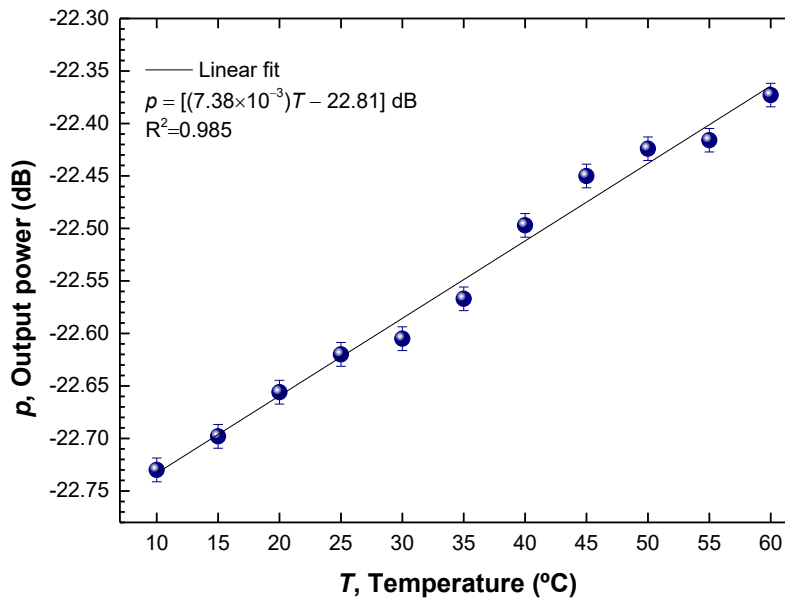


Figure 6.22. Sensor calibration. Optical power sensor responses to the variation of temperature, at a measuring wavelength of 1520 nm.

A linear dependence of optical power to the variation of temperature was detected (correlation factor of 0.985). In this way, the value of m_T is $[(7.38 \pm 0.29) \times 10^{-3}]$ dB/°C.

Applying **Equation 6.4**, a cross-sensitivity value of (-4.67×10^{-4}) °C/(g/g) was obtained. The definition of cross-sensitivity varies according to the context and sensor application [31]. In relation to the present sensor and its application, a cross-sensitivity below 0.001°C is considered a lower value, i.e., the effect of temperature in concentration measurements, using the developed sensor, can be ignored. The results revealed that an increase of 1°C creates a diminution of (4.67×10^{-4}) g/g units in the concentration measurements. It is important to notice that the sensor in question was fabricated to be implemented inside the OFC channels and, at each OFC channel, the temperature during the crystallization process remains constant (**section 6.3.2**).

- **Limit of detection**

In terms of concentration, the sensor LOD was determined as explained in **section 6.2.2**.

Table 6.8 shows the variables values used in the calculations performed, by applying **Equation 6.1**. The standard deviation of y-residuals was determined using **Equation 6.2** and the slope of the regression line was shown in **Figure 6.21 (c)**.

Table 6.8. Determination of FBG-based optical fiber tip sensor LOD (values rounded to the nearest hundredth).

Variable	Value
$\hat{\sigma}$	0.14
n	5
b	(-15.80) dB/(g/g)
LOD	0.03 (g/g)

For fiber tip sensor (2), a LOD value of ~0.03 g/g, in relation to concentration, was obtained. Regarding temperature, the value of sensor LOD is 0.96°C, as shown in **section 6.3.1**.

- **Resolution**

The resolution of the FBG-based optical fiber tip sensor was determined using the method shown in **Chapter 4, section 4.3.1**. The sensing head was consecutive immersed in two paracetamol samples, with two consecutive values of concentration, namely, 102.20 g/kg and 114.95 g/kg. The sensor output power response obtained during these measurements, at a measuring wavelength of ~1520 nm, is shown in **Figure 6.23**.

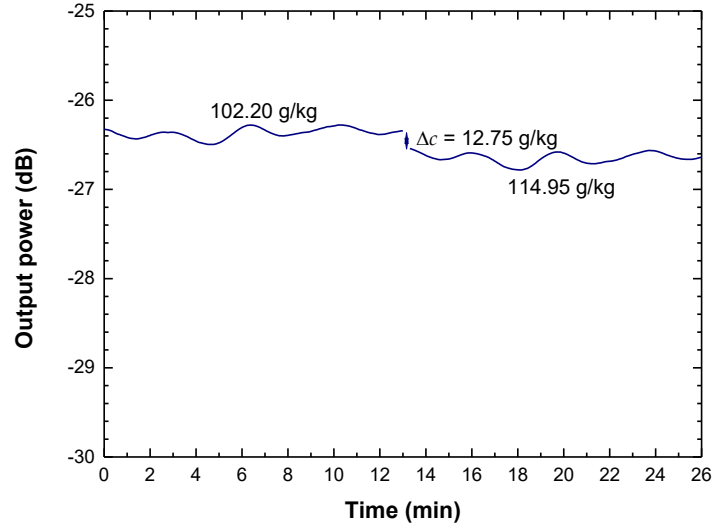


Figure 6.23. Resolution of the FBG-based optical fiber tip sensor.

Then, the minimum value of concentration (δ_c) that the sensor could discriminate was determined through the previous response (**Figure 6.23**) and applying **Equation 4.2** of **Chapter 4** [17].

A resolution of (8.46×10^{-3}) g/g was obtained. **Table 6.9** indicates the variable used in this calculation.

Table 6.9. Determination of sensor resolution (values rounded to the nearest hundredth).

Variable	Unit	Value
σ_p	dB	(9.95×10^{-2})
Δc	(g/kg)	12.75
ΔP	dB	(3.00×10^{-1})
Resolution	(g/g)	(8.46×10^{-3})

6.4.2. Monitorization of concentration in an OFC during a crystallization experiment

As previously reported in **section 6.4**, two cycles of crystallization were performed to test the capability of fiber tip sensor (2) to perform measurements of temperature and concentration simultaneously. The first crystallization cycle is the presented in **section 6.3.3**, where the fiber tip sensor (2) was implemented at the input OFC channel. The second crystallization cycle took place under the same conditions; however, the fiber tip sensor (2) was implemented at the output OFC

channel. In this way, a 180 g/kg solution of paracetamol in 40%(v/v) ethanol/water at 37.5°C was fed into the OFC at 75 mL/min. The frequency and the amplitude of the OFC oscillation were set at 3 Hz and 9 mm, respectively. The cooling bath was thermostated at 30°C, since the crystallization was induced by cooling.

As shown in **Figure 6.19 (b)**, during the first crystallization cycle, at the input OFC channel was obtained a temperature of ~35°C. In relation to concentration, **Figure 6.24 (a)** shows the optical power dependence of the output spectrum of optical fiber tip sensor (2), at a measuring wavelength of 1520 nm (left side of FBG baseline), during the crystallization process. Using the calibration performed, shown in **Figure 6.21 (c)**, the variation of paracetamol concentration at the input OFC channel was determined – **Figure 6.24 (b)**.

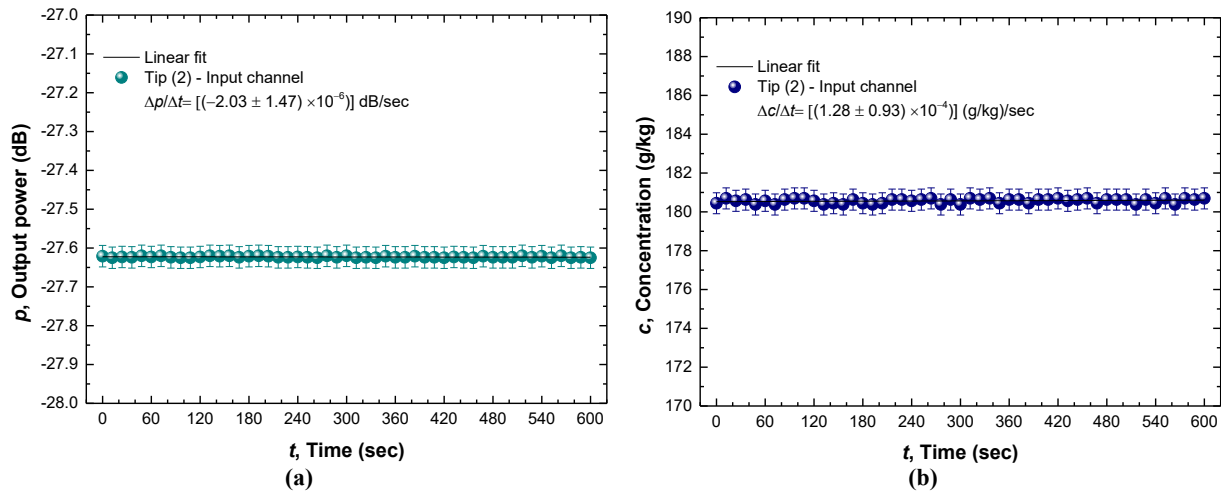


Figure 6.24. Variation of concentration at the input OFC channel during the first cycle of paracetamol crystallization process. (a) Sensor's response at the input OFC channel; (b) Determination of concentration at the input OFC channel.

During the second cycle of crystallization, the optical fiber tip sensor (2) was implemented at the output channel. The temperature at this channel was also determined through the sensor response. **Figure 6.25 (a)** shows the sensors' response, in relation to temperature (wavelength dependence), used to determine the temperature at the output OFC channel. For this, the calibration shown in **Figure 6.13 (b)** for optical fiber tip sensor (2) was used. The temperature result for this OFC channel is represented in **Figure 6.25 (b)**.

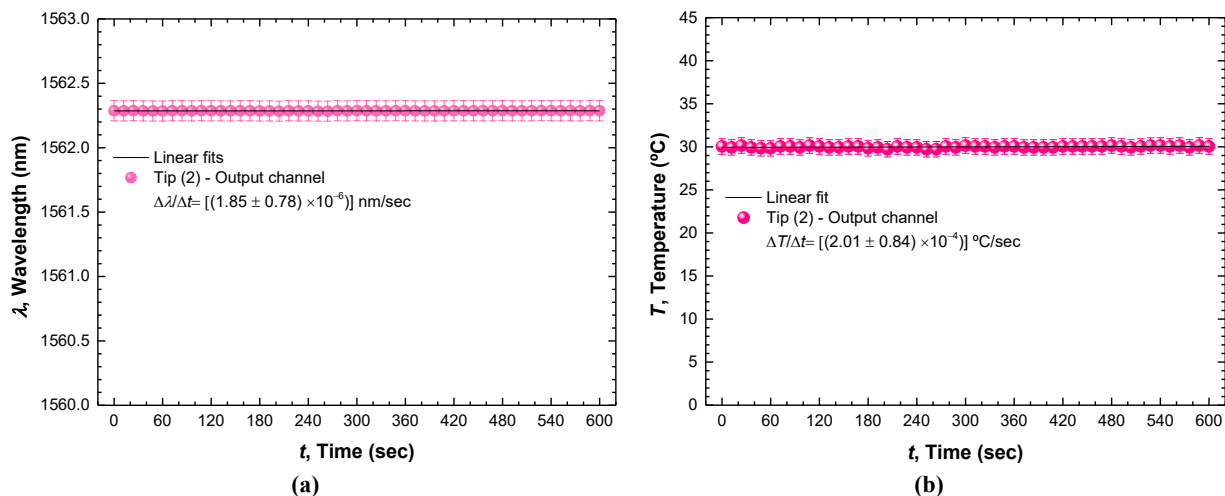


Figure 6.25. Temperature variation at the output OFC channel during the second cycle of paracetamol crystallization process. **(a)** Sensor's response at the input OFC channel; **(b)** Determination of temperature at the input OFC channel.

During the second cycle of crystallization, a temperature value was obtained at the output channel, close to the temperature value measured at the first crystallization cycle (**Figure 6.19 b**), for the same OFC channel. Since the crystallization conditions between cycles were kept, similar results were expected between the two cycles, as well as a temperature value at the OFC channel close to 30°C (the OFC-plate was thermostated at this temperature, 30°C) – **Figure 6.26 (b)**.

In relation to the concentration at the output OFC channel, the sensor response at a measuring wavelength of 1520 nm (left side of FBG baseline) was also analyzed – **Figure 6.26 (a)**. After that, and through the calibration previously performed (**Figure 6.20**), the paracetamol concentration at this OFC channel, i.e., the concentration at the end of crystallization process, was determined – **Figure 6.26 (b)**.

The results revealed that the signal of optical power measured at 1520 nm by the sensor at the input was lower than that measured by the sensor at the output – **Figure 6.25 (a)** and **Figure 6.26 (a)**, respectively. At both locations signal, the signal was constant, proving the steady state of two crystallization cycles. At the input OFC channel, **Figure 6.25 (b)**, the concentration of paracetamol was ~180 g/kg, which was expected, since this is the concentration of the initially supersaturated solution. Gradually, the supersaturation was consumed as paracetamol crystallizes. At the output OFC channel, **Figure 6.26 (b)**, the concentration measured was ~86 g/kg, suggesting that the solution reached solubility before leaving the OFC.

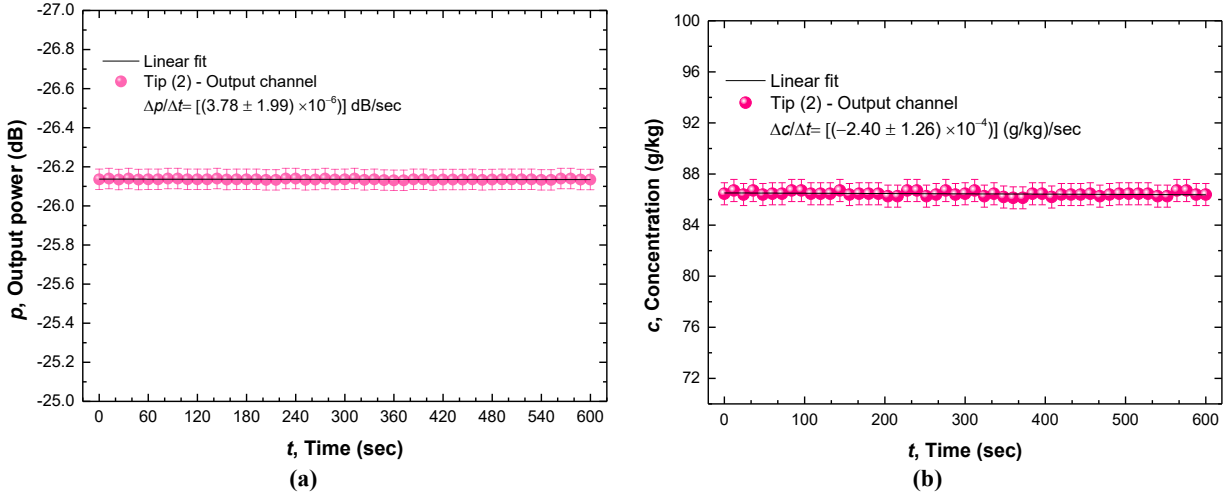


Figure 6.26. Variation of concentration at the output OFC channel during the second cycle of paracetamol crystallization process. **(a)** Sensor's response at the output OFC channel; **(b)** Determination of concentration at the output OFC channel.

6.4.3. Concluding remarks

Considering that the two paracetamol crystallization cycles are equivalent, since they were performed at the same conditions, and according to optical fiber tip (2), at the input OFC channel, the process flow had a concentration of ~ 180 g/kg and it was at $\sim 35^\circ\text{C}$.

On the other hand, at the output OFC channel, the concentration of process flow reached temperatures of $\sim 30^\circ\text{C}$ and a concentration value of ~ 86 g/kg – **Figure 6.27**.

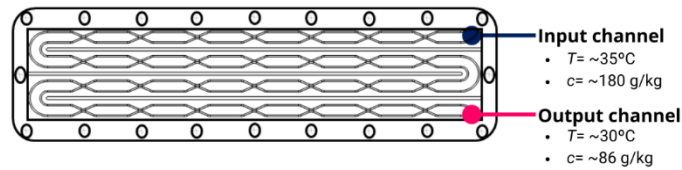


Figure 6.27. Schematic representation of the monitoring of paracetamol crystallization in the OFC: monitoring of temperature and concentration, simultaneously, at the input and output OFC channels.

These results are as expected. Initially, at the input channel, and for crystallization occurs, the solution in circulation must be highly concentrated (supersaturated). The paracetamol needs to be totally dissolved. Then, at the end of crystallization process, when the solution in circulation reaches the output channel, it is expected lower values of concentration. The paracetamol present in solution is lower, since the paracetamol crystals are already formed.

In relation to temperature, initially (input channel), the temperature must be higher to promote the total dissolution of paracetamol. This temperature, along with the OFC geometry, decreases, since the crystallization is induced by cooling.

These results proved to be very promising. A simple sensing head geometry based on an FBG tip was developed. The sensing head results in an FBG cleaved in the middle, forming an optical fiber tip. Besides temperature measurements, it was also found that this sensor can be used in RI/concentration sensing.

Due to its reduced dimensions and simplicity, this sensor may find applications in chemical and biological sensing fields. Specifically, it can be implemented to control and monitor the process flow of OFC, during crystallization process, providing readings of temperature and concentration, in simultaneously, with great sensitivity and stability.

6.5. Final chapter remarks

The scientific and technological advancement in pharmaceutical industry has led to the development of new geometries of crystallizers, such as the OFC. However, the technology available for the control of crystallization in these new geometries of crystallizers is still limited, expensive and incompatible with their configurations and dimensions. Crystallizers such as OFC have small vessels with channels with a diameter smaller than the diameter of the probes, which avoids the implementation of these tools and makes it impossible to monitor the process parameters during crystallization, in real-time. Concentration and temperature of the process flow are two of these process parameters that need to be controlled.

In this chapter, the development of a fiber optic–based technology sensitive to the parameters of interest (concentration and temperature) is described. Due to the dimensions of a standard optical fiber, the consolidation of the developed technology allowed the monitoring of these process parameters in real-time, by immersing the fabricated optical fiber sensors in the OFC process flow, without changing it, in a simple and easy way.

It is considered that all the work developed will contribute to greater knowledge and control of the crystallization process, regardless of the crystallizer geometry.

In addition to the strong applicability in the pharmaceutical area, the technology developed may also have applicability in several areas, with the aim of monitoring chemical, biological and biochemical processes.

References

- [1] D. Zhang, S. Xu, S. Du, J. Wang, and J. Gong, “Progress of Pharmaceutical Continuous Crystallization”, *Engineering*, vol.3, n°3, pp.54–364, June 2017, DOI:10.1016/J.ENG.2017.03.023.
- [2] L. L. Simon, H. Pataki, G. Marosi, F. Meemken, K. Hungerbühler, A. Baiker, S. Tummala, B. Glennon, M. Kuentz, G. Steele, H. J. M. Kramer, J. W. Rydzak, Z. Chen, J. Morris, F. Kjell, R. Singh, R. Gani, K. V. Gernaey, M. Louhi-Kultanen, J. O'Reilly, N. Sandler, O. Antikainen, J. Yliruusi, P. Froberg, J. Ulrich, R.D. Braatz, T. Leyssens, M. von Stosch, R. Oliveira, R.B.H. Tan, H. Wu, M. Khan, D. O'Grady, A. Pandey, R. Westra, E. Delle-Case, D. Pape, D. Angelosante, Y. Maret, O. Steiger, M. Lenner, K. Abbou-Oucherif, Z. K. Nagy, J. D. Litster, V. K. Kamaraju, and M.-S. Chiu, “Assessment of Recent Process Analytical Technology (PAT) Trends: A Multiauthor Review”, *Org. Process Res. Dev.*, vol.19, n°1, pp.3–62, Jan. 2015, DOI:10.1021/op500261y.
- [3] L. Yu, R. Lionberger, A. Raw, R. D'Costa, H. Wu, and A. Hussain, “Applications of process analytical technology to crystallization processes”, *Adv. Drug Deliv. Rev.*, vol.56, n°3, pp.349–369, Feb. 2004, DOI:10.1016/j.addr.2003.10.012.
- [4] T. McGlone, N. E. B. Briggs, C. A. Clark, C. J. Brown, J. Sefcik, and A. J. Florence, “Oscillatory flow reactors (OFRs) for continuous manufacturing and crystallization”, *Org. Process Res. Dev.*, vol.19, n°9, pp.1186–1202, Aug. 2015, DOI:10.1021/acs.oprd.5b00225.
- [5] M. W. Hermanto, G. He, M. Tjahjono, P. S. Chow, R. B. H. Tan, and M. Garland, “Calibration of dielectric constant measurements to improve the detection of cloud and clear points in solution crystallization”, *Chem. Eng. Res. Des.*, vol.89, n°12, pp.2613–2619, Dec. 2011, DOI:10.1016/j.cherd.2011.04.012.
- [6] J. Worlitschek, and M. Mazzotti, “Model-Based Optimization of Particle Size Distribution in Batch-Cooling Crystallization of Paracetamol”, *Cryst. Growth Des.*, vol.4, n°5, pp.891–903, Feb. 2004, DOI:10.1021/cg034179b.

-
- [7] D. J. Griffin, Y. Kawajiri, R. W. Rousseau, and M. A. Grover, "Using MC plots for control of paracetamol crystallization", *Chem. Eng. Sci.*, vol.164, pp.344–360, June 2017, DOI:10.1016/j.ces.2017.01.065.
- [8] K. A. Powell, A. N. Saleemi, C. D. Rielly, and Z. K. Nagy, "Monitoring Continuous Crystallization of Paracetamol in the Presence of an Additive Using an Integrated PAT Array and Multivariate Methods", *Org. Process Res. Dev.*, vol.20, n°3, pp.626–636, Jan. 2016, DOI:10.1021/acs.oprd.5b00373.
- [9] L. Helmdach, M. P. Feth, C. Minnich, and J. Ulrich, "Application of ATR-MIR spectroscopy in the pilot plant—Scope and limitations using the example of Paracetamol crystallizations", *Chem. Eng. Process. Process Intensif.*, vol.70, pp.184–197, Aug. 2013, DOI:10.1016/j.cep.2013.04.003.
- [10] I. -C. Wang, M. -J. Lee, D. -Y. Seo, H. -E. Lee, Y. Choi, W. -S. Kim, C. -S. Kim, M. -Y. Jeong, and G. J. Choi, "Polymorph Transformation in Paracetamol Monitored by In-line NIR Spectroscopy During a Cooling Crystallization Process," *AAPS PharmSciTech.*, vol.12, n°2, pp.764–770, June 2011, DOI:10.1208/s12249-011-9642-x.
- [11] K. P. Guiry, J. M. Kelleher, S. E. Lawrence, M. T. McAuliffe, H. A. Moynihan, and A. L. Ryan, "Crystal polymorphism of pharmaceuticals: probing crystal nucleation at the molecular level", *J Enzyme Inhib Med Chem.*, vol.22, n°5, pp.550-555, Oct. 2007, DOI: 10.1080/14756360701425147.
- [12] A. G. Shtukenberg, M. Tan, L. Vogt-Maranto, E. J. Chan, W. Xu, Y. Jingxiang, M. E. Tuckerman, C. T. Hu, and B. Kahr, "Melt Crystallization for Paracetamol Polymorphism", *Cryst. Growth Des.*, vol.19, n°7, pp.4070-4080, June 2019, DOI:10.1021/acs.cgd.9b00473.
- [13] M. Rassat, I. Ouandji, N. Guiblin, and P. Espeau, "Obtaining two polymorphic forms of paracetamol within the phase diagram with PEG 1500", *Eur. J. Pharm. Biopharm.*, vol.195, 114173, Feb. 2024, DOI:10.1016/j.ejpb.2023.114173.
- [14] E. Hecht, *Optics*, 5th ed., Pearson: London, UK, 2015.
- [15] A. Shrivastava, and V. Gupta, "Methods for the determination of limit of detection and limit of quantitation of the analytical methods", *Chron. Young Sci.*, vol.2, n°1, pp.21-25, Jan.-Mar. 2011, DOI:10.4103/2229-5186.79345.
- [16] Y. Yang, L. Sun, and C. Guo, "Aero-Material Consumption Prediction Based on Linear Regression Model", In *Proceedings of the 8th International Congress of Information and*

-
- Communication Technology*, vol.131, pp.825-831, Jan. 2018, Xiamen, China. DOI:10.1016/j.procs.2018.04.271.
- [17] S. Novais, M. S. Ferreira, and J. L. Pinto, "Relative humidity fiber sensor based on multi-mode interferometer coated with agarose-gel", *Coatings*, vol.8, n°12, 453, Dec. 2018, DOI:10.3390/coatings8120453.
- [18] F. Ferreira, J. A. Teixeira, F. Castro, "Modular Oscillatory Flow Plate Reactor". Patent PT 109314 H (2016); PCT/IB2017/052005 (2017); US 16/092,010, EP3439773 (2018).
- [19] P. Cruz, F. Rocha, and A. Ferreira, "Determination of the critical mixing intensity for secondary nucleation of paracetamol in an oscillatory flow crystallizer", *CrystEngComm.*, vol.20, pp.829–836, Jan. 2018, DOI:10.1039/C7CE01940H.
- [20] M. Jiang, and X. -W. Ni, "Reactive Crystallization of Paracetamol in a Continuous Oscillatory Baffled Reactor", *Org. Process Res. Dev.*, vol.23, n°5, pp.882–890, Mar. 2019, DOI:10.1021/acs.oprd.8b00446.
- [21] R. Correia, R. Sinha, A. Norris, S. Korposh, S. Talbot, F. U. Hernandez, and S. P. Morgan, "Optical fiber sensing at the interface between tissue and medical device". In *Proceedings of the International Conference on Biophotonics V*, 103400X, Apr. 2017, Perth, Australia. DOI:10.1117/12.2269811.
- [22] S. Silvestri, and E. Schena, "Optical-Fiber Measurement Systems". In *Optoelectronics: Devices and Applications*, P. Predeep, Ed. Rijeka, Croatia: InTech, pp.205–224, 2011.
- [23] S. Silva, P. Roriz, and O. Frazão, "Refractive Index Measurement of Liquids Based on Microstructured Optical Fibers", *Photonics*, vol.1, n°4, pp.516-529, Dec. 2014, DOI:10.3390/photonics1040516.
- [24] R. Y. Shah, and Y. K. Agrawal, "Introduction to fiber optics: Sensor for biomedical applications", *Indian J. Pharm. Sci.*, vol.73, n°1, pp.17-22, Jan. 2011, DOI:10.4103/0250-474X.89752.
- [25] R. Kashyap, *Fiber Brags Grating*, 2nd ed., Academic, Optics and Photonics Series: San Diego, CA, 2010.
- [26] C. Massaroni, M. A. Caponero, R. D'Amato, D. Lo Presti, and E. Schena, E., "Fiber Brag Grating measuring system for simultaneous monitoring of temperature and humidity in mechanical ventilation", *Sensors*, vol.17, n°4, 749, Apr. 2017, DOI:10.3390/s17040749.

-
- [27] R. Correia, S. James, S. -W. Lee, S. P. Morgan, and S. Korposh, "Biomedical applications of optical fiber sensors", *J. Opt.*, vol.20, n°7, pp.1-25, June 2018, DOI:10.1088/2040-8986/aac68d.
- [28] J. Du, and Z. He, "Sensitivity enhanced strain and temperature measurements based on FBG and frequency chirp magnification", *Opt. Express*, vol.21, n°22, pp.27111-27118, Nov. 2013, DOI:10.1364/OE.21.027111.
- [29] A. D. Kersey, M. A. Davis, H. J. Patrick, M. LeBlanc, K. P. Koo, C. G. Askins, M. A. Putnam, and E. J. Friebele, "Fiber grating sensors", *J. Lightwave Technol.*, vol.15, n°8, pp.1442–1463, Aug. 1997, DOI:10.1109/50.618377.
- [30] H. Meng, W. Shen, G. Zhang, C. Tan, and X. Huang, "Fiber Bragg grating-based fiber sensor for simultaneous measurement of refractive index and temperature", *Sens. Actuators B: Chem.*, vol.150, n°1, pp.226-229, Sept. 2010, DOI:10.1016/j.snb.2010.07.010.
- [31] T. Jiao, H. Meng, S. Deng, S. Liu, X. Wang, Z. Wei, F. Wang, C. Tan, and X. Huang, "Simultaneous measurement of refractive index and temperature using a Mach-Zehnder interferometer with forward core-cladding-core recoupling", *Opt. Laser Technol.*, vol.111, pp.612–615, Apr. 2019, DOI: 10.1016/j.optlastec.2018.10.047.

Chapter 7. Conclusions and future work

The work developed during the PhD program had the main goal of developing optical fiber sensors capable of controlling and monitoring the crystallization process, regardless of the crystallizer geometry used. The following paragraphs summarize all the accomplishments acquired during all the research and development activities.

Crystallization is one of the oldest separation and purification unit operations used in several manufacturing industries, specially used in the pharmaceutical industry. One of the main concerns of pharmaceutical industry is to develop technology capable of optimizing its production from the point of view of the consumption of reagents and solvents. For this, the rigorous control of some process parameters during the crystallization process is fundamental. Concentration and temperature are two of the most important parameters to be controlled to ensure the quality of the final product.

In an initial phase, the concepts related to the Crystallization process and the use of optical fiber as a sensing technology were studied and analyzed, as presented in **Chapter 2** and **Chapter 3**.

In **Chapter 4** the potential of optical fiber tips to perform refractive index and, consequently, concentration measurements, was shown. An optical fiber sensor based on a GI-MMF tip was fabricated to measure samples with different concentration values and to detect the different phases of paracetamol crystallization process, in a non-invasive and non-destructive way.

Besides the optical fiber sensor geometry, different interrogation systems were developed and tested, as shown in **Chapter 5**. The use of fiber optic laser technology was tested, and two different laser cavities configurations, ring and linear, were fabricated. Both configurations were able to perform concentration measurements, however only the linear ones reached the laser condition and allowed the measurement of paracetamol concentration with higher sensitivity and resolution.

The *in-situ* implementation of the developed technology required the use of an idealized portable interrogation system. All the procedures were described in **Chapter 6**. Initially, the MMF fiber tip sensor, presented in **Chapter 4**, was used to monitor the optical concentration of paracetamol at a planar-OFC, operating in continuous, during the crystallization process. A similar monitorization, however in a batch operation, was performed, using the same paracetamol supersaturated solution.

The concordance obtained in both monitorization allowed to test the repeatability of the sensor as well as its viability. Another optical fiber tip sensor configuration was fabricated to monitor the temperature variations during the paracetamol crystallization process at a planar-OFC. The fiber tip consists of an FBG structure cleaved in the middle and forming an optical fiber tip. The temperature monitorization was performed at different OFC channels without interfering with the process flow.

The main discovery found about this sensing structure, the optical fiber-based FBG tip, is its capability of performed temperature and concentration measurements simultaneously, with a lower cross-sensitivity. In this way, using the same sensing structure it was possible to monitor the concentration and temperature of process flow, during the paracetamol crystallization process at the planar-OFC, with great sensitivity and resolution, when compared with the performance observed for MMF fiber tip sensor (concentration measurements).

In view of these results and recognizing the difficulty of creating suitable crystallization systems that ensure profitability and maximum use of compounds, it is stated that the technology presented, applied to OFC, could be of added value to the pharmaceutical industry.

The planar-OFC, due to its characteristics and geometry, has been widely explored by industry, regarding the continuous crystallization of APIs. Thus, the use of the fabricated optical fiber tip sensors, with low implementation cost and compatible with the OFC geometry, can contribute to maximizing this profitability, ensuring greater use of compounds and avoiding the use of other more expensive analytical equipment, such as ATR-probes.

Despite the obvious potential of this technology, it is essential to highlight that the entire project still presents several opportunities for improving results, especially in terms of assembling the entire data acquisition and processing setup.

It is also expected to extend the implementation of the developed system, using the FBG-based fiber tip sensor, to other types of reactors/crystallizers, more compact and with different geometries.

In this way, the work developed on this PhD can serve as a starting position for further improvement and optimization of the developed sensors.

Finally, it is important to note that this work presents other topics of interest, namely:

- Fabrication of new FBG-based optical fiber tip sensors to optimize the monitorization of crystallization process in all channels of the planar-OFC and not only at the input and output channels.
- Study and developed new configurations of optical fiber sensors, sensitive to other parameters of interest in crystallization field, namely, crystal size, pressure and viscosity.
- Developed an array of sensors to perform continuous monitoring in OFCs geometries.
- Optimize data acquisition and processing setup.

Appendix A.

Raman spectroscopy: a process analytical technology for quantitative analysis of paracetamol

A.1. Introduction

Raman spectroscopy is a non-destructive and non-invasive technique that allows the performance of quantitative and qualitative analysis. These characteristics make Raman spectroscopy a technique with applicability in several scientific fields.

In this work, a Raman spectroscopy-based calibration model was developed to quantify paracetamol concentration in liquid solutions.

The concentration of paracetamol (a well-known API) in standard liquid solutions was quantified through the most sensitivity Raman paracetamol band at 1617 cm^{-1} . A linear relationship between the intensity of this band and the concentration was ascertained.

A.2. Fundamentals of Raman spectroscopy

The Raman effect was observed for the first time in 1928 by Chandrasekhara Venkata Raman, when he illuminated a liquid benzene with a mercury lamp and found that the light inelastically collided through the medium, giving rise to an optical phenomenon similar X-Ray scattering. This phenomenon was known as Raman scattering and guaranteed the Nobel Prize of Physics to C.V. Raman in 1930 [1, 2].

- **Principle of Raman effect**

When a monochromatic light focuses on a sample, part of the light is absorbed and transmitted, and other parts are scattered by the sample. According to the scattered light frequency, the scattering can be classified as: (1) elastic and (2) inelastic; the first one is the most likely to occur [1, 3].

Elastic scattering, also known as Rayleigh scattering, occurs when the photons suffer a change of direction during the collision with the sample molecules, however, its energy does not change, i.e., the frequency of scattered light is equal to the frequency of incident light. On the other hand, when a change occurs in the photon's energy, as consequence of the light collision with sample molecules, an inelastic scattering or Raman scattering happens. In this case, there is a difference between the frequencies of incidents and scattered lights, and an energy shift occurs between photon-molecules and molecules-photon. In this way, the energy of scattered light can be lower or higher than the energy of incident light, occurring Stokes or Anti-Stokes scattering, respectively. The difference between the energy of scattered and incident light is equal to the vibrational transition of sample molecules [3-5]. In **Figure A.1** diagrams of the different types of scattered and respective energy transitions are found.

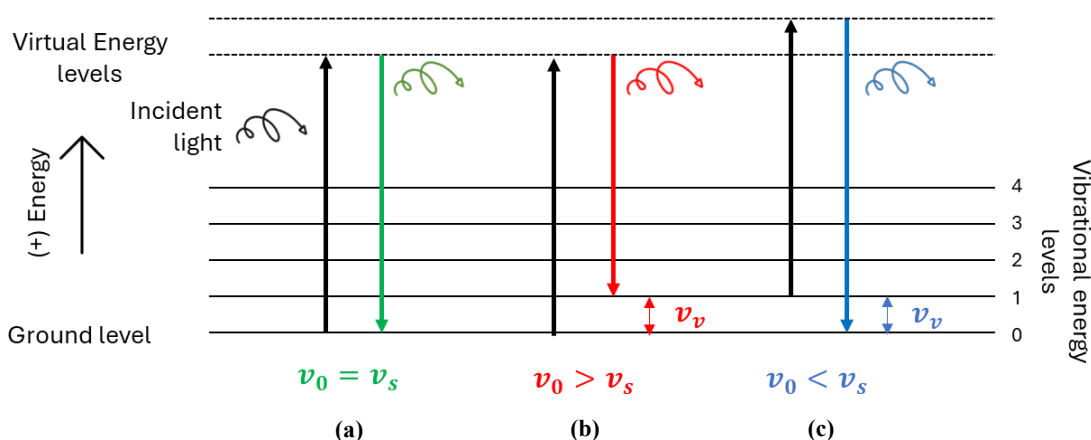


Figure A.1. Diagram representation of Rayleigh and Raman scattering processes. **(a)** Rayleigh scattering light; **(b)** Stokes Raman scattering light; **(c)** Anti-Stokes Raman scattering light. ν_0 , ν_s and ν_v correspond to the frequencies of incident light, scattered light, and vibrational transition, respectively, which are proportional to their energies. Adapted from [6].

When a monochromatic light (laser) focuses on a sample, its molecules, which are in the ground state (Energy = 0), are excited and reach a virtual state of excitement. As the molecules are instable, they quickly return to ground state. In this transition, if the molecules frequency does not change, and the transference between photon-mater or mater-photon does not happen, the scattered light has equal energy than the incident light, that is, the Rayleigh scattering takes place – **Figure A.1 (a)**. However, if in this transition the molecules return to an energy state higher than the ground state, Energy = 1, an energy transference from the photon to the matter occurs. Consequently, the

scattered light has lower energy than the incident light. In this case, the Stokes scattering happens, and the photon suffers a deviation to the red – **Figure A.1 (b)**. When the sample molecules are already in an excited state (Energy = 1) and the laser focus causes a transition to a lower energy state (Energy = 0), an energy transference from the mater to the photon occurs. For this reason, the scattered light has higher energy than the incident light. An Anti-Stokes scattering happens, and the photon has a deviation to the blue – **Figure A.1 (c)**.

Normally, the Stokes scattering is most likely to occur, because it does not depend on excited states, i.e., it is more common to find the molecules of samples in their fundamental state [3-6].

In the Raman spectrum it is possible to observe the Stokes and Anti-Stokes regions, as well as the Rayleigh line. In **Figure A.2** it is also possible to see that Anti-Stokes lines are less intense, compared with the Stokes lines, because, as previously referred, Anti-Stokes scattering requires the presence of molecules in excited energy levels [3, 5].

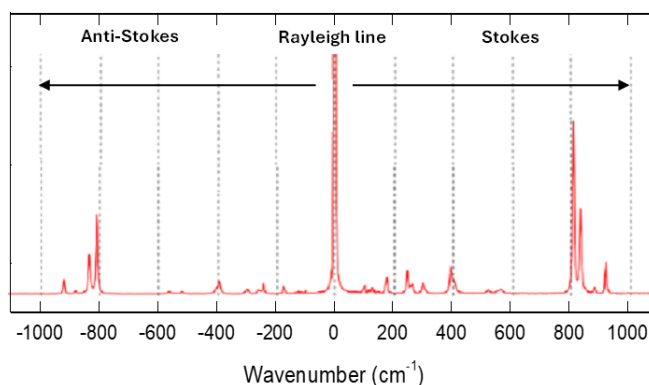


Figure A.2. Characteristics regions of a Raman spectrum: Rayleigh line and Stokes and Anti-Stokes regions. Adapted from [5].

- **Raman spectroscopy**

The Raman spectroscopy began to be implemented in the late 60's, because of technologic advances in the field of source and detection of light [4].

This is a vibrational optic technique that uses a laser as source, and it works based on the principle of dispersion (scattering) of inelastic light. The molecules of samples under study absorb the incident photons and transmit Raman photons, causing a transition between energy levels [4, 6].

The energy differences between these levels are associated to the molecular vibrational modes and they allow the extrapolation of information related to the chemical and structural composition of

sample, i.e., information about how the atoms is connected and which is the molecular geometry of sample under study. The substances present in the sample can also be identified through the characteristic spectral pattern that acts as a kind of fingerprint. Only this way is it possible to identify different compounds that have the same chemical formulation, but different structures. These spectral patterns can be used to quantify the presence of a given substance in the sample. In relation to the sample, it can be analyzed in different physical states, and it can correspond to any type of material, either organic or inorganic [3-5].

- **Instrumentation**

The typical Raman spectrometer is presented in **Figure A.3**. This is principally composed of five modules: (1) laser light source, (2) filter, (3) sample, (4) monochromator/Charge-Coupled Device (CCD), and (5) detector [4, 5].

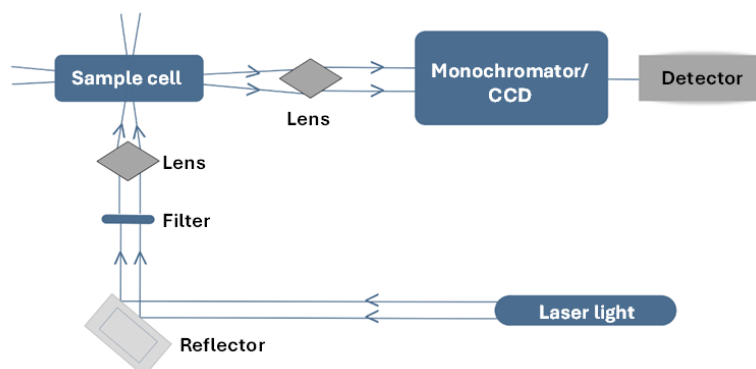


Figure A.3. Schematic representation of a typical Raman spectrometer. Adapted from [3].

As the Raman effect only occurs with a small fraction of incident photons, it is necessary an intense monochromatic light source: the laser. The most used laser sources are He-Ne (Helium-Neon, 632.8 nm) and Ar (Argon, 514.5 nm and 488.0 nm) lasers for visible light and solid-state neodymium YAG (Yttrium Aluminum Garnet) lasers for the near-infrared region. The filter is used to split the fraction of light that inelastically collides with the sample (photons with different wavelengths). These photons are analyzed by the spectrometer which cause the light dispersion through diffraction gratings and the different wavelengths are simultaneously detected in a CCD cam or sequentially detected in a monochromator. When the laser focuses on the sample, a characteristic Raman spectrum is created [3, 4].

- **Raman spectra**

The Raman spectrum represents the intensity of scattered light in relation to the wavenumber. The wavenumber is linearly correlated to the incident and scattered lights, which makes the Raman shift of materials normally independent of the incident light. The Raman shift is determined by the **Equation A.1**, where $\lambda_{incident}$ and $\lambda_{scattered}$ are the wavelengths (nm) of incident light and scattered light, respectively [6].

$$Raman\ shift = \left(\frac{1}{\lambda_{incident}} - \frac{1}{\lambda_{scattered}} \right) \times 10^7 \text{ (cm}^{-1}\text{)} \quad (\text{A.1})$$

Through the Raman spectrum it is possible to obtain several information about the material/sample in analysis, as shown in **Figure A.4**.

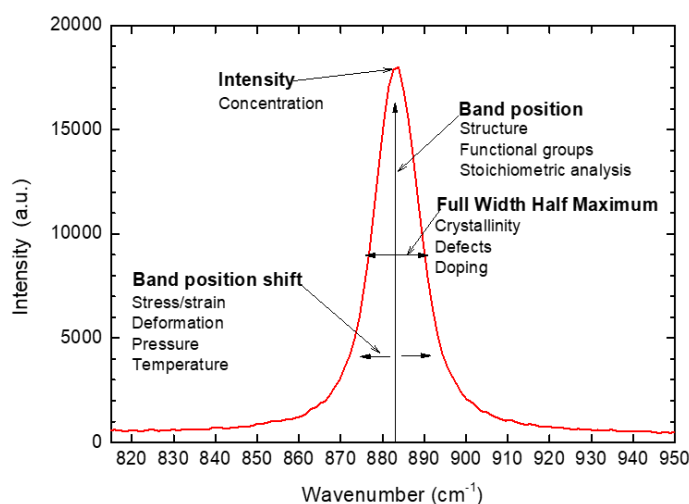


Figure A.4. Example of a Raman spectrum and respective information. Adapted from [6].

- **Main applications**

With the development of spectroscopy, the Raman technique has been implemented in several areas. This is a non-invasive and non-destructive technique that can provide information about chemical and structural composition of samples at a microscopic scale with imaging. Quantitative and qualitative analysis of whether solid, liquid, gas, gel, slurry, or powder materials can be

performed by Raman spectroscopy in an easy and rapid way [3, 4]. For this reason, **Table A.1** presents a list of different applications for said analytical tools.

Table A.1. Raman spectroscopy applications in different scientific fields.

Area of application	Examples of application	References
Life science	• Development of cell therapies: validate the quality of therapeutic cells	[7]
	• Evaluation of bone composition alterations: identification of disease or injury	[8]
	• Analysis of biocompatibility of a material: evaluation of tissue-implant interaction	[9]
Geology and Mineralogy	• Analysis of fluid inclusions: estimation of solute composition	[10]
	• Identification and classification of minerals	[11]
Pharmaceutical research and industry	• Identification of contaminants	[12]
	• Quality control of pharmaceutical products	[13]
	• Detecting polymorphisms of APIs	[14]
	• Determination of API concentration	[15, 16]
Semiconductors and carbon materials	• Identification of defects and dopants	[17]
	• Study of electrical properties	[18]

A.3. Quantitative analysis of paracetamol

Paracetamol is an API well known and utilized world-wide. For this reason, it is produced on a large scale by the pharmaceutical industry, through the crystallization process.

In this work, Raman spectroscopy technique was applied to quantify paracetamol concentration. Through this PAT tool, samples of the process flow, present in reactors/crystallizers during the crystallization process, can be analyzed and the concentration of paracetamol present in these samples can be determined. The chemical structure of paracetamol (4-Acetamidophenol) is shown in **Figure A.5** [19].

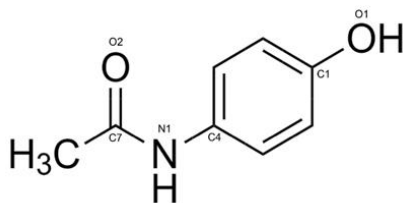


Figure A.5. Chemical structure of paracetamol. Adapted from [19].

- **Material and methods**

- (a) Samples preparation**

Nine paracetamol liquid samples were prepared in the laboratory at a room temperature of 25°C. Seeds of paracetamol (CAS¹ registry number 103-90-02, 98% of purity, from Sigma-Aldrich) were added to a solution of ethanol and deionized water, with a volume percentage of 40%/60%, respectively. Adding ethanol was necessary to guarantee the total dissolution of paracetamol seeds since the paracetamol solubility is higher in ethanol than only in water [20]. In this process, with a duration approximately of two hours, it was used a heating (at 75°C) and stirring (at 400 rpm) plate.

¹CAS – Chemical Abstracts Service

The prepared samples had a concentration range of 52.60 to 233.86 g of paracetamol per kg of solvent.

- (b) Acquisition system**

The Raman acquisition was performed through a Renishaw InVia™ Qontor confocal Raman spectrometer®. This equipment (**Figure A.6**) presents high efficiency and a spectral resolution better than 2 cm⁻¹ for the different excitation wavelengths, namely, 785, 633 and 532 nm. It also works with rejection filters, edge type, in the spectral range of 100–4000 cm⁻¹.

For correct utilization of the Raman acquisition system, it is necessary to procedure to a previous calibration using a standard sample of silicon (Si).



Figure A.6. Experimental setup: Raman spectrometer. System inVia Qontor, Renishaw®.

(c) Calibration

The standard silicon sample is placed in the microscope platin, and its surface is focused with a 50× objective. The 633 nm laser is used with a power of 50% for 1 second. The silicon Raman band should appear near to 521 cm^{-1} , as is shown in **Figure A.7**. If the band values do not agree with the expected, the spectrometer needs to be calibrated, according to the equipment manual.

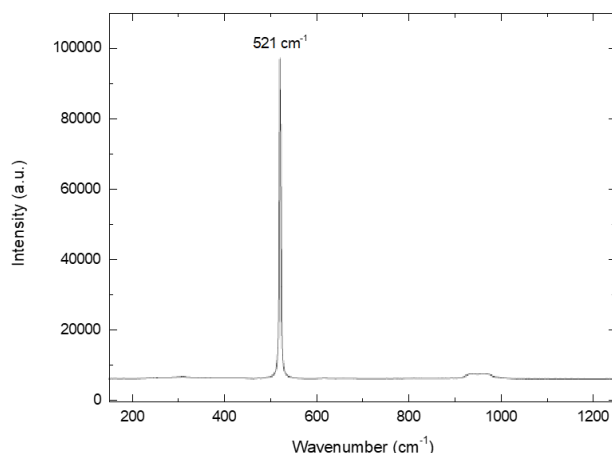


Figure A.7. Raman spectrum of silicon: calibration with a standard sample.

(d) Samples measurements

The paracetamol samples were put into a specific amorphous quartz cuvette to avoid influences on the Raman signal, and they were analyzed from its lowest to its highest concentration. Samples of pure ethanol and water were also analyzed as reference since these compounds are used as solvents. The Raman parameters adopted in the measurements are presented in **Table A.2**.

Table A.2. Raman acquisition parameters adopted.

Raman acquisition	
Lens	50×
Laser	633 nm
Optical power	5.5 mW
Exposure time	10 sec

It is important to notice that all measurements were performed at room temperature ($\sim 20^{\circ}\text{C}$) and to avoid intensity variations of collected light, the distance from the diffuser center to the lens was maintained constant between measurements.

(e) Data processing

For each Raman spectrum, the position and area of paracetamol bands were determined through the best adjustment of a sum of damped harmonic oscillators which is directly proportional to their excitation probability. These calculations were performed using the software IGOR Pro [21].

• **Results and discussion**

After data processing, it was possible to observe well defined Raman bands in the spectral range from 300 to 3200 cm^{-1} . However, only the bands present within the range from 300 to 1800 cm^{-1} were considered relevant, as shown in **Figure A.8**. According to the literature, it is possible to find Raman bands associated with the vibrational modes of paracetamol in this spectral range, regardless of other chemical compounds that may be present in solution [22].

The bands marked with * in **Figure A.8** are solely associated with ethanol and they were identified through the comparison with the pure ethanol spectrum. The corresponding vibrational modes are listed in **Table A.3**.

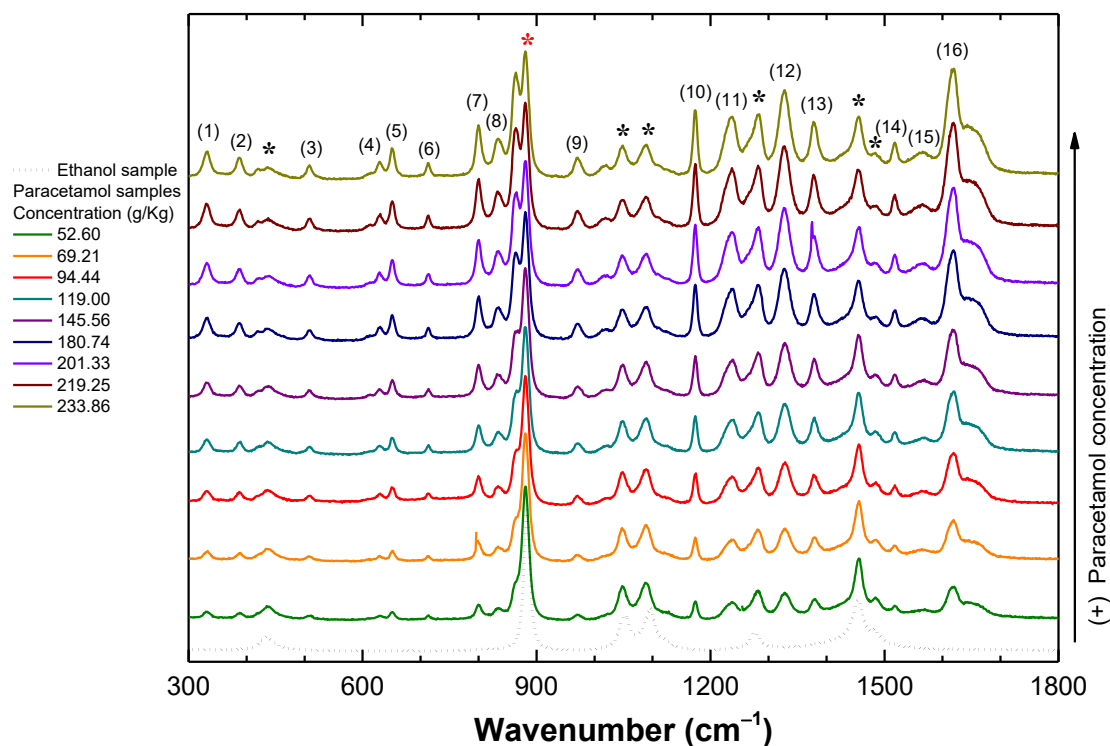


Figure A.8. Raman spectra of ethanol and paracetamol samples in a spectral range of 300 to 1800 cm^{-1} . The Raman bands associated with ethanol are identified with * and the paracetamol bands are numbered by order, according to Table A.4.

Table A.3. Ethanol-assigned Raman bands and respective vibrational modes [25].

Raman band (cm^{-1})	Vibrational mode
436	δCCO
881	$\nu_s\text{CCO}$
1048	C–O (link), νCO
1087	CCO , νCH_3
1281	δCH_2
1455	$\delta_{\text{as}}\text{CH}_3$
1484	δCH_2 e δCH_3

(δ – corresponds to the out-of-plane deformation modes); (ν_s – corresponds to the symmetric stretching modes); (ν – corresponds to the stretching modes); (δ_{as} – corresponds to the asymmetric deformation modes).

Furthermore, the samples also have in their composition deionized water. However, in the spectral range in analysis (300–1800 cm^{-1}), there are not representative water bands, according to the literature [23]. There is only a single water band at $\sim 1600 \text{ cm}^{-1}$. This is a very weak band when it is combined with concentrations of ethanol higher than 35% [25]. For this reason, the presence of this compound was ignored.

The paracetamol bands are numbered (1 to 16) in **Figure A.8** and their respective vibrational modes are listed in **Table A.4**.

Table A.4. Paracetamol-assigned Raman bands and respective vibrational modes [22].

Raman band (cm ⁻¹)	Vibrational mode
(1) 332	$\beta\text{N—C—CH}_3$
(2) 388	$\beta\text{C—R}_1 + \beta\text{C—R}_2$
(3) 508	$\beta\text{C=O}$
(4) 629	$\nu\text{N—C} + \nu$
(5) 651	αCCC
(6) 713	δCCC
(7) 800	γCH
(8) 833	γCH
(9) 971	γCH
(10) 1174	βCH
(11) 1236	$\nu\text{C—R}_1$
(12) 1328	νCC
(13) 1379	$\delta_s\text{CH}_3$
(14) 1518	νCC
(15) 1565	$\beta\text{NH (amide group)}$
(16) 1617	νCC

(β – corresponds to the in-plane deformation modes of the substituents); (ν – corresponds to the stretching modes); (α – corresponds to the in-plane deformation modes of the aromatic ring – phenyl ring); (δ – corresponds to the out-plane deformation modes of the aromatic ring – phenyl ring); (γ – corresponds to the out-plane deformation modes of the substituents); (δ_s – corresponds to the symmetric deformation modes of CH_3); (R_1 – corresponds to the paracetamol amide group); (R_2 – corresponds to the paracetamol hydroxyl group).

To better understand the behavior of the Raman bands with increasing concentration of paracetamol, a quantitative analysis based on the study of the relative integrated intensities was performed. For that purpose, the relative area under the curve of each Raman band was calculated based on the adjustments performed by the software IGOR Pro.

In **Figure A.9** a representative example of the adjustments performed for the band at 1517 cm^{-1} , and for different paracetamol concentrations, is shown.

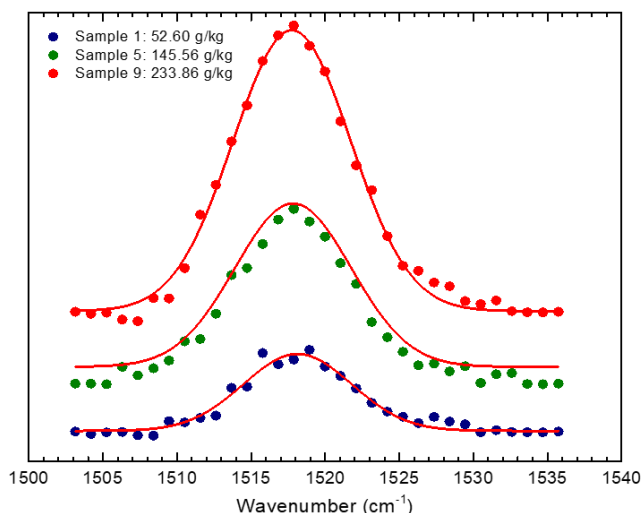
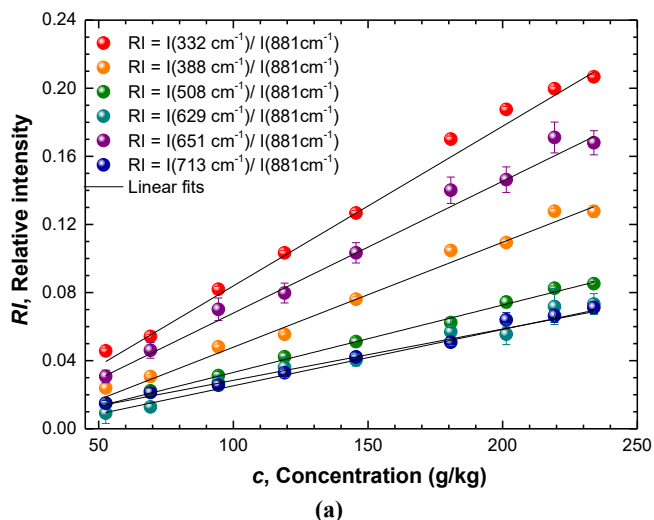


Figure A.9. Example of the adjustment performed in the calculations of paracetamol bands intensity. Representation for paracetamol band at 1518 cm^{-1} , present in the Raman spectra of the samples with the lowest (52.60 g/kg), intermediate (145.56 g/kg) and highest (233.86 g/kg) concentration.

As previously mentioned, considering the spectral range in analysis, and in addition to the bands associated with paracetamol, there is also the presence of ethanol bands. For this reason, a normalization regarding the most intense ethanol band (at 881 cm^{-1} , identified in **Figure A.8**) was performed, i.e., the ratio between each paracetamol band and the ethanol band at 881 cm^{-1} was calculated and plotted as a function of the concentration in solution.

The results reveal a linear dependence of relative intensity in relation to concentration all-paracetamol bands as is shown in **Figure A.10**.



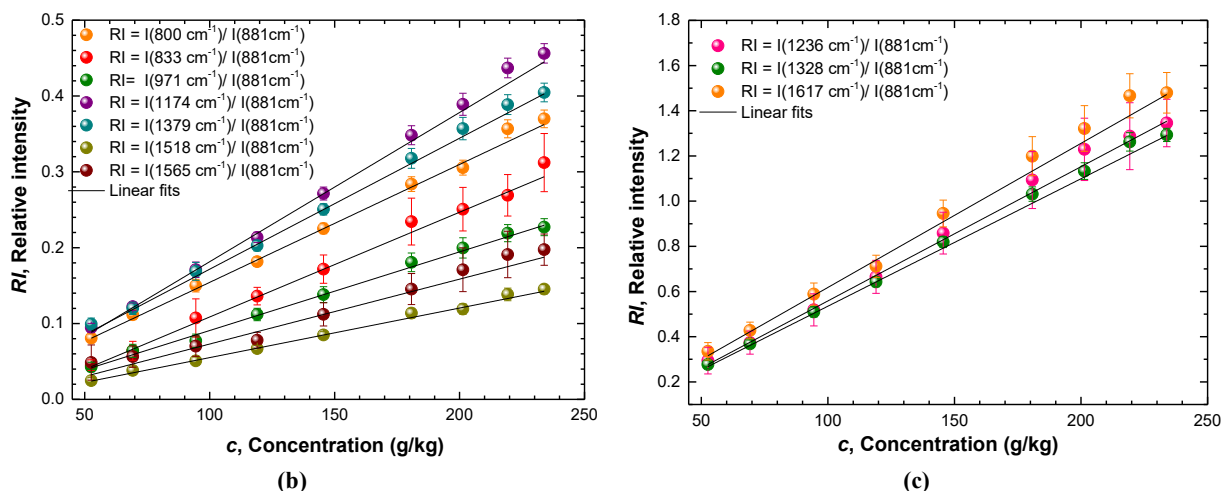


Figure A.10. Relative intensity (i.e., ratio between the intensity of paracetamol bands and the intensity of ethanol band at 881 cm^{-1}) as a function of paracetamol concentration. (a) Paracetamol bands 332, 388, 508, 629, 651 and 713 cm^{-1} ; (b) Paracetamol bands 800, 833, 971, 1174, 1379, 1518 and 1565 cm^{-1} ; (c) Paracetamol bands 1236, 1328 and 1617 cm^{-1} .

The sensitivity of all-paracetamol bands was determined through the slope of the corresponding linear relation and the values are presented in **Table A.5**.

Table A.5. Intensity band sensitivity to the variation of paracetamol concentration.

Band position (cm^{-1})	Sensitivity ($\times 10^{-3}$)	R^2
332	(0.94 ± 0.05)	0.994
388	(0.62 ± 0.04)	0.990
508	(0.40 ± 0.01)	0.994
629	(0.27 ± 0.03)	0.994
651	(0.77 ± 0.03)	0.997
713	(0.30 ± 0.01)	0.992
800	(1.55 ± 0.05)	0.983
833	(1.38 ± 0.08)	0.976
971	(1.04 ± 0.03)	0.978
1174	(1.97 ± 0.08)	0.993
1236	(5.94 ± 0.21)	0.990
1328	(5.64 ± 0.23)	0.994
1379	(1.73 ± 0.10)	0.985
1518	(0.65 ± 0.02)	0.963
1565	(0.86 ± 0.08)	0.996
1617¹	(6.38 ± 0.32)	0.998

¹ The most sensitive band.

The results (**Figure A.8** and **Table A.5**) demonstrate that the paracetamol band at 1617 cm^{-1} is the most sensitive to the variation of paracetamol concentration. Therefore, the 1617 cm^{-1} band can

be adjusted to obtain a linear relation between the band values (relative integrated intensity) and concentration. This calibration (**Figure A.8**) may be used as a principle to future measurements, according to **Equation A.2**.

$$c = (1.57 \times 10^2)RI + 3.12 \text{ (g/kg)} \quad (\text{A.2})$$

A.4. Final remarks

In this work, paracetamol samples with different concentrations were analyzed by Raman Spectroscopy. With this analysis, it was intended to develop a method capable of quantifying the paracetamol concentration present in the studied solutions. After the identification of Raman bands associated to the paracetamol, it was verified the existence of a linear relation between the relative intensity of Raman band at 1617 cm^{-1} and the paracetamol concentration present in the solution. This linear relation may be used in the quantification of paracetamol concentration in solution.

In conclusion, the results obtained allow to prove the potential of Raman spectroscopy as an analytical tool, however, the need of sampling is a disadvantage.

The need for sampling could create some problems, namely, (1) difficulty in accessing the sample; (2) presence of an unrepresentative sample and (3) need of a recurrent sampling process that changes the process flow.

Considering these limitations, in crystallization, technology which allows real-time measurements is the most advantageous, since it makes sample preparation unnecessary, and the process flow is not disturbed.

References

- [1] C. V. Raman, and K. S. Krishnan, “A New Type of Secondary Radiation”, *Nature*, vol.121, n°3048, pp.501-502, Marc.1928, DOI:10.1038/121501c0.
- [2] T. N. Foundation, “Sir Chandrasekhara Venkata Raman - Biographical”, The Nobel Foundation. <https://www.nobelprize.org/prizes/physics/1930/raman/biographical/> (accessed sept. 25, 2024).
- [3] W. Wang, H. Zhang, Y. Yuan, and Y. H. S. Guo, “Research Progress of Raman Spectroscopy in Drug Analysis”, *AAPS PharmSciTech*, vol.19, n°7, pp.2921-2928, Oct. 2018, DOI:10.1208/s12249-018-1135-8.
- [4] J. Jesus, R. Löbenberg, and N. A. Bou-Chacra, “Raman Spectroscopy for Quantitative Analysis in the Pharmaceutical”, *J Pharm. Pharm. Sci.*, vol.23, n°1, pp.24-46, Mar. 2020, DOI: 10.18433/jpps30649.
- [5] G. Bumbrah, and R. Sharma, “Raman spectroscopy – Basic principle, instrumentation and selected applications for the characterization of drugs of abuse”, *Egypt J. Forensic Sci.*, vol.6, n°3, pp.209-215, Sept. 2016, DOI:10.1016/j.ejfs.2015.06.001.
- [6] Z. Xu, Z. He, Y. Song, X. Fu, M. Rommel, X. Luo, A. Hartmaier, J. Zhang, and F. Fang, “Topic Review: Application of Raman Spectroscopy Characterization in Micro/Nano-machining”, *Micromachines*, vol.9, n°7, 361, July 2018, DOI: 10.3390/mi9070361.
- [7] S. Rangan, H. Schulze, M. Vardaki, M. Blades, J. Piret, and R. Turner, “Applications of Raman spectroscopy in the development of cell therapies: state of the art and future perspectives”, *Analyst*, vol.145, n°6, pp.2070-2105, Feb. 2020, DOI: 10.1039/C9AN01811E.
- [8] M. Morris, and G. Mandair, “Raman assessment of bone quality”, *Clin Orthop Relat Res.*, vol.469, n°8, pp.2160-2169, Aug. 2011, DOI:10.1007/s11999-010-1692-y.
- [9] G. Kalisz, A. Przekora, P. Kazimierzczak, B. Gieroba, M. Jedrek, W. Grudzinski, W. Gruszecki, G. Ginalska, and A. Sroka-Bartnicka, “Application of Raman Spectroscopic Imaging to Assess the Structural Changes at Cell-Scaffold Interface”, *Int. J. Mol. Sci.*, vol.22, n°2, 485, Jan. 2021, DOI:10.3390/ijms22020485.
- [10] H. Chu, G. Chi, and C. Xue, “Quantification of Solute Composition in H₂O-NaCl-CaCl₂ Solutions Using Cryogenic 2D Raman Mapping”, *Minerals*, vol.10, n°11, 1043, Nov. 2020, DOI:10.3390/min10111043.

-
- [11] Z. Guo, L. Yu, S. Tian, X. Lv, and W. Xue, “Raman Spectroscopy Analysis of Minerals Based on Feature Visualization”, *Spectroscopy*, vol.35, n°11, pp.37–46, Nov. 2020.
- [12] M. K. Maruthamuthu, A. H. Raffiee, D. M. De Oliveira, A. M. Ardekani, and M. S. Verma, “Raman spectra-based deep learning: A tool to identify microbial contamination”, *MicrobiologyOpen*, vol.9, n°11, e1122, Sept. 2020, DOI:10.1002/mbo3.1122.
- [13] J. Omar, A. Boix, and F. Ulberth, “Raman spectroscopy for quality control and detection of substandard painkillers”, *Vibrational Spectroscopy*, vol.111, 103147, Nov. 2020, DOI:10.1016/j.vibspec.2020.103147.
- [14] Y. N. Thi, K. Rademann, and F. Emmerling, “Direct evidence of polymorphism in paracetamol”, *CrystEngComm.*, vol.17, n°47, pp.8967–9244, Oct. 2015, DOI:10.1039/C5CE01583A.
- [15] G. Lakhwani, O. Sherikar, and P. Mehta, “Nondestructive and rapid concurrent estimation of paracetamol and nimesulide in their combined dosage form using Raman spectroscopic technique”, *Indian J Pharm Sci.*, vol.75, n°2, pp.211–216, Mar.- Apr. 2013, PMCID: PMC3757861.
- [16] S. Duraipandian, M. Knoppb, M. Pollarda, H. Kerdoncuffa, J. Petersena, and A. Müllertz, “A fast and novel internal calibration method for quantitative Raman measurements on aqueous solutions”, *Anal. Methods*, vol.10, n°29, pp.3589-3593, June 2018, DOI:10.1039/C8AY00753E.
- [17] R. Beams, L. Cançado, and L. Novotny, “Raman characterization of defects and dopants in graphene”, *J. Phys.: Condens. Matter*, vol.27, n°8, 083002, Jan. 2015, DOI:10.1088/0953-8984/27/8/083002.
- [18] R. Tanta, M. Madsen, Z. Liao, P. Krogstrup, T. Vosch, J. Nygård, and T. Jespersen, “Raman spectroscopy and electrical properties of InAs nanowires with local oxidation enabled by substrate micro-trenches and laser irradiation”, *Appl. Phys. Lett.*, vol.107, n°24, 243101, Dec. 2015, DOI:10.1063/1.4937442.
- [19] M. Amare, “Voltammetric determination of paracetamol in tablet formulation using Fe (III) doped zeolite-graphite composite modified GCE”, *Heliyon*, vol.5, n°5, e01663, May 2019, DOI:10.1016/j.heliyon.2019.e01663.
- [20] R. Granberg, and Å. Rasmuson, “Solubility of paracetamol in pure solvents”, *J. Chem. Eng. Data.*, vol.44, n°6, pp.1391-1395, Nov. 1999, DOI:10.1021/je990124v.

-
- [21] WaveMetrics, “Igor Pro”. <https://www.wavemetrics.com/products/igorpro> (accessed sept. 25, 2024).
- [22] A. Amado, C. Azevedo, and P. Ribeiro-Claro, “Conformational and vibrational reassessment of solid paracetamol”, *Spectrochim Acta A Mol Biomol Spectrosc.*, vol.183, pp.431-438, Aug. 2017, DOI:10.1016/j.saa.2017.04.076.
- [23] S. M. Baschenko, and L. S. Marchenko, “On Raman spectra of water, its structure and dependence on temperature”, *Semicond. Phys. Quantum Electron.*, vol.14, n°1, pp.77-79, Feb. 2011, DOI:10.15407/spqeo14.01.077.
- [24] S. Burikov, T. Dolenko, S. Patsaeva, Y. Starokurov, and V. Yuzhakov, “Raman and IR spectroscopy research on hydrogen bonding in water–ethanol”, *Molecular Physics*, vol.108, n°18, pp.2427–2436, Sept. 2010, DOI:10.1080/00268976.2010.516277.
- [25] A. Emin, A. Hushur, and T. Mamtimin, “Raman study of mixed solutions of methanol and ethanol”, *AIP Advances*, vol.10, n°6, 065330, June 2020, DOI:10.1063/1.5140722.

Appendix B.

Fiber Bragg grating-based optical fiber tip sensor for refractive index sensing

B.1. Introduction

In this work, the potential of an optical fiber tip sensor to perform refractive index (RI) measurements was tested.

The developed sensor is presented in **Chapter 6** of this document, **section 6.3.1**, and it corresponds to an 8 mm-length FBG section that was cleaved in the middle, forming a fiber tip with a 4 mm-length FBG inscribed at its end.

Meng et al. proves the potential of a similar configuration to performed RI measurements of liquid solutions [1]. According to the authors, when the FBG-based fiber tip sensor was immersed in liquid solutions with different RI, the side mode of the FBG optical spectrum varies due to the Fresnel reflection at the cleaved fiber tip-end [2]. If the samples were measured at the same temperature, the peak associated with the FBG remains constant.

B.2. Experimental setup

Samples with different RI were measured using the same experimental setup shown in **Figure 6.11** of **section 6.3.1 – Chapter 6**. The sensors were interrogated in reflection using the portable interrogation system Bragg METER FS2 and their responses were recorded by the software BraggMONITOR SI. Optical fiber tip sensors (1) and (3), identified in **Table 6.5** of **Chapter 6**, were used in this experiment.

Optical fiber tip sensor (1) was used to perform measurements of a calibrated RI kit, from the company Cargille Laboratories. The RI liquid set includes 10 different liquids whose RI values are certified and, in this case, range from 1.30 to 1.39.

The sensing head was vertically immersed in each sample, from the lowest (1.30 RIU) to the highest (1.39 RIU) RI value, and its optical response was recorded. After each measurement, the sensing head was cleaned with ethanol to avoid possible contamination.

The same procedure, however, for optical fiber tip sensor (3), was performed using paracetamol samples with different concentration/RI values (concentration ranged from 102.20 to 183.93 g/kg (g of paracetamol per kg of solvent), corresponding to a RI range of 1.3677 RIU to 1.3733 RIU). The samples were prepared and characterized as mentioned in **Chapter 6, section 6.4.1**.

B.3. Results and discussion

The FBGs used to fabricate the sensors had a Bragg resonance wavelength, λ_B , of ~ 1554 nm. After the cleavage, the output spectrum of the sensor maintained a maximum power level near to this value, as it is possible to see in **Figure B.1**.

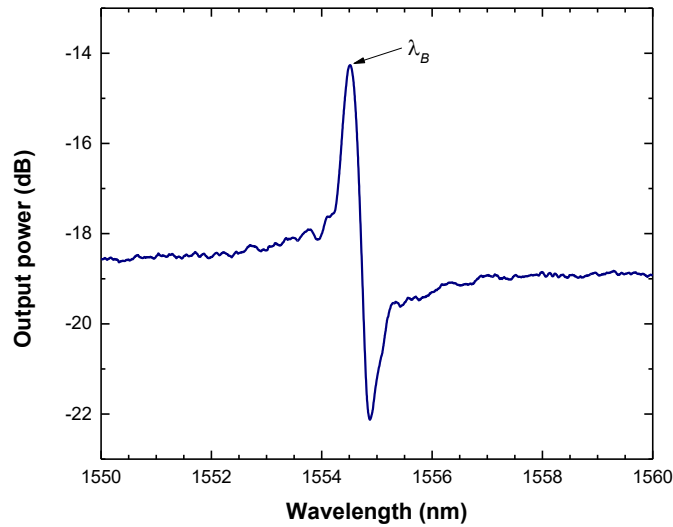


Figure B.1. Spectral characterization of the optical fiber tip sensor fabricated.

The spectrum shown in **Figure B.1** is related to optical fiber tip sensor (1), however, the spectrum of optical fiber tip sensor (3) is similar. The spectrum shows the signal that is reflected by the optical fiber tip, when the sensor is only in contact with air. The FBG cleavage creates an overlap of FBG reflection spectra and its own transmission spectra [3].

Figure B.2 shows the optical fiber tip sensor (1) output spectrum, when the sensing head is in contact with each liquid sample, with different RI (calibrated RI kit).

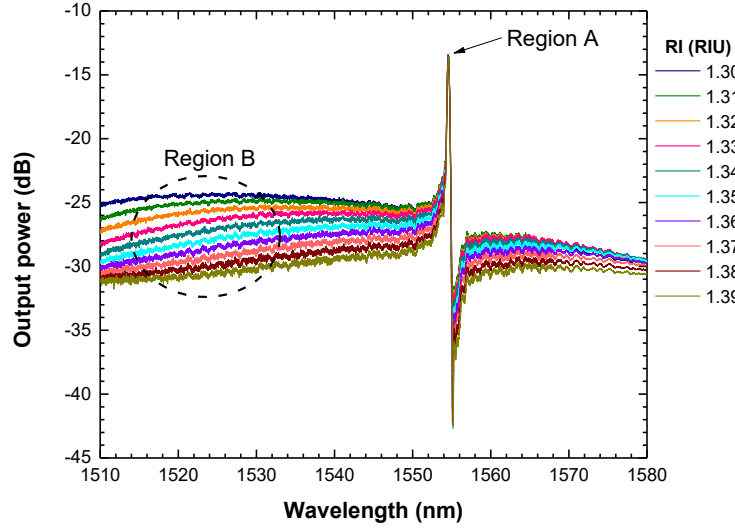


Figure B.2. Output spectrum for each RI measured (optical fiber tip sensor 1).

Since the samples (calibrated RI kit) were stored at room temperature ($\sim 20^\circ\text{C}$) and the measurements were performed under the same conditions, the peak associated with the Bragg resonance wavelength (Region A) remains constant, ~ 1554 nm (**Figure B.2**). However, the left side of the sensor optical spectra, at ~ 1520 nm (Region B), varies with the samples RI. This variation is illustrated **Figure B.3**.

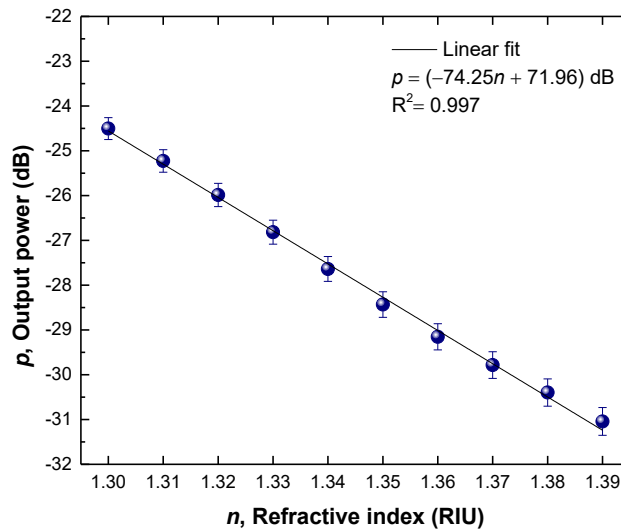


Figure B.3. Optical output power as a function of RI.

The output power response of the sensor linearly varies with the increase of RI (correlation factor of 0.997), as shown in **Figure B.3**. A linear sensitivity of (-74.25 ± 1.29) dB/RIU was obtained to the variation of RI, with ranges of 1.30 to 1.39 RIU.

In relation to paracetamol samples, **Figure B.4 (a)** shows the optical fiber tip sensor (3) output spectrum for each paracetamol sample measured. The optical power response of the sensor to the variation of RI, at a measuring wavelength at 1520 nm (left side of FBG baseline – Region B), is shown in **Figure B.4 (b)**.

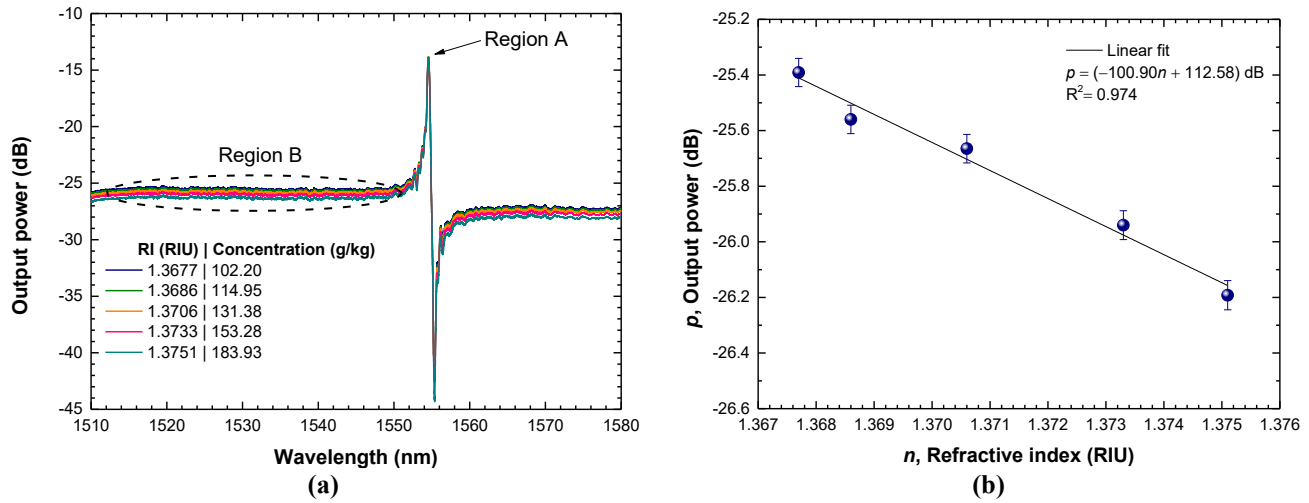


Figure B.4. Measurements of paracetamol samples using optical fiber tip sensor (3). **(a)** Output spectrum for each paracetamol sample measured; **(b)** Optical power sensor response to the variation of RI, at a measuring wavelength of 1520 nm.

As it is possible to see in **Figure B.4**, the sensor output power response, at a measuring wavelength of 1520 nm, linearly varies with the increase of RI (correlation factor of 0.974). A linear sensitivity of (-100.90 ± 8.15) dB/RIU was obtained, with ranges of 1.3677 to 1.3751 RIU. Since the samples were kept and measured at room temperature, $\sim 20^\circ\text{C}$, the peak associated with the FBG (Region A, **Figure B.4 a**) remains constant.

These experimental results were compared with the simulated ones, proposed by the numerical model developed by Robalinho et al. for this type of sensing structure [3].

Figure B.5 (a) corresponds to the simulation results from the numerical model to a RI variation from 1.366 to 1.376 RIU (working range). At the left side of FBG baseline, there is a spectral wavelength range (Region B) where the intensity decreases with the increase of RI samples

(Figure B.5 a). This region is equivalent to Region B identified at Figure B.4 (a), for experimental results (measuring wavelength of 1520 nm).

In the simulation spectrum (Figure B.5 a), it is also possible to see that at Region A, referent to the FBG peak, the intensity also decreases with the increase of RI, which did not happen in the experimental results. This could be related to the lack of resolution of the equipment used to acquire the sensor response.

It is important to note that, besides the left side of FBG baseline (Region B), it is also possible to measure the influence of RI in the sensor response at the right-side of FBG baseline. This is also proved by Meng et al. [1]. However, only the left side was considered since, in the experimental results, due to the lack of resolution, the right-side of FBG baseline had less sensitivity to RI variations (as it is clearly shown in Figure B.2).

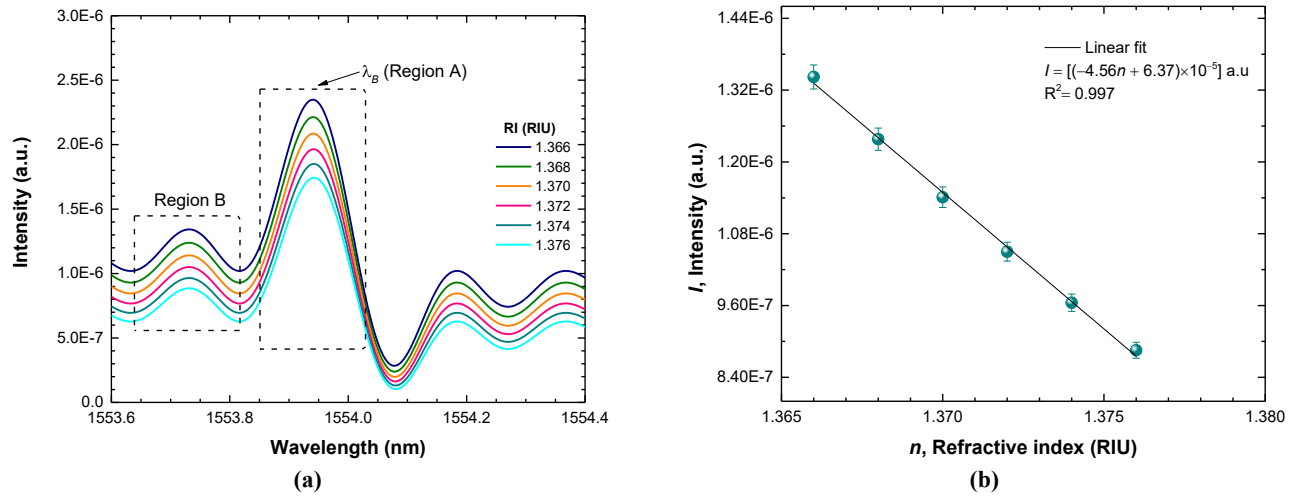


Figure B.5. Simulation results. (a) Output spectrum for each RI; (b) Output intensity as a function of RI.

In relation to the simulated results, a linear approximation of the obtained sensor output response (Figure B.5 a) at Region B as a function of RI was carried out – Figure B.5 (b). The data of this approximation is shown in Table B.1.

Table B.1. Parameters obtained by a linear approximation when varying the RI ($I = m \cdot n + b$).

	m	b
Value	(-4.56×10^{-5})	(6.37×10^{-5})
Standard Error	$\pm(1.11 \times 10^{-6})$	$\pm(1.52 \times 10^{-6})$
R^2	0.997	

To compare the experimental results (**Figure B.4 b**) and the simulated ones (**Figure B.5 b**), for a RI ranged from ~ 1.366 to 1.376 RIU, a data normalization was performed, according to **Equation B.1** [4].

$$X_{norm} = \frac{X - X_{min}}{X_{max} - X_{min}} \quad (\text{B.1})$$

The performed normalization is commonly used and allowed to transform the data into a specific interval, generally, between 0 and 1. Through this, it is possible to put the two groups of data (experimental and stimulated) on the same scale, allowing their comparison [4]. In this way, through **Equation B.1**, the original data, X , is transformed into a normalized value, X_{norm} , using the minimum data value, X_{min} , and the maximum data value, X_{max} .

The comparison between experimental and stimulated data was established and illustrated at **Figure B.6**.

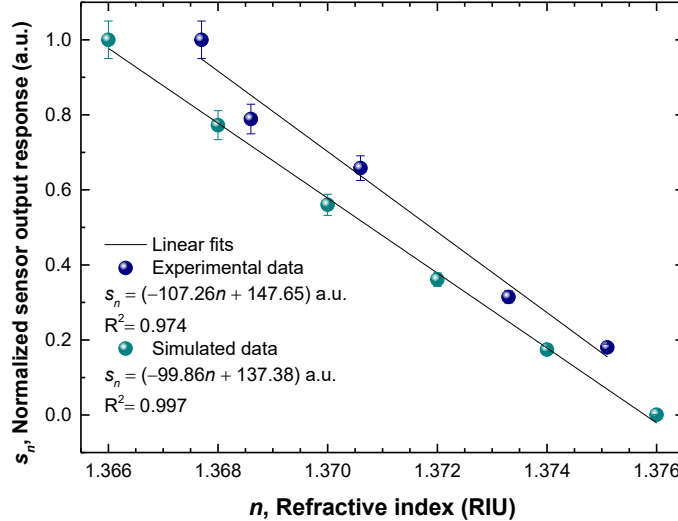


Figure B.6. Comparison between experimental and simulated data (normalized data). Variation of sensor output response as a function of RI.

Figure B.6 shows that the experimental data are in good agreement with the simulated one. It was observed linear approximations, with correlations factors higher than 0.97. As expected, for the simulated data, the correlation factor is higher, since the experimental results are influenced by

several factors, namely, equipment resolution, human error, measurement error and environmental factors. Besides this, close values of sensitivity were obtained, namely, (-99.86 ± 2.42) a.u./RIU and (-107.26 ± 8.67) a.u./RIU, for simulated and experimental data, respectively.

B.4. Final remarks

A simple geometry of sensing head based on a FBG was developed. This sensing head results in an FBG cleaved in the middle, forming an optical fiber tip.

Besides temperature measurements (**Chapter 6, section 6.3** of this document), it was also found that this sensor can be used in RI sensing.

Due to its reduced dimensions and simplicity, this sensor may find applications in chemical and biological sensing fields.

References

- [1] H. Meng, W. Shen, G. Zhang, C. Tan, and X. Huang, “Fiber Bragg grating-based fiber sensor for simultaneous measurement of refractive index and temperature”, *Sensors and Actuators B: Chemical*, vol.150, n°1, pp.226-229, Sept. 2010, DOI:10.1016/j.snb.2010.07.010.
- [2] E. Hecht, *Optics*, 5th ed., Pearson: London, UK, 2015.
- [3] P. Robalinho, V. Piaia, L. Soares, S. Novais, A. L. Ribeiro, S. Silva, and O. Frazão, “Phase-shifted fiber Bragg grating by selective pitch slicing”, *Sensors*, vol.24, n°21, 6898, Oct. 2024, DOI:10.3390/s24216898.
- [4] A. K. Jain, R. P. W. Duin, and J. Mao, “Statistical Pattern Recognition: A Review”, *IEEE Trans. Pattern Anal. Mach. Intell.*, vol.22, n°1, pp.4-37, Jan. 2000, DOI: 10.1109/34.824819.